

**Sensorless Out-of-Plane Displacement Estimation
for Freehand 3D Ultrasound Applications**

by

Mahla Abdolahnejad Bahramabadi

A thesis submitted to the Faculty of Graduate and Postdoctoral
Affairs in partial fulfillment of the requirements for the degree of

Master of Applied Science

in

Biomedical Engineering

Department of Systems and Computer Engineering
Carleton University
Ottawa, Ontario

© 2014, Mahla Abdolahnejad Bahramabadi

Abstract

The aim of freehand 3D ultrasound imaging is to construct a 3D volume of data from conventional 2D ultrasound images. In freehand 3D ultrasound, the probe is moved by hand over the area of interest in an arbitrary manner and its motion is measured by attaching some kind of position sensor to the probe. Since attaching external tracking sensor to the probe imposes some difficulties, alternative ways are investigated to acquire freehand 3D ultrasound without a position sensor. Sensorless Estimation of any in-plane motion between images is reliably determined using standard image registration techniques and the big challenge is out-of-plane motion estimation. The most important approach to overcome this challenge so far is to use the speckle decorrelation method. The method is based on the idea that the correlation value of a specific model of speckle known as Fully Developed Speckle (FDS) can be used to estimate the out-of-plane displacement between images. However, the method requires the B-scans to contain mostly regions of FDS pattern but this kind of pattern is rare in scans of real tissue. One successful way around this problem is to quantify the amount of coherency at each point in the B-scans by calculating the axial and lateral correlations and comparing them with the FDS calibrated ones. This approach leads to adapt elevational decorrelation curves based on the amount of non-FDS regions in the image. The novelty of this thesis is firstly adjusting the method to be applicable on B-mode ultrasound images rather than RF ultrasound data because RF data is not always available in clinical environments. Secondly, the experiment setup is truly freehand and the motion of the probe is not constrained in any directions during scanning and in-plane motion compensation is required. Thirdly, the method is tested on in vivo human data as well as test chicken and beef data sets. The method is shown to work quite remarkable (accuracy of around 5%) for the elevational distance estimation for both test phantoms and real human tissue data.

Acknowledgements

I would like to use this opportunity to thank my supervisor Dr. Chris Joslin, Associate Professor of School of Information Technology, Carleton University, for his friendly guidance, inspiration and assistance.

I would also like to thank Dr. Yuu Ono for his guidance and for providing the lab equipment to be used in the experiments of this thesis. Surely, it would not be possible to conduct this research without his support.

I am also grateful to my lab mates and coworkers for making the lab an inspiring environment to research.

I would also like to thank to my family and friends for their endless support and encouragement. I am sure that without their support it would not be possible for me to go towards the completion of Master's Degree.

Finally and most importantly, I wish to extend my sincere gratitude to my mom for keeping faith in me.

Table of Contents

Abstract	i
Acknowledgements	ii
List of Figures	vi
List of Tables	x
List of Acronyms	xi
Chapter 1 Introduction	1
1.1 Overview	1
1.2 Problem Statement.....	3
1.3 Proposed Method.....	4
1.4 Thesis Contributions.....	6
1.5 Thesis Organization.....	7
Chapter 2 Background Review	9
2.1 Ultrasound Physics	9
2.2 Ultrasound Instrumentation.....	13
2.3 Ultrasound Imaging Modalities (Modes)	15
2.4 Ultrasound and Musculoskeletal Imaging.....	17
Chapter 3 State of the Art Review	20
3.1 3D Ultrasound Imaging	20
3.1.1 Limitations of Conventional 2D Ultrasound.....	21
3.1.2 3D Ultrasound Acquisition Techniques	22

3.2	Freehand 3D Ultrasound System.....	24
3.2.1	Ultrasound Probe Tracking Systems.....	25
3.2.2	Calibration Process.....	26
3.2.3	3D Reconstruction Algorithms	29
3.2.4	Challenges of Using Freehand 3D Ultrasound.....	31
3.3	Sensorless Probe Motion Estimation.....	31
Chapter 4 Methodology		36
4.1	Statistics of Ultrasound Speckle.....	37
4.1.1	Statistical Modeling of Speckle	37
4.1.2	Correlation Formulation.....	39
4.1.3	Out-of-Plane Motion Estimation Using Speckle.....	41
4.2	Experimental Procedure and Data Acquisition	41
4.2.1	Overview of Proposed Framework	41
4.2.2	Experimental Setup and Data Acquisition	44
4.2.3	Ultrasound Machine and Probe Specification.....	48
4.2.4	Electromagnetic Sensor Specification.....	50
4.3	Primary Data Processing	52
4.3.1	Temporal Calibration	53
4.3.2	Spatial Calibration.....	58
Chapter 5 Data Processing and Results.....		66
5.1	Data Samples Selection	66
5.2	FDS Decorrelation Curves Calibration	68
5.2.1	In-Plane Motion Compensation	69
5.2.2	Creating Decorrelation Curves.....	70
5.3	FDS Decorrelation Curves Adjustment.....	79

5.4	Method Evaluation	82
5.5	Discussion.....	87
Chapter 6 Conclusions and Future Work.....		93
6.1	Conclusions	93
6.2	Future Works.....	95
References.....		96

List of Figures

Figure 2.1 Different Types of Interactions of Ultrasound Waves with Tissue.....	12
Figure 2.2 Typical Ultrasound B-scan Image of Thigh Muscle	13
Figure 2.3 Basic Component Elements of Imaging Ultrasound Transducer.	14
Figure 2.4 Principles of Phased Arrays	15
Figure 2.5 Generating an A-mode Echo Signal.....	16
Figure 2.6 Typical Ultrasound M-mode Image of Heart Valve	17
Figure 3.1 Definitions of Ultrasound Directions and Different Volume Shapes Produced by Mechanical Sweep Motions.....	23
Figure 3.2 Schematic View of Freehand 3D Ultrasound Scanning.....	25
Figure 3.3 Coordinate Systems of Freehand 3D Ultrasound System	27
Figure 3.4 Principles of Elevational Speckle Decorrelation.....	33
Figure 3.5 Two Pixels on Adjacent B-scans and Corresponding Ultrasound Resolution Cells.	34
Figure 4.1 Block Diagram of Experimental Procedure and Proposed Methodology	42
Figure 4.2 PATRIOT Electromagnetic Sensor Mounted on L10-5 Linear Ultrasound Probe	44
Figure 4.3 Hardware Setup of Picus Ultrasound Machine and PATRIOT Electromagnetic Tracking System	45
Figure 4.4 Polhemus PiMgr Application Data Record Screen	45
Figure 4.5 Cross-Wire Spatial Calibration Phantom	46
Figure 4.6 (a) Scanning Speckle Phantom (b) Typical B-scan Image of Speckle Phantom	46
Figure 4.7 Test Phantom Containing Pieces of Beef and Chicken Meat and A Piece of Rubber Mounted in Jelly.....	47
Figure 4.8 In-vivo Scanning of Human Thigh Tissue in Elevational Direction.....	48

Figure 4.9 Picus Ultrasound Imaging Machine Accompanied by Computer Connected to Frame Grabbing Card	49
Figure 4.10 L10-5 40 mm Linear Ultrasound Probe	50
Figure 4.11 PATRIOT System; Electronics Unit, Sensor and Source	51
Figure 4.12 Range vs. Resolution Curve of PATRIOT Tracking System.....	52
Figure 4.13 (a) Original Image of Ultrasound Machine Screen Acquired by Frame Grabbing Card (b) B-scan Image of Beef Phantom After Cropping.....	53
Figure 4.14 Plot of Position Readings Data Recorded for Beef Phantom Experiment in Two Dimensions (X and Y in mm)	54
Figure 4.15 Plot of Position Readings Data Recorded for Beef Phantom Experiment in Three Dimensions (X, Y and Z in mm).....	55
Figure 4.16 Total Translations between Successive Position Readings in mm for Beef Phantom Experiment.....	55
Figure 4.17 Measuring Difference between Successive B-scan Frames for Detecting Sudden Changes in Image Content.....	56
Figure 4.18 Deduction of Step Input Occurrence Time in Position and Image Streams.....	57
Figure 4.19 Matching Images and Positions.....	58
Figure 4.20 Arrangement of Coordinate Systems Involved in Spatial Calibration Experiment.....	59
Figure 4.21 (a) Scanning Cross-Wire Phantom (b) Typical B-scan of Cross-Wire Calibration Phantom	60
Figure 4.22 Z-Y-X Euler Angles Reported by PATRIOT Sensor as A Measure of Sensor's Orientation	62
Figure 4.23 Normal Distribution of Estimated X Values for Pixel at Origin of C for All B-scans Representing Image of Wires Crossing.....	64
Figure 4.24 Distribution of Estimated Y Values for Pixel at Origin of C for All B-scans Representing Image of Wires Crossing	65
Figure 4.25 Distribution of Estimated Z Values for Pixel at Origin of C for All B-scans Representing Image of Wires Crossing	65
Figure 5.1 (a) Grid of Patches Applied on B-scan Image of Speckle Phantom (b) Grid of Patches with Valid Patches Shown in White and Invalid Patches Shown in Gray	67

Figure 5.2 Surface Fitted on Measured Correlations between Particular Corresponding Patches of Two Frames for Different Amounts of In-Plane Offset between Them	70
Figure 5.3 Elevational Decorrelation Curves of Speckle Phantom for Six Patches from Column 1 of Grid but at Different Rows	73
Figure 5.4 Elevational Decorrelation Curves of Speckle Phantom for Six Patches from Column 4 of Grid but at Different Rows	74
Figure 5.5 Elevational Decorrelation Curves of Speckle Phantom for Six Patches from Column 8 of Grid but at Different Rows	75
Figure 5.6 Axial and Lateral Decorrelation Curves of Speckle Phantom for Six Patches from Column 1 of Grid but at Different Rows	76
Figure 5.7 Axial and Lateral Decorrelation Curves of Speckle Phantom for Six Patches from Column 4 of Grid but at Different Rows	77
Figure 5.8 Axial and Lateral Decorrelation Curves of Speckle Phantom for Six Patches from Column 8 of Grid but at Different Rows	78
Figure 5.9 FDS Decorrelation Curve Adjustment Using Only Two Adapted Data Points Corresponding to Elevational Distances Equal to 0.4mm and 0.8mm	81
Figure 5.10 FDS Decorrelation Curve Adjustment by Adapting All Data Points Based on Amount of Displacement for Data Points Corresponding to Elevational Distances Equal to 0.4mm and 0.8mm	82
Figure 5.11 (a) Typical B-scan Image of Human In-vivo Data Set (b) Typical B-scan Image of Speckle Phantom Data Set Divided into Patches by The Same Grid.....	83
Figure 5.12 (a) Typical B-scan Image of Beef Data Set (b) Typical B-scan Image of Speckle Phantom Data Set Divided into Patches by The Same Grid	84
Figure 5.13 (a) Typical B-scan Image of Chicken Data Set (b) Typical B-scan Image of Speckle Phantom Data Set Divided into Patches by The Same Grid	84
Figure 5.14 Elevational Distance Estimations for Chicken Data Set	86
Figure 5.15 Elevational Distance Estimation for Beef Data Set.....	86
Figure 5.16 Elevational Distance Estimation for Human Thigh Data Set.....	87
Figure 5.17 Systematic Errors	88
Figure 5.18 Difference against Mean for Elevational Distance Measurements of Chicken Data Set.....	90

Figure 5.19 Difference against Mean for Elevational Distance Measurements of Beef Data Set	90
Figure 5.20 Difference against Mean for Elevational Distance Measurements of Human Thigh Data Set	91

List of Tables

Table 5.1 Elevational Distance Estimations	85
Table 5.2 Limits of Agreement Calculated Using Bland-Altman Method for Different Data Sets.....	91

List of Acronyms

Acronym	Description
AC	Alternating Current
A-mode	Amplitude Mode of Ultrasound Imaging
B-mode	Brightness Mode of Ultrasound Imaging
CT	Computed Tomography
DC	Direct Current
DOF	Degrees Of Freedom
DS	Distribution Step
FAI	Femoro-Acetabular Impingement
FBM	Function-Based Method
FDS	Fully Developed Speckle
HFS	Hole-Filling Step
M-mode	Motion Mode of Ultrasound Imaging
MRI	Magnetic Resonance Imaging
PBM	Pixel-Based Method

PNN	Pixel Nearest Neighbor
PSF	Point Spread Function
RBF	Radial Basis Function
RF	Radio Frequency
RiIG	Rician Inverse Gaussian
RMS	Root Mean Square
VBM	Voxel-Based Method
VBMI	Voxel-Based Method with Interpolation
VNN	Voxel Nearest Neighbor
2D	Two Dimensional
3D	Three Dimensional

Chapter 1

Introduction

In this chapter an introduction to this thesis is provided along with an overview of the entire document and its organization. Additionally, a summary of the motivations and objectives leading to conduct this research, and also contributions of the thesis are delineated in this chapter.

1.1 Overview

About 50% of the mass of the human body in healthy adult men and women is formed by musculoskeletal system [1] and it is quite common for a person to suffer from numerous musculoskeletal injuries and diseases such as broken bones, arthritis and etc. throughout life. The main motivation leading to conduct this research was to focus on a particular musculoskeletal abnormality called Femoro-Acetabular Impingement (FAI). FAI is a condition of abnormal contact stresses and potential joint damage around the hip. Basically, a bony deformity or spatial malorientation causes the ball (femoral head) and socket (acetabulum) rub abnormally creating damage to the hip joint in this

condition. The damage can occur to the articular cartilage or the labral cartilage [2]. If we can achieve a thorough visualization of the whole hip joint it would help considerably in the clinical understanding and mechanisms of the abnormality and eventually in making decisions about the diagnosis and treatment procedure.

Fortunately, in the last decades musculoskeletal imaging has developed rapidly and largely due to the important developments in imaging capabilities of Magnetic Resonance Imaging (MRI), Computed Tomography (CT), and ultrasound [3]. Since ultrasound scanning, unlike CT, does not involve the use of ionizing radiation, and the examination is less time-consuming and traumatic for the patient than MRI, it has been introduced as the least invasive and least expensive imaging technique. Additionally, many other advantages of ultrasound imaging can make it as one of the most promising imaging modalities for assessment of musculoskeletal disorders. Ultrasound machines are easily available and relatively inexpensive to buy and maintain [4], the small and user friendly design of the ultrasound probes makes it a quite useful tool when joints are difficult to assess clinically, such as hip joint scanning [5], and they also take advantage of real-time scanning feature. However, there are also some disadvantages that can be considered as barriers in the clinical use of ultrasound imaging. One of these disadvantages is the limited field of view of ultrasound scans. Since the ultrasound probe is small, it has a limited field of view and cannot cover a large area in one frame. Therefore the diagnosis results of ultrasound imaging are quite dependent on the experience and knowledge of the clinician who has to manipulate the ultrasound transducer, generate a mental 3D view of tissue structure, and make diagnosis decisions based on this mental view.

The idea of developing 3D ultrasound imaging systems arises as a way to overcome the limitations of conventional 2D ultrasound images [6]. 3D ultrasound is able to provide extended field of view images and decrease the operator dependency for scan interpretation. There are a number of different techniques to construct a 3D volume using ultrasound 2D frames. One of these techniques which is known as freehand three-dimensional (3D) ultrasound, has attracted many researchers' attention due to its apparent simplicity and flexibility. In this technique, the clinician sweeps the ultrasound probe over the anatomy in an arbitrary manner and simultaneously the trajectory of the probe is recorded using a position sensor attached to it. The volume of anatomy can be constructed

then by matching the ultrasound data with their corresponding position in space [7]. This technique is the cheapest and most flexible approach which allows a large arbitrary volume to be recorded and visualized. However, it needs to be mentioned that there are some particular calibration processes and other considerations required to be met in order to achieve high quality 3D images and accurate results using freehand 3D ultrasound system.

1.2 Problem Statement

The aim of freehand ultrasound imaging is to construct a 3D ultrasound image by moving a 2D probe freely over the anatomy. Although an external tracking sensor can be used for the task of accurate position tracking, it imposes extra cost and need for calibration [8]. It is said that the requirement of the add-on position sensor is the most important barrier to pervasive clinical usage of freehand 3D ultrasound systems.

When we use a position sensor to record the motion of probe, some difficulties and challenges arise and it is required to overcome them in order to setup a 3D freehand system successfully. Firstly, it is required to do precise end-user calibration when using a position sensor. There are different ways to calibrate the sensor with respect to the probe and most of them are highly time consuming and subjective [9]. Secondly, using the position sensor inflicts cumbersome constraints on the scanning procedure. For example, the operator must maintain a clear line of sight between the probe and the cameras when using optical sensors, or must be careful not to deviate outside the sensor's operating region and to place the sensor far from metallic objects when using electromagnetic sensors. Thirdly, matching ultrasound images accurately with their corresponding position readings is a difficult task. The unknown latencies in both position sensing device and ultrasound machine can cause ultrasound image to be labeled with the position reading recorded some time after the image is actually acquired and it can highly affect the results. It is not surprising therefore that many researchers are investigating to introduce alternative sensorless freehand acquisition techniques and eliminate the need for the position sensor in 3D freehand ultrasound systems.

In the context of ultrasound imaging, the axial direction is defined in the direction of wave propagation from the transducer into the skin, the lateral direction is defined the other principal direction in the plane of the B-scan, and the elevational direction is defined

perpendicular to the plane of the B-scan. Any in-plane motion between two frames (translation in the axial and lateral directions, and also roll around elevational direction) can be accurately and reliably estimated using standard 2D registration techniques [10] [11]. The big challenge in sensorless image-based ultrasound tracking is the out-of-plane motion (translation in the elevational direction, and also rotations around axial and lateral directions) estimation. There are few approaches which have been tried to deal with this challenge so far. The most important one is the speckle decorrelation method [12]. The method is based on the idea that the correlation value of a specific model of speckle known as Fully Developed Speckle (FDS) can be used to estimate the out-of-plane displacement between images. The problem with this approach is that in real tissue, this kind of pattern is rare and the deviation of speckle pattern from the ideal FDS model decreases the accuracy of the out-of-plane motion estimation. Some alternative methods are introduced to solve this problem such as detecting FDS regions in images and applying method only on these regions or trying to find a way to consider the effect of both FDS and non-FDS regions in correlation measurement between images. However, highly accurate sensorless out-of-plane motion estimation between ultrasound images is an ongoing research problem which is receiving great amount of attention from researchers in the field.

1.3 Proposed Method

This thesis proposes a method for sensorless out-of-plane displacement estimation between ultrasound B-scan images that can be used in freehand 3D ultrasound applications. It was discussed in previous section that the most important approach used for solving this problem so far is speckle decorrelation method. The method is based on the fact that ultrasound beam focusing is imperfect in elevational direction. This imperfection causes the resolution cells of ultrasound images obtained in close adjacency to overlap in space and therefore, they image mostly the same scatterers. This causes the signal samples of these two images to be mutually correlated; the correlation decreases with the amount of overlap between resolution cells which is a function of distance. This phenomenon is called speckle decorrelation and indicates that there is a deterministic relationship between correlation and elevational separation.

The practical way to implement this idea is to create a speckle phantom which means an object that contains a great amount of randomly located ultrasound scatterers. The speckle phantom resembles FDS pattern, and by scanning it at known regular elevational intervals, a transducer-specific decorrelation curve can be fitted to the set of resulting correlation measurements. This curve can then be used to estimate distance between ultrasound images having their correlation. It is worth mentioning that since ultrasound resolution cell's width varies across and down the B-scans, it is required to divide the images into a number of patches in order to calibrate decorrelation curves and obtain a particular decorrelation curve for each specific patch.

As discussed before, the main challenge of using speckle decorrelation method is the rarity of FDS regions in ultrasound images of real tissue. The solution for this problem which is used in this thesis is an adoption of currently available Cambridge heuristic method [13] to be applicable on B-mode ultrasound images. The method considers the effect of both FDS and non-FDS regions and tries to compensate for the deviation of the real tissue correlation curve from its FDS calibrated one.

The main idea behind this method is that under isotropic medium assumption (which means that the coherency in the axial and lateral directions is the same as in the elevation direction), it is possible to correct for the out-of-plane deviation by knowing the amount of in-plane deviation from an ideal FDS curve. The practical way to perform this is to locally adjust calibrated correlation curve for every single patch. This means to compare in-plane correlation curves with their corresponding calibrated FDS curves and then adjust the out-of-plane curves based on this difference for each patch. In fact, the in-plane correlation is measured to find the percentage of coherent scattering in the patches, and the adjustment is based on this percentage. Since the resolution cell width is approximately four times larger in the elevation direction, the coherency effect and the elevational displacement are considered to be equal to in-plane effect/displacement multiplied by four. The fixed size of the pixels in the B-scan images causes encountering some limitations in implementing this method because the finest displacement that we can consider in axial and lateral direction is equal to the size of one pixel. Therefore, the finest elevational distance that we can consider is equal to size of one pixel multiplied by four ($0.1 \times 4 = 0.4$ mm for the B-scan images used in the analysis of this thesis) which is quite big for motion tracking tasks. It is

essential to adopt the curve adjustment task in such way that the shape of the curve is kept. In addition, the effect of the in-plane motion between successive frames should be considered to achieve better results since we are discussing a freehand system, and the motion of the probe is not constrained any direction. After successfully dealing with the challenges mentioned above, the adjustment of elevational FDS calibrated curves is achievable and it is possible to find the elevational distance between patches with a good accuracy based on the measured correlation between them from new adjusted curves.

1.4 Thesis Contributions

This section provides a list of the main research contributions of this thesis along with a brief explanation for each. However, the thorough explanation for these contributions will be covered in further chapters.

- Using B-mode ultrasound images instead of RF data: In this thesis we use B-mode images (B-scans), which are the most commonly used ultrasound data format in medical clinics, and it is the major difference between our work and most previous works done on sensorless out-of-plane motion estimation. Since RF data are not always available in clinical applications, investigation of speckle decorrelation method and specifically adaptation of currently available sensorless motion estimation approaches which separate FDS and non-FDS effect, on the B-mode ultrasound data would be a great help toward widespread clinical usage of sensorless freehand 3D ultrasound systems.
- Decorrelation curves adjustment in a new way: using B-mode images for sensorless out-of-plane motion estimation causes encountering some limitations in decorrelation curves adjustment. In this condition the finest possible displacement in axial and lateral direction is equal to the size of one pixel and since the resolution cell's width in elevational direction is nearly four times larger than the resolution cell's width in axial and lateral directions, the finest corresponding elevational displacement is four times bigger than the size of one pixel and it is a pretty large offset in motion tracking tasks. Therefore, we obtain only few adapted data points to create new decorrelation curves when using axial and lateral decorrelation curves to adapt elevational decorrelation curves.

In order to avoid decrease in accuracy, an algorithm is proposed here to adapt other data points in such way that the shape of the curve will be preserved based on the amount of displacement for the adapted points.

- True freehand system and real in vivo human experiment: In experiments of this thesis we are dealing with a true freehand system. It means that, unlike most studies on this topic in which the probe is mounted on a mechanical device allowing accurate translations only in elevational direction, motion of the probe here is totally unconstrained and is not limited in any directions. We also scan real human thigh tissue and apply the method on this *in vivo* data which are affected by the presence of both in-plane and physiological motion. However most studies on this topic apply the method only on *in vitro* data.
- Compensate for in-plane motion: Since freehand motion does not produce pure elevational translations, in-plane motion and out-of-plane rotations are also included in the motion between successive frames. It is therefore required to compensate for in-plane motion. In this thesis we adopt the idea in previous works to be applicable on B-mode images. The algorithm proposed here defines a range of potential offsets in axial and lateral directions for each patch. Then moves the patch within the possible offset ranges and calculate correlation coefficient between the corresponding patch in previous frame and the shifted patch in the current frames. Among all measured correlation coefficients it finds the maximum value and uses the maximum value in order to create and calibrate elevational decorrelation curves.

1.5 Thesis Organization

Chapter 1 provides an introduction to the concepts discussed throughout this thesis.

Chapter 2 provides background information about ultrasound physics governing image formation process, along with a brief description of basic ultrasound instrumentation, and different imaging modalities. Additionally, a discussion on the advantages of using ultrasound imaging modality in the musculoskeletal imaging field is provided.

Chapter 3 reviews the state of the art on the 3D ultrasound development, limitations of conventional 2D ultrasound, and different 3D ultrasound acquisition techniques. It goes

through the freehand 3D ultrasound technique then and provides a literature review on sensor-based and sensorless probe motion estimation methods.

Chapter 4 defines the mathematical model for statistics of ultrasound speckle and provides a mathematical formulation for calculating the correlation. It proceeds with providing an overview of the proposed methodology, detailed descriptions of experimental setup, ultrasound machine/probe and electromagnetic sensor hardware specifications, data acquisition process, and primary data processing routines.

Chapter 5 provides details about data processing algorithms including frames selection, in-plane motion compensation, and FDS decorrelation curves calibration and adjustment. It concludes with the evaluation of the method on test data and in vivo data, and a discussion of algorithm accuracy and limitations.

Chapter 6 concludes this thesis by providing a summary of the proposed experiments and algorithms, the major findings, and a number of recommendations for future works.

Chapter 2

Background Review

Ultrasound (the term is used to define sounds above the hearing range of humans) acoustic waves that are used for diagnostic medical applications are usually in the frequency range of 1MHz to 10 MHz in order to achieve both good resolution, which requires higher frequencies range, and good penetration, which requires lower frequencies range. The sources of ultrasound waves are piezoelectric transducers that convert electrical energy into mechanical energy and vice versa. The sound waves propagate through the human body. A portion of the waves reflect back to the transducer from the boundary between two types of tissue due to their different acoustic properties. The received signal is then processed in order to create medical images providing a visualization of the tissues inside the body [14]. A brief description of basic ultrasound physics and instrumentation along with its most common imaging modalities are provided in the following section.

2.1 Ultrasound Physics

Since ultrasound refers to high frequency sound waves, physics of ultrasound is governed by the physics of sound propagation. The sound waves used in diagnostic

medical ultrasound are longitudinal waves that propagate through physical media. As a result of this propagation, local movements are generated in the medium in the direction of the waves' propagation. Similar to all other waves, sound waves can be expressed by wavelength and frequency. Another important feature (specific to sound waves) to be considered is the speed of propagation which is determined by the medium the wave is traveling in [15]. The ultrasound image is a result of interactions between sound waves and body tissue. These interactions are described using terms such as reflection, scattering, refraction, and attenuation.

The basis of ultrasound image formation is the reflected echoes that return to the transducer. The point where ultrasound waves are reflected back when travelling through the body is at boundaries between tissues. The reflection is caused by changes in acoustic impedance between two different tissue types. The acoustic impedance (z) is the measure of ultrasound pulse transmission through a medium. The impedance is determined by the density (ρ) and speed of sound (c) in the medium as shown in Equation 2.1.

$$z = \rho c \quad (2.1)$$

The percentage of the ultrasound pulse that is reflected (R) from the boundary between two tissue types is dependent upon the acoustic impedances (z_1 and z_2) of the tissue as given by Equation 2.2. In addition, Equation 2.3 determines the percentage of the ultrasound pulse that is transmitted to the second medium.

$$R = \frac{I_r}{I_i} = \left(\frac{z_2 - z_1}{z_2 + z_1} \right)^2 \times 100 \quad (2.2)$$

$$T = 100 - R \quad (2.3)$$

At each biological interface with changes in acoustic impedance, part of the ultrasound beam is transmitted and part of it is reflected [16]. The difference in the acoustic impedance between two materials determines the amount of transmission and reflection of the ultrasound pulses; the larger the difference, the less pulses are transmitted and more are reflected [17]. The depth of the object causing the reflection can be calculated having the average speed of sound in tissue and the time between transmission and detection of the

reflected pulse. This will allow in displaying the object in its appropriate position in the image.

Equation 2.2 assumes that the tissue boundary interface is perfectly flat and smooth; this assumption may not be met in some surfaces within the body. The roughness of surfaces is assessed against the scale of wavelength. In such slightly-rough surfaces, the ultrasound waves are reflected over a range of angles [17]. On the other hand, reflection usually occurs at boundaries between different organs when there is a large interface and a big jump in acoustic impedance. Also, within an organ there are many small-scale variations in acoustic impedance. These small changes in acoustic properties cause reflections that do not follow the general laws of reflection. When the ultrasound waves are incident on such very small targets, where the size of target is comparable to or less than the wavelength, the reflection occurs over a large range of angles. If the target's size is much smaller than the wavelength, the wave will be scattered monotonically in all directions (see Figure 2.1 b). This phenomenon is called scattering which has an important role in the interpretation of ultrasound images. This importance can be explained by an example from the ultrasound imaging of musculoskeletal system. Tissues such as muscles have long-range structures in the direction of their fibers. These tissues do not scatter ultrasound waves monotonically in all directions when they are scanned in a way that ultrasound beam is parallel to muscle fibre direction. Accordingly, the appearance of the muscle in an ultrasound image may be different depending on the relative orientation of the ultrasound probe and the muscle fibers [15].

Another important issue related to scattering that should be briefly covered is acoustic speckle. Since real tissues are full of structure, movement, and organization on several length scales, they cannot be considered as homogenous media. Therefore, as ultrasound pulses travel within the tissue they may encounter many small particles (smaller than the ultrasound's wavelength) at any location in their way. Therefore, several echoes are generated simultaneously which may arrive at the transducer in such way that either emphasize (constructive interference) or debilitate (destructive interference) each other. These small particles that cause ultrasound waves to scatter in many directions are called scatterers. As the ultrasound beam is travelling through the tissues, with scatterers moving into and out of the beam, the interference alternates between constructive and destructive

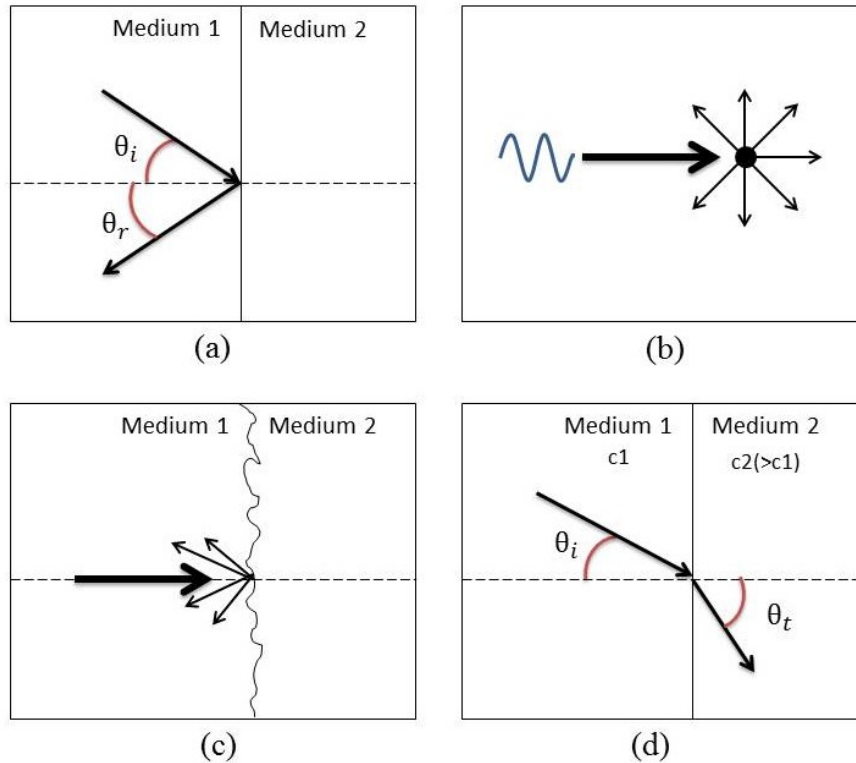


Figure 2.1 Different Types of Interactions of Ultrasound Waves with Tissue. (a) Reflection: the angle of reflection is equal to the angle of incidence when there is a large, flat, smooth interface between mediums. (b) Scattering: small targets scatter the wave over a large range of angles. (c) Diffuse reflection: a rough surface reflects the wave over a range of angles. (d) Refraction: when a wave crosses a boundary where there is a change in the speed of sound with an inclined angle, the direction of transmitted wave will change (Reconstructed from [15]).

modes resulting in a displayed dot pattern. This grainy appearance represents the interference pattern of the scattering distribution scanned. This phenomenon is called acoustic speckle and is a form of acoustic noise in ultrasound imaging. The grainy appearance of the acoustic speckle can be seen in Figure 2.2. We will return to this concept later in Section 3.3 for sensorless out-of-plane motion estimation.

Another important phenomenon occurs when the ultrasound waves are incident on an interface between two mediums by a non-zero angle (non-normal incidence), and the speed of sound changes from one medium to another. In this case, the direction of the transmitted wave changes when it crosses the interface (see Figure 2.1 d). This is known as refraction effect. Refraction can cause a target to be shown in a place in the image which is different

from its true position in the body [15]. This displacement error is known as lateral position error or refraction artifact in the image [17].

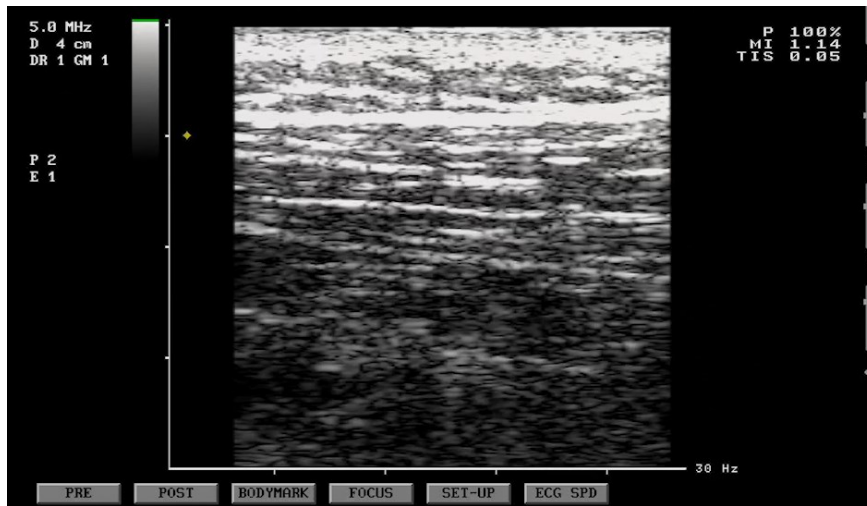


Figure 2.2 Typical Ultrasound B-scan Image of Thigh Muscle Displaying Grainy Appearance of Acoustic Speckle.

One other important effect in the interaction of ultrasound waves with tissue is attenuation. Attenuation is the loss of wave energy as it propagates through the tissue and it increases with the distance travelled. Attenuation may occur due to absorption of ultrasound energy by the medium, scattering of ultrasound out of the beam, and divergence of the beam with distance [15]. Attenuation is important to understand because it limits the imaging depth and its weakening effect on the image must be compensated by the diagnostic instrument [17].

2.2 Ultrasound Instrumentation

Ultrasound waves are produced by the piezoelectric transducers which convert electrical transmission pulses into ultrasonic pulses and vice versa. In other words, the transducer material is excited by the applied electrical signal causing it to expand and contract thus, producing pressure waves within the medium that is in contact with the transducer. Conversely, a pressure wave impinging on the transducer causes an electrical signal to be produced [18].

The basic components of a single transducer ultrasound probe are shown in Figure 2.3 where a narrow rectangular piece of piezoelectric crystal is housed within a case. The

backing material behind the crystal is designed to remove unwanted sound waves (either the backward travelling waves or the waves reflected back from the probe-tissue interface). The chosen material should be closely impedance-matched to the properties of the piezoelectric crystal so there would be complete transmission from piezoelectric crystal to the backing layer [19]. The large difference in the impedance between the crystal and patient tissue is overcome by placing a series of thin matching layers in front of the crystal to gradually decrease the difference in the impedance. These layers are chosen from the material with acoustic impedance of some intermediate value between those of the transducer element and the tissue [17].

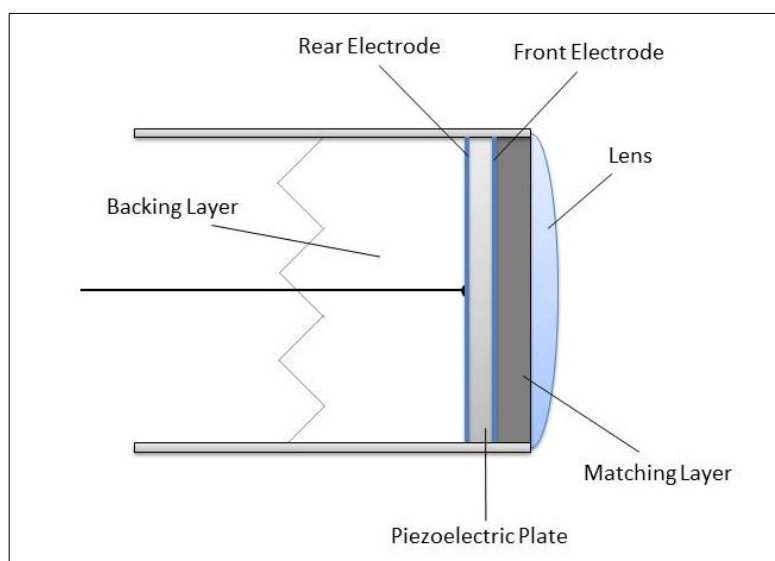


Figure 2.3 Basic Component Elements of Imaging Ultrasound Transducer (Reconstructed from [15]).

There are a variety of ultrasound probe scanning types: linear array, curvilinear array, and phased array [17]. Their names relate to the arrangement of the transducer material within the probe housing. The term transducer specifically refers to the piece of piezoelectric material; though is also commonly used to refer to the probe as a whole.

A linear probe contains an array of narrow rectangular pieces of piezoelectric crystals acting individually. The individual transducers in the array are fired in groups to produce a series of small ultrasound beams. There is a short delay after firing to allow the reflected ultrasound pulses to be detected by the transducers before the next pulse is fired. As different groups are fired, the origin of the sound beam moves across the face of the

transducer from one end to the other producing the same effect as produced by manual linear scanning with a single element group. The operation of a curvilinear or convex array is completely the same as linear array, but the transducer elements are arranged along a curved line rather than a straight line so the pulses travel out in different directions producing a sector-type image.

A phased array is similarly composed of a compact line of elements, but the voltage pulses are applied to most or all elements with small time difference between them (less than $1\mu\text{s}$). This time difference is called phasing and results in sound pulses to be sent out in a specific path direction. The time delays are automatically changed slightly in all iterations which cause the pulses to travel out in slightly different directions. Continuing these changes in beam direction will result in having echoes generated from one specific anatomic location with several viewing angles [17].

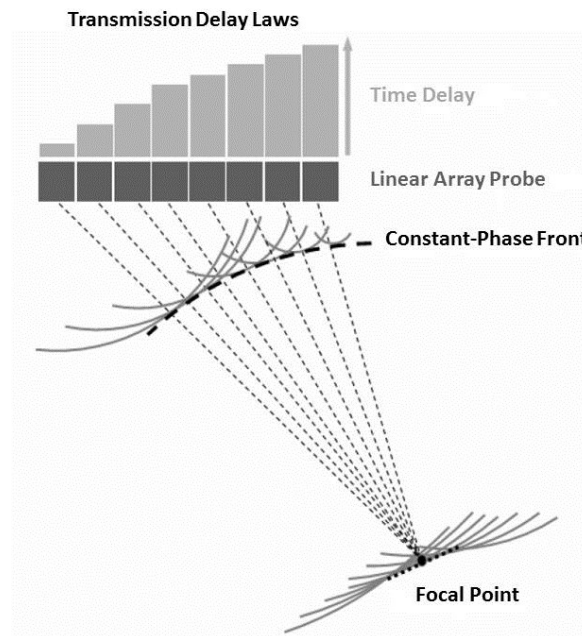


Figure 2.4 Principles of Phased Arrays; Focus at A Given Depth and Different Angles Achieved Using Different Time Delays [20].

2.3 Ultrasound Imaging Modalities (Modes)

Although the principles of ultrasound imaging are always the same (propagation of sound through the body and sensing the reflected echoes), there are several different

ultrasound modes. Each of these modes has benefits and drawbacks and is developed for different medical applications. A brief review of the most common ultrasound modalities is outlined in this section.

- **A-mode:** it is the simplest form of ultrasound imaging. A single transducer scans a line through the body. The envelope of the reflected echo signal is displayed as a function of depth. Firing the transducer repetitively will generate a series of these signals that can be displayed on an oscilloscope. This display is called A-mode or Amplitude mode [18]. A-mode is currently used in only a few specialist applications [15]. An example of creation of an A-mode signal can be seen in Figure 2.5.
- **M-mode:** an M-mode or Motion mode scan is generated by putting A-mode signals together as columns. The brightness of M-mode image is determined by the value of the A-mode signal [18]. The location of the beam is fixed during the M-mode scanning. This provides a single direct line of sight. Any motion of objects along this line is displayed by bright traces moving up and down across the image (see Figure 2.6). This is the reason this modality is called motion mode [15]. The mode is useful to image the areas that experience motion constantly, such as heart valves, and is usually displayed in conjunction with the ECG as shown in Figure 2.6.

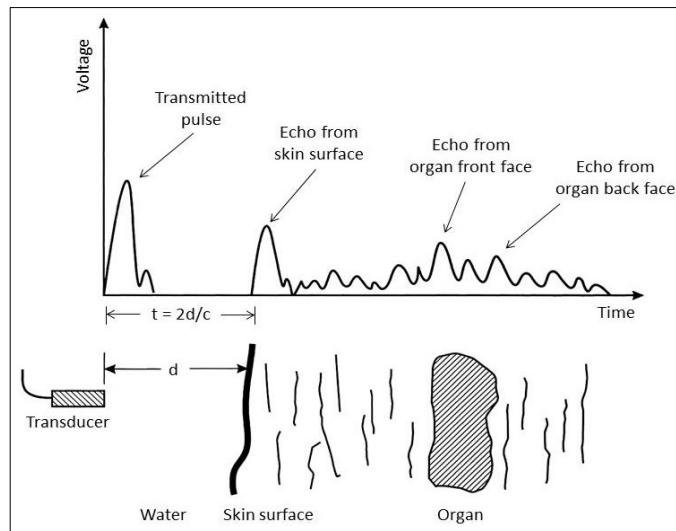


Figure 2.5 Generating an A-mode Echo Signal [18]

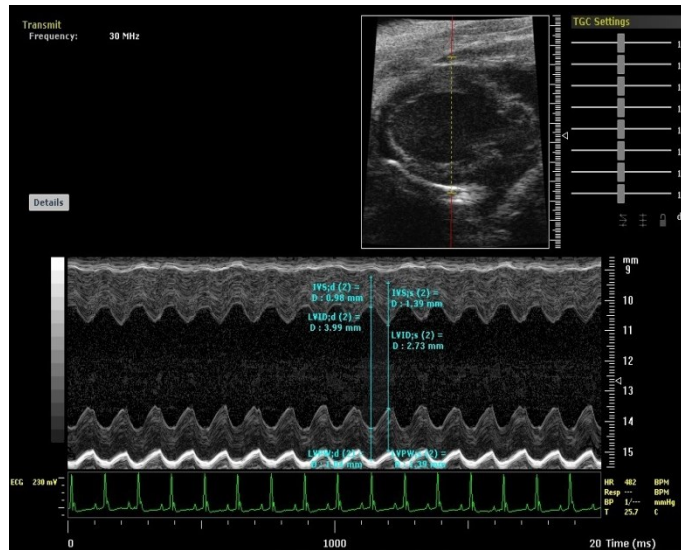


Figure 2.6 Typical Ultrasound M-mode Image of Heart Valve [18]

- **B-mode:** a B-mode or brightness mode scan provides a two dimensional display of the cross-sectional image of internal tissues under the probe. One way to do this is to move the single transducer laterally along the skin surface and collect the A-mode scan lines. Another way is to use array ultrasonic that contain several transducers and provide several A-mode scan lines. The A-mode signals are then brightness-modulated to generate B-mode image pixel values [18]. There are a number of probes that have been specifically designed for different B-mode applications [15]. An example of a typical B-mode scan is shown in Figure 2.2.

The modes that have been described in this section are the most common ultrasound imaging modes. However, there are some other modes such as the C-mode -constant range mode- which uses a gate to select data from a specific depth from an A-mode line, the Doppler mode that makes use of the Doppler effect in measuring and visualizing images, and the 3D-mode that uses a series of B-mode scan data to reconstruct the 3D images.

2.4 Ultrasound and Musculoskeletal Imaging

Among the wide range of ultrasound applications in the vast field of medicine, ultrasound imaging of the musculoskeletal system is of main interest to this research. The primary reason for conducting this research, as discussed in the motivation statement (Chapter 1), is to focus on a specific musculoskeletal abnormality in hip joint known as

Femoro-Acetabular Impingement (FAI). The size of impingement in this abnormality is in the range of millimeters [21] therefore it can be detected from ultrasound images of the hip joint.

Ultrasound imaging has been introduced as the least invasive and least expensive imaging technique in a review article by Kaplan et al. [22]. Details of all aspects of musculoskeletal imaging from different ultrasound scanners used in musculoskeletal applications to various injuries and disorders that could be examined were discussed in the article. The review suggests that ultrasound modality should be considered as the first choice in the diagnosis procedure before requesting further details which are often more resource-intensive imaging modalities.

Considering the technical aspects of ultrasound musculoskeletal imaging, it has been stated in the review article that high-resolution real-time ultrasound machines are good choices when examining soft-tissue structures because they can identify structure of interest rapidly and determine optimal scanning plane accurately. In addition, high-frequency transducers are able to image small superficial structure in the extremities of most soft tissues. High-frequency transducers have the advantage of providing optimal spatial and contrast resolution but the penetration depth and also the field of view are limited in this type of transducers. Therefore, lower frequency linear transducers are more appropriate choices for scanning large muscular areas (such as the thigh), where the increased penetration depth and larger field of view are required to see deep structures. The linear array transducers are also suitable for imaging superficial structures such as tendons because their beams are perpendicular to the superficial structures and the increased field of view is also provided. In comparison, curvilinear transducers have a small field of view in the near field and the beam is oriented obliquely relative to longitudinally oriented tendons. Generally, ultrasound images should be acquired in both longitudinal and transverse planes for examining all structures of the organ of interest. Acquisition of ultrasound images in both longitudinal and transverse planes will help to gain most information and provide an interpretation of three dimensional localization and measurement of musculoskeletal lesions and injuries. Additionally, the highly reflective nature of bone has made ultrasound ideal for evaluating the bone surface which can be an advantage when investigating a bone related disorder like FAI. There is a great amount of

publications that took advantage of the use of ultrasound imaging in different musculoskeletal related areas such as evaluation of complications of orthopedic implants [23], imaging soft tissue defects and diseases [24], and imaging bone and bone related diseases [25]. Comparative X-ray, MRI, and ultrasound images for a number of musculoskeletal complaints are shown in these publications while ultrasound being promoted as the best modality for musculoskeletal imaging.

Another recently published review article by Klauser and Peetrons [26] has reviewed and described all new developments in ultrasound technologies during the last decade. It has been concluded in the article that these developments are expanding the applications of ultrasound in the musculoskeletal field by offering the advantages of real-time performance, high tissue resolution, and relatively high speed all at a reasonable cost. One of these new developments is three-dimensional (3D) ultrasound that has helped address a number of limitations of conventional 2D ultrasound such as the need for the operator to interpret the series of 2D images viewed during scanning to form a diagnosis. It means that the inter-operator dependency in the interpretation of the images which could lead to differences in patient management can be removed by using 3D ultrasound. This topic will be discussed in detail in the next section.

Chapter 3

State of the Art Review

3.1 3D Ultrasound Imaging

In a 3D ultrasound system, as it can be expected from the name, the location of the ultrasound signal is known in three dimensions. It allows a whole volume data set to be generated rather than solely the conventional planar data set or image. The development of 3D ultrasound imaging is a way to overcome some disadvantages of conventional 2D ultrasound imaging. One of the main disadvantages of 2D ultrasound imaging is the dependency of the diagnosis results on the experience and knowledge of the clinician who has to manipulate the ultrasound transducer, generate mental 3D view of tissue structure, and finalize the diagnosis. This disadvantage has negative effects on the different applications of ultrasound imaging [6].

3D anatomical information (visualization) was demonstrated for the first time in the early 1970s by introduction of computed tomography (CT). After that, the development of 3D images from CT, and later Magnetic Resonance Imaging (MRI), created a major motive in the field of 3D visualization. In the beginning, extending ultrasound images to

3D was a slow progress because of the low quality of images. In the last decade, advances in ultrasound image quality along with advances in 3D image visualization have encouraged research investigators and commercial companies to develop 3D ultrasound imaging [27]. Since then, the quality of 3D images is improving and the range of clinical applications of 3D ultrasound is growing rapidly. A review of the limitations of conventional 2D ultrasound that can be addressed by the development of images to 3D, different 3D ultrasound scanning techniques, and the most common 3D reconstruction algorithms used in the field of 3D ultrasound will be covered in the following section.

3.1.1 Limitations of Conventional 2D Ultrasound

The major reason for the increase in the use of 3D ultrasound is related to the limitations of 2D viewing of 3D anatomy using conventional 2D ultrasound. The most important disadvantage of conventional 2D ultrasound imaging, as was mentioned briefly before, is the subjectivity and the variability of the results. It means that the diagnosis based on the mental 3D pictures from 2D images is greatly dependent on the skill and experience of the clinician and is not generalized; it can lead to incorrect decisions in the diagnosis and consequently in the treatment process [6]. Another limitation is that accurate quantified estimation of volumes (e.g. estimation of fetus volume, tumor volume, etc.) is difficult to acquire from 2D ultrasound images. Using simple measurements of height, width, and length in two orthogonal views to interpret the organ volume needs the assumption of an idealized shape (for example ellipsoidal) which is rare in real organs and would lead to low accuracy of the results [27].

Among other limitations of 2D ultrasound imaging are the inability to reproduce the same images at a later time and the inaccessibility to the optimal views. Assessing the treatment procedure or performing quantitative prospective or follow-up studies requires reproducing a particular image at later examinations. However, it is very difficult to adjust the transducer position in a way that the 2D ultrasound image plane would be exactly at the same anatomical position and orientation as it was in the previous examination. This difficulty makes conventional 2D ultrasound a poor imaging modality to be used for these applications. Because of anatomical restrictions, it is impossible to achieve images from some views by ultrasound transducers, for example planes parallel to skin surface. This

limitation results in inaccessibility of optimal image planes which are necessary for the diagnosis [6] [27].

The main goal of 3D ultrasound imaging is to overcome these limitations and to provide a better visualization of the anatomical structures inside the body to improve the diagnosis and the therapy procedure. 3D ultrasound is able to provide new images from views which previously could only be imagined by the clinician creating a mental picture from 2D information. Additionally, the quality of a conventional 2D image can be improved by compounding images acquired from different perspectives in a 3D ultrasound system.

3.1.2 3D Ultrasound Acquisition Techniques

Generally, there are four techniques to construct a 3D volume using ultrasound devices. In most of these techniques, 3D ultrasound is acquired by moving a conventional 2D probe over the area of interest and stacking up the resulting B-scans together to generate a 3D volume. A brief description of each of these techniques is provided in the following section.

- **3D ultrasound probes:** A 3D ultrasound probe is made up of a 2D array of transducer elements which can provide a pyramidal volume scan [28] [29]. The advantage of using this kind of probes is that the real-time imaging is possible, but the difficulty of wiring a large number of elements in a confined space results in images with lower resolution compared to 2D ultrasound.
- **Mechanically swept probes:** A mechanically swept probe uses a motor to move a 2D array within the probe housing therefore, a 3D dataset is constructed from combining a number of 2D B-scans acquired in a rapid session. Volumes of different shapes can be produced by this technique depending on the constraints applied on the motion of 2D probe by the motor. A schematic view of the different volume shapes is shown in Figure 3.1. It can be seen in the figure that the shape and the size of volume which can be achieved by this technique is limited.

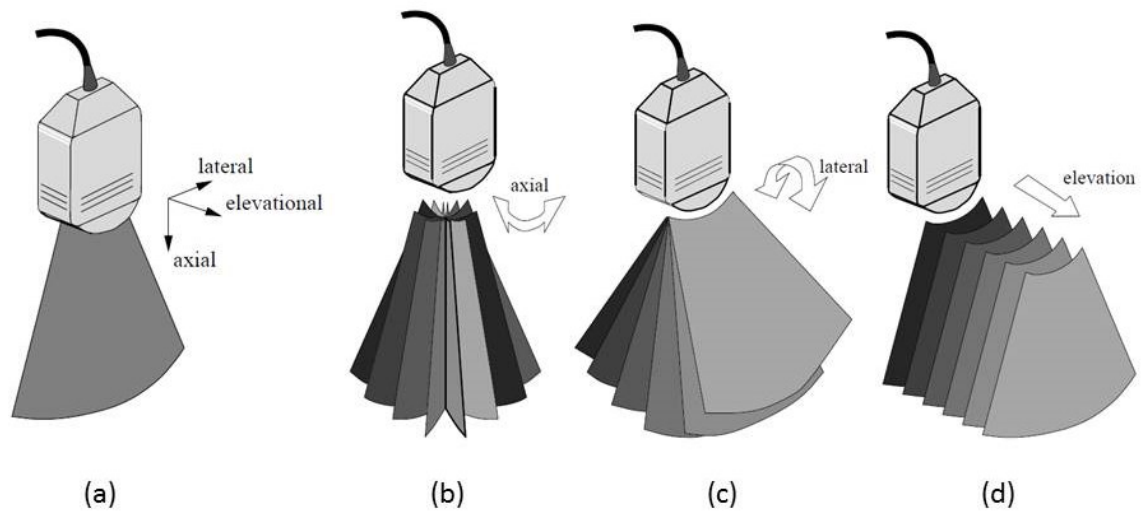


Figure 3.1 Definitions of Ultrasound Directions and Different Volume Shapes Produced by Mechanical Sweep Motions Assuming Sector-Shaped 2D Images. (a) Nomenclature of Ultrasound Imaging Directions. (b) Cone-shaped volume produced by a rotation about axial direction. (c) Fan-shaped volume produced by a rotation about lateral direction. (d) Prism-shaped volume produced by translation along elevational direction. [30]

- Freehand techniques with a position sensor:** Another technique to reconstruct a 3D volume using an ultrasound device is to track a conventional ultrasound probe by attaching a position sensor to it. In this technique the exact position of the probe is recorded by the attached position sensor while it is moving over the anatomy. The volume of anatomy can be constructed by matching the ultrasound data with their corresponding position in space. This technique is the cheapest and most flexible approach which allows a large arbitrary volume to be recorded and visualized [7]. The low cost of this kind of systems is the greatest advantage. In fact, they upgrade a conventional 2D ultrasound into a 3D system (According to the different ultrasound brands websites, conventional 2D ultrasound machines prices is in the range around \$10,000 while the range of price for 3D ultrasound machines is around \$100,000). Further details of engineering such freehand 3D system are provided in Section 3.2.
- Sensorless freehand techniques:** The principle is similar to the freehand technique with a position sensor. The clinician guides a conventional 2D ultrasound probe over the anatomy to collect a series of non-evenly spaced B-scans. By having the position

and orientation of each B-scan in 3D space the volumetric data can be reconstructed. The only difference is that in sensorless approach the position and orientation of B-scans is approximated by using the information in the images themselves and each frame is located with respect to the previous frame. Since there is no need for the additional position sensor in this technique, many limitations and challenges of using a regular freehand 3D system are overcome by it. A large number of researchers are attracted by the apparent simplicity of this approach and are trying to improve the accuracy and reduce the errors in the results. A detailed discussion of different approaches used so far to estimate the motion of the probe in sensorless freehand 3D systems is provided in section 3.3.

3.2 Freehand 3D Ultrasound System

As it has been discussed in previous sections, in the last decades many researchers have proposed systems for the construction and visualization of three-dimensional volumes from ultrasound images. One of the most important approaches is to use a freehand 3D system. In freehand 3D ultrasound, the probe is moved by hand over the area of interest in an arbitrary manner and its motion is measured by attaching some kind of position sensor to the probe. As a result, we will have a sequence of recorded B-scans, each labeled with its position and orientation in 3D space, to perform the 3D reconstruction. The freehand 3D ultrasound is the cheapest and most flexible way to achieve a 3D visualization of the organs from ultrasound images. The main components of this system are an ultrasound machine, a tracking system, and a reconstruction algorithm. Each of these components along with the required calibration processes will be described in the following sections.

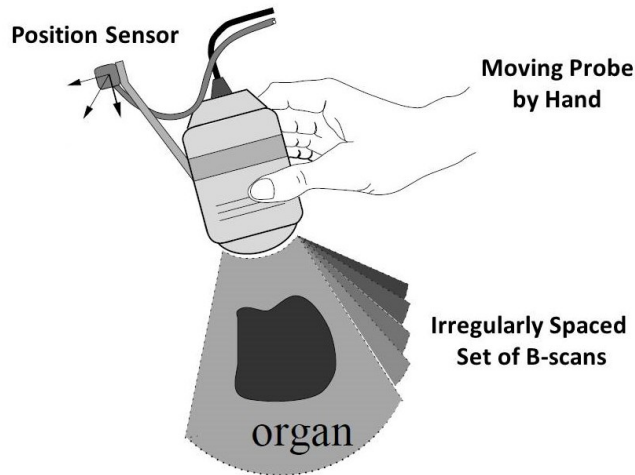


Figure 3.2 Schematic View of Freehand 3D Ultrasound Scanning [30].

3.2.1 Ultrasound Probe Tracking Systems

An important component of a freehand 3D system that has a strong effect on the 3D imaging results is the tracking system used to track the motion of the probe. In general, three types of tracking devices are used in freehand applications. A brief description of each device is provided below.

Mechanical arms: The motion of the probe can be defined and measured by attaching the ultrasound probe to a mechanical arm with six Degrees Of Freedom (DOF). The exact position of the probe is computed precisely by knowing the geometric properties of the mechanical arm and the existence of encoders at each articulation to report the angles. The accuracy up to 0.1 mm is achievable by some specific sorts of mechanical arms. The advantage of this technology is that the position of the arm is always available and the possibility of obstruction is zero (unlike other non-contact tracking systems). The main disadvantage of this device is its high cost and difficulty of use. Additionally, each mechanical arm is able to track only one object at a time and the accuracy can be affected if a force is applied to the arm without moving it [31].

Electromagnetic sensors: This kind of system consists of a transmitter and a receiver. The receiver is attached to the probe. While the probe is moving within the magnetic field generated by the transmitter, the receiver determines the motion of the probe by measuring the induced electrical current. There are two types of these electromagnetic devices

depending on the usage of either alternating currents (AC) or direct currents (DC) to generate the magnetic field. The motion measurement accuracy is in the range of 1 to 2 mm. The receiver needs to be placed near the transmitter within the generated magnetic field when using electromagnetic systems. Otherwise, the accuracy of the system will degrade rapidly. Another limitation of such systems is that the performance of electromagnetic sensors can be hampered by the presence of metallic (for AC sensors) and ferromagnetic material (for DC sensors) [32]. Experiments show that an error of up to 9.4 mm can be seen when a stainless steel rod is placed 10 mm away from the transmitter [33]. This limitation makes the use of electromagnetic sensors in medical surgery quite challenging because several metal objects are continuously being moved around in such environments. However, it remains a good option for other clinical applications because it provides a compromise between cost and accuracy.

Optical sensors: Optical tracking systems consist of multiple cameras observing one or more targets. The target is either passive or active markers. To accurately measure both position and orientation of the object and locating it in 3D space at least three markers are necessary. Using more markers will give higher accuracy. In general, the accuracy of these systems is in the range of 0.1 mm. Although the accuracy of these systems is exceptionally good, their high cost is a barrier for them to be used widely in clinical applications. Another disadvantage of using an optical tracking system is that a direct line of sight needs to be maintained between the cameras and the tracked targets.

3.2.2 Calibration Process

There are two calibration processes that have very important effects on the accuracy of every freehand 3D ultrasound system. The first one is about matching ultrasound images with their corresponding position readings carefully. This process is known as temporal calibration and involves estimating the latencies in the position sensing device and the ultrasound machine. In a freehand system usually the frame-grabbing card which is used to take the images automatically time-stamps the images, but we do not know how accurate this time-stamping is. Indeed, there might be significant latencies in the ultrasound machine and the frame-grabbing hardware which can cause the images to be time-stamped after some time delay. There might be an unknown latency in the position sensor readings

as well. The procedure of temporal calibration is to estimate these image and position reading latencies and the difference between them. The difference is then used to adjust time-stamps of position readings stream and images stream so they can be meaningfully match together. Generally, temporal calibration is carried out by a step input to be applied to both the image and position streams simultaneously. This can be achieved practically by holding the probe motionless against the skin and then yanking it away abruptly. It generates sudden changes in both the image content and position readings. Then we can use the difference in the timings of the observed eruption in position readings stream and images stream to adjust the timing of the two [34].

In freehand ultrasound system the position readings indicates the 3D location of the small sensor that is attached to the ultrasound probe. However, what we really want is the location of scan plane (each pixel of image) in 3D space. It is therefore, necessary to find the six-DOF rigid-body transformation between the position sensor coordinate system and image plane coordinate system. The process which is used to determine this transformation is called spatial calibration.

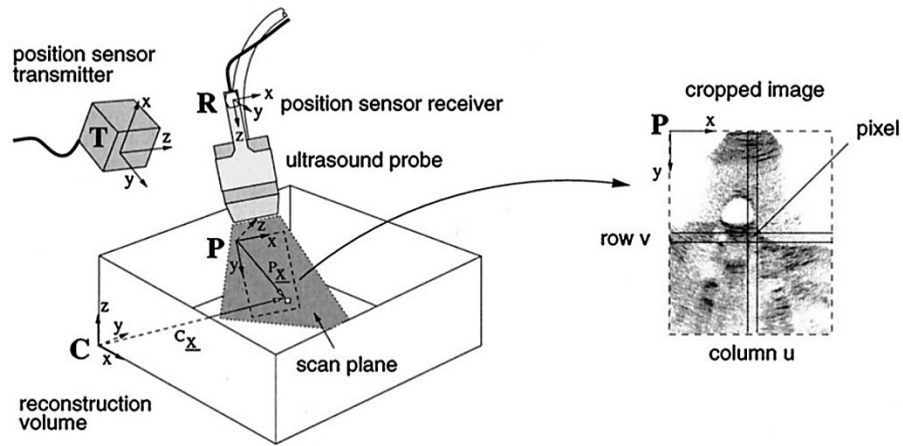


Figure 3.3 Coordinate Systems of Freehand 3D Ultrasound System [35].

The coordinate systems used for determining the image plane of an ultrasound probe in 3D space are shown in Figure 3.3 C is the world coordinate system that is in fact the coordinate system of reconstruction volume, T is the coordinate system of position sensing device (the transmitter in case of electromagnetic device), R is the coordinate system of the sensor mounted on the probe, and P is the coordinate system of the image plane.

To find the location of every pixel of every image relative to the origin of C in 3D space the location of every pixel's scan has to be transformed first to the coordinate system of the receiver R, second to the transmitter T, and last, to the reconstruction volume C. The multiplication of homogeneous transformation matrices provides the overall transformation that converts each pixel's location in the image to its location in 3D space. This transformation is displayed in equation 3.1.

$$\begin{pmatrix} x \\ y \\ z \\ 1 \end{pmatrix} = T_{C \leftarrow T} T_{T \leftarrow R} T_{R \leftarrow P} \begin{pmatrix} S_x u \\ S_y v \\ 0 \\ 1 \end{pmatrix} \quad (3.1)$$

In this equation, $T_{i \leftarrow j}$ shows the transformation from the coordinate system j to coordinate system i . u and v are the column and row indices of the pixel in the image, and S_x and S_y are scale factors with units of mm/pixel. Each of the transformation matrices in equation 3.1 has its own importance in the reconstruction process. $T_{T \leftarrow R}$ is collected directly from the position sensor readings and is the most clear-cut part of the equation. The purpose of including $T_{C \leftarrow T}$ in the equation is mainly for the convenience of reconstruction. However, it can be omitted, and the reconstruction volume can be aligned with the transmitter coordinate system. This omission, for instance, may place the B-scans a long way from the origin of C. The most challenging part of the equation is $T_{R \leftarrow P}$ which needs to be determined by spatial calibration [35].

By performing external measurements of the probe casing and its attached position sensor a straightforward estimate of the $T_{R \leftarrow P}$ can be achieved [36]. The main drawback of this method is the absence of external markers on the probe which makes it impossible to identify the origin of the image. This problem is also a concern in the case of magnetic sensors whose origin is embedded in the receiver casing. Another drawback of this method is the assumption that the image is centered on and perpendicular to the probe face, which is not necessarily true [37].

A more precise method for performing the calibration process is to scan an object with known geometric properties called a phantom. The way this method works is to image the phantom and determine its features on the ultrasound images. Since the locations of these features are known in the physical phantom space, the spatial relationship between the

position of the features in the image and the features on the phantom can be estimated in the calibration process. To find the unknown calibration parameters (three translational parameters and three rotational parameters of $T_{R \leftarrow P}$) a least squares minimization technique can be used. This technique estimates the parameters by minimizing the difference between the sets of features (points or lines) identified in the image and on the phantom [37].

3.2.3 3D Reconstruction Algorithms

The review article by Solberg et al. [38] has provided a comprehensive review and comparison of all freehand 3D ultrasound reconstruction algorithms. The reconstruction algorithms are categorized in three main groups as given below.

Voxel-Based Methods (VBM) function by creating a voxel grid. The algorithm then passes through each voxel in the grid and uses the information gathered from the 2D images to decide what value should be given to each voxel. There are different types of algorithms depending on the number of pixels that may contribute to the value of each voxel. Some methods use only one input pixel and assign it to the voxel while others use the average of many pixels. The most common algorithm in this category is the Voxel Nearest Neighbor (VNN) which assigns each voxel with the value of the nearest image pixel [39].

An example of using the VBM is in Stradx Specialized system (Medical Imaging Group, Engineering Department, University of Cambridge) [34]. Stradx is a real-time acquisition and visualization freehand 3D system that uses a reconstruction method which practically works as a VNN interpolation. Stradx is different from other reconstruction algorithms by not creating a voxel grid, but it is still placed in the same group as VNN. In fact, Stradx performs a fast VNN reconstruction of arbitrarily oriented 2D slices through the set of 2D images without creating a 3D volume.

Other examples of using the VBM are in the EchoPAC-3D software (GE Vingmed Ultrasound, Horten, Norway) [40] and the Solus system [41]. EchoPAC-3D software is another specialized freehand software that also uses Voxel-Based Methods with Interpolation (VBMI). VBMI uses an interpolation between several input pixel values to decide a voxel value. The Solus system is similar to the Stradx system in function, but the

only difference is that the Solus system implements a localized approach to a VNN interpolation instead of using a global VNN.

Pixel-Based Methods (PBM) which pass through each pixel in the input images and assign the pixel value to one or several voxels. These methods consist of two steps, the Distribution Step (DS) and the Hole-Filling Step (HFS). In the DS the input pixels are traversed and the pixel value is applied to one or several voxels often stored together with a weight value. The HFS goes through every voxel and fills the empty voxels. In most hole-filling methods there is a limit that indicates the difference between the known values and the values that can be assigned to the holes.

PBMs have been used widely in many researches. One of the commonly used methods in this category is Pixel Nearest Neighbor (PNN). An example of using PNN is in [42] where bin-filling is performed in DS, and then it traverses empty voxels and fills them from a local neighborhood in HFS. The following are two examples of other types of PBMs. In [43] [44] 3D kernel is applied to already filled voxels to determine impact on nearby voxels as HFS and in [45] a 3D kernel is applied to input pixels to determine impact on nearby voxels as DS.

Function-Based Methods (FBM) are utilized in order to create the voxel grid and they can estimate the functions of the input data. A particular function (like a polynomial) is chosen and the coefficients are determined to make one or more functions pass through the image pixels. Then, a regular voxel array is created using previous functions by evaluating them at regular intervals. Examples of the implementation of FBMs can be found in Rohling et al. [46] where Radial Basis Function interpolation (RBF) was used and in Sanches and Marques [47] where Rayleigh reconstruction and interpolation was used with a Bayesian framework.

In the review article by Solberg et al. [38], not only the algorithms are classified but a comprehensive comparison and discussion of different aspects of each algorithm is also provided. Based on this discussion, it can be concluded that the algorithms capable of generating results in real-time or close to real-time will be the most useful ones. The examples of these types of algorithms are implementations of VNN, PNN, using a small kernel around input pixels, or VBMI with interpolation over a limited area for each voxel. The algorithms that are slower might be added in order to support the fast algorithms.

Faster versions of the higher quality algorithms are the results of faster computers and fast optimized algorithms with the aim of optimizing the usage of 3D ultrasound reconstruction in image-guided surgery.

3.2.4 Challenges of Using Freehand 3D Ultrasound

The greatest barrier to pervasive clinical usage of freehand 3D ultrasound systems might be the requirement of the add-on position sensor [13]. The most significant challenges raised from the need for sensor are summarized as following.

It is essential to perform precise end-user calibration. There are different ways to calibrate the sensor with respect to the probe. Each of the calibration procedures have advantages and disadvantages however, most of them are highly time consuming and subjective. In addition, utilization of the sensor imposes cumbersome constraints on the scanning protocol. For instance, in case of using optical sensors, the operator must maintain a clear line of sight between the probe and the cameras. Also, the operator must be careful not to deviate outside the sensor's operating region and to place the sensor far from metallic objects while using electromagnetic sensors.

The other challenge is related to the matching of ultrasound images with corresponding position readings. Since there are unknown latencies in both position sensing device and ultrasound machine, matching between the images and positions can be encountered with the error which highly influences the results.

Considering all of these obstacles, it is not surprising that investigating alternative freehand acquisition techniques which dispense with the position sensor have been gained high attention among researchers in the field. In the next section, a review of sensorless probe motion estimation methods will be described in detail.

3.3 Sensorless Probe Motion Estimation

As it was discussed in previous sections, the main issue that stands in the way of universal use of freehand 3D ultrasound systems is the need for the motion sensor. The usage of sensorless freehand ultrasound mainly leads to removing the demand for a position sensor mounted on the transducer by using speckle tracking method. In the past two decades, measuring the relative pose of adjacent ultrasound images based on the

statistics of the receiving signal has been significantly increased compared to the measuring of the position of ultrasound transducer with a tracking sensor [8].

As it was mentioned briefly in section 2.1, the deviation of a coherent field phase front from its original form after encountering a random medium, causes a granular noisy pattern in ultrasound images so-called as speckle. In fact, speckle is a meaningful signal instead of only being a random noise; therefore, it can be applied in order to manifest information of the imaging system or the random medium [48].

The speckle pattern is mainly applied for tracking the ultrasound probe in freehand 3D ultrasound. The motion estimation task achieved by speckle-based tracking can be classified in two essential categories of in-plane and out-of-plane motions.

In the ultrasound image, the recovery of the in-plane motion can be estimated in an accurate and reliable way. Studies illustrate that the techniques based on image registration such as block matching [11] and radio-frequency (RF) tracking methods [49] are able to achieve credible results. Other successful examples of using standard 2D registration methods for in-plane-motion estimation between ultrasound images can be seen in [10] [50].

The main challenge related to the probe motion estimation is the out-of-plane motion. These are the three main categories that have been introduced in the literature for the purpose of out-of-plane motion estimation by using speckle tracking: correlation-based, regression-based, and learning-based methods. A summary of these three methods is provided below.

The correlation-based method is the most important one which is used in the majority of the research on ultrasound speckle tracking. To better understand this method, images A and B are examined among a sequence of ultrasound images (see Figure 3.4). The in-plane motion between images A and B includes the translation in the x and y directions and roll around the plane normal. As discussed before, these motions are simply determined using conventional 2D image registration techniques. The out-of-plane motion between A and B includes the translation in the elevational direction, tilt around the lateral axis, and yaw around the axial axis. To estimate these motions, corresponding patches in images A and B are considered. The imperfect elevational focusing of ultrasound probe causes the images separated by short distances to share content with each other (see Figure 3.5). In fact,

contents of the patches of these images depend on scatterers within overlapping resolution cells and are therefore correlated. The correlation coefficient increases with the degree of overlap between the resolution cells and decreases with the elevational separation between the images. Considering this fact and having a suitable decorrelation curve, a measured correlation between two patches can be used to find the corresponding elevational separation between them. By repeating this process for at least three non-collinear patches, the elevational separation, tilt, and yaw of A relative to B can be obtained [13]. The nominal decorrelation curves are different for each probe. They can be obtained by using acoustic physics and a detailed specification of the ultrasound scanner and probe. The more practical and popular way is to calibrate the decorrelation curves of the probe by scanning a speckle phantom and then measuring correlation coefficients directly from the images for different elevational offsets.

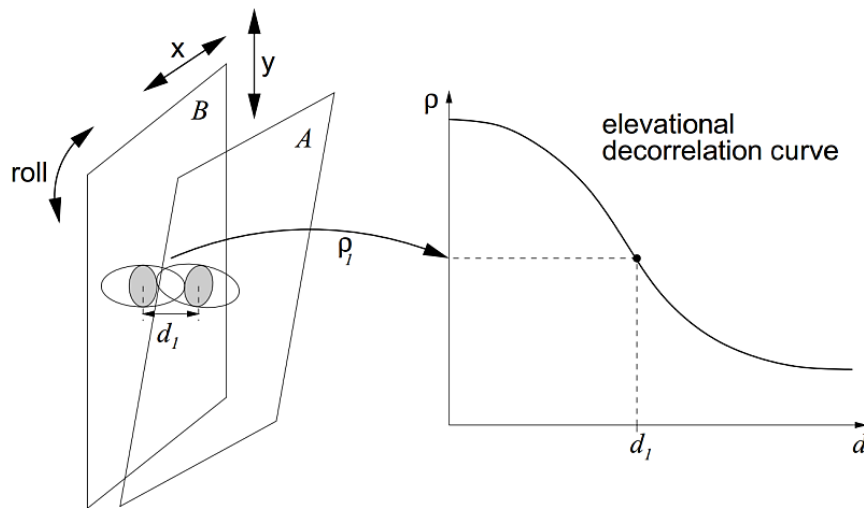


Figure 3.4 Principles of Elevational Speckle Decorrelation [13]

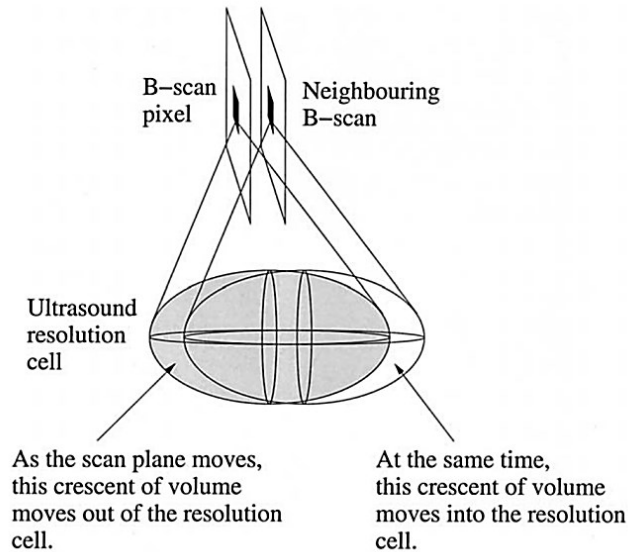


Figure 3.5 Two Pixels on Adjacent B-scans and Corresponding Ultrasound Resolution Cells. The imperfection of elevational focus in the ultrasound probe causes neighboring pixels to share content with each other [10].

The theory behind speckle decorrelation method applies only to Fully Developed Speckle (FDS), but real tissue contains regions of coherent scattering too. This is a serious difficulty with speckle decorrelation method because regions of coherent scattering decorrelate at a slower rate than regions of FDS and it decreases the accuracy of motion estimation in the images of real tissue. One solution to this problem is to develop algorithms to automatically detect FDS regions in the images and to obtain elevational distance estimates in these regions only. Examples of researches that increased the accuracy of motion estimation by using FDS detection algorithms can be found in [12] [51] [52].

The rarity of the FDS patches in images of real tissue is a main concern among others in out-of-plane motion estimation [13]. The result of this rarity is that very few FDS patches are found through the whole image, and the rest of the information in the image remains unused. In addition, the accuracy of FDS detector can influence the results. This means if there is any coherency in the speckle or if the statistics of the speckle deviates from FDS, the out-of-plane estimation will show significant error [8].

To solve this problem, some alternative approaches are developed that consider the effect of FDS and non-FDS distributions in the statistical distribution of the speckle pattern

jointly. For example, in [13], a heuristic technique is used to quantify the amount of coherency at each point in the B-scans by examining the axial and lateral correlation functions. This technique leads to the creation of the adapted elevational decorrelation curves which allow for the effect of coherent scattering to be considered. Another example is in [48] where a framework is created to separate coherent and non-coherent effects in every patch of the images based on a Rician Inverse Gaussian (RiIG) statistical model.

The second category is regression-based methods [10]. The principle of these methods is similar to the correlation-based methods. The best linear estimation of a circularly Gaussian distributed Radio Frequency (RF) signal correspondent to a FDS pattern is determined by these methods. This linear estimation is closely related to the correlation of speckle patches.

The third category is learning-based methods. The usage of learning-based methods for out-of-plane motion estimation of ultrasound images has been introduced recently [53]. These new methods calculate a scale factor based on training data to adapt the nominal correlation curve to it. The learning-based approach proposes a new method for estimating the elevational correlation length of ultrasound signals in a specific media by learning its relationship to in-plane image statistics. The learning process is performed based on the dataset of synthetic ultrasound images that are generated from virtual phantoms of different micro-structure.

In spite of the high number of researches conducted on sensorless out-of-plane motion estimation of ultrasound imagery, highly accurate out-of-plane motion estimation is not yet achieved and none of the efforts succeeded in completely solving the problem. As a result, estimating the accurate out-of-plane motion between ultrasound images and engineering a sensorless freehand 3D ultrasound system are ongoing research problems.

Chapter 4

Methodology

It was discussed in Chapter 1 that the objective of this thesis is to introduce a sensorless out-of-plane ultrasound transducer motion estimation method for freehand 3D ultrasound application. This is done by using an imaging phenomenon known as speckle decorrelation. In this thesis we use B-mode images (B-scans); this is the major difference between our work and most previous works which use of the RF signal. Since the RF signal is not always available in clinical environments, adaptation of currently available sensorless motion estimation methods for B-scan images which are commonly used in medical clinics would be a great help. A basic review of the fundamental principles of ultrasound image formation and interpretation along with the physics governing the speckle decorrelation phenomenon was provided in the Chapter 2. The information in Chapter 2 is essential for the reader to follow the discussions presented in this chapter; which will provide a more detailed and mathematically formulated description of speckle formation process and correlation formulation. Additionally, an overview of the proposed framework, a comprehensive description of the experimental setup along with the hardware specification of the ultrasound imaging system and electromagnetic motion

tracking sensor, and a detailed explanation of primary data processing routines are provided in this chapter.

4.1 Statistics of Ultrasound Speckle

Since the speckle pattern does not represent any of the scanned objects in the ultrasound image, it is usually considered to be a type of noise. Therefore, it is not surprising that a variety of “speckle reduction” and “de-speckling” methods have been developed and applied on ultrasound images in order to improve the image contrast for visualization [54] [55] or to perform image processing tasks that are based on large obvious displayed geometries and boundaries such as multi-modality image registration [56], sketching organ boundaries [57], or interpolation of freehand 3D ultrasound data [58]. It should be made clear that speckle is not a random noise. The reason that can prove this claim is that if we scan a specific object with a specific transducer in a specific configuration twice, the speckle pattern in these two images will be exactly the same. This example shows that the speckle is a repeatable meaningful signal and not just a random noise. The speckle signal can be used to interpret information about the target medium micro-structure and the physical characteristics of the transducer. Since the speckle pattern is generated by the spatial organization of scatterers (particles of size smaller than ultrasound’s wavelength which cause ultrasound waves to scatter in many directions), and the spatial organization of scatterers is different for different type of tissue; therefore, the speckle patterns can be used in diagnostic procedures. Examples of the use of speckle textural analysis for diagnostic tissue characterization tasks can be found in [59] [60] [61] [62]. In this thesis, the speckle is also considered as a meaningful pattern and is used for both tissue and transducer characterization. The mathematical explanation and essential assumptions underlying the analysis of this thesis are provided in the following sections.

4.1.1 Statistical Modeling of Speckle

Estimation of the displacement between two image planes based on the changes of the backscattered signal at two different positions is the eventual goal of out-of-plane motion estimation. The reflected signal received by the transducer carries information resulting from two different sources: the medium and the ultrasound beam. If we can distinguish

between the effect of the ultrasound beam and the effect of the medium on the backscattered signal (by knowing the characteristics of the ultrasound beam which are always constant), we can interpret the image plane motion directly from the changes in the medium effect which is practically interpreted from the statistical changes in the properties of the speckle. Therefore, it is an essential requirement to statistically model the speckle formation process and to predict the effect of out-of-plane motion on the statistics of the receiving signal.

In ultrasound imaging, reflected signals from a specific scatterer may hit other scatterers on their way back to the transducer. This phenomenon is called multiple reflection but and it is assumed that the amplitude of these multiply reflected signals received at the transducer is always negligible. The assumption is known as weak scattering condition, and under this assumption the ultrasound imaging process can be modeled as a linear system. With a linear probe, the ultrasound wave propagates in axial direction (y direction) and the RF signal can be demonstrated by Equation 4.1.

$$\varrho(x, y, z) = (h * \zeta)(x, y, z) \quad (4.1)$$

In the equation, h represents the transducer's Point Spread Function (PSF) and ζ shows the scatter function describing the medium. Validity confirmation of this linear systems model and the way to compute the PSF h for particular transducer specifications can be found in [63] [64]. h is assumed to be a pulse to satisfy the purpose of this discussion. It can be approximated as a sinusoidal wave with zero mean modulated by a Gaussian envelope. The envelope of the transducer's PSF is often called as the resolution cell. The scatter function ζ is determined as a summation of N_s point scatterers as shown in Equation 4.2.

$$\zeta(x, y, z) = \sum_{i=0}^{N_s} e_i \text{Dirac}(x - x^{(i)}, y - y^{(i)}, z - z^{(i)}) \quad (4.2)$$

In Equation 4.2 Dirac stands for the Dirac impulse function, e_i , $x^{(i)}$, $y^{(i)}$ and $z^{(i)}$ represent the strength or echogenicity, and x , y , z represent the location of the scatterer i . The first order statistics of ϱ can be determined depending on how densely the scatterers

fill the resolution cell of the ultrasound transducer and their spatial arrangement with respect to the incident ultrasound wave. If the scatterers have a uniform distribution in space and their strength is not dependent on location, ρ will ordinarily have zero mean. Moreover, if the number of scatterers within the resolution cell were large, ρ will have a Gaussian distribution with zero mean according to the central limit theorem [65]. This condition is known as Rayleigh scattering, and the speckle pattern generated under this condition is called Fully Developed Speckle (FDS). The Rayleigh distribution is the basic speckle statistical model which is commonly used for speckle tracking applications.

In addition to the first order statistics, the second order statistics are also of a great importance when speaking in the ultrasound speckle context. The second order statistics describe the dispersion of the differences between ultrasound signal samples as a function of their respective locations. The reason why second order statistics are important is because these signal samples cannot be handled as they are statistically independent. In other words, if the resolution cells of the finite size are located in space in a way that their center is matched to two neighboring points, they overlap in space and therefore, they image mostly the same scatterers. This causes the signal samples of these two images to be mutually correlated; the correlation decreases with the amount of overlap between resolution cells which is a function of distance. This phenomenon is called speckle decorrelation. The second order statistics of ultrasound speckle are usually delineated in terms of autocorrelation functions. They depend solely on the transducer's characteristics under Rayleigh scattering conditions or fully developed speckles. In other words, in such cases, the point spread function h determines the second order statistics of ultrasound speckle by its own [66]. It can be shown that under Rayleigh scattering conditions, if the resolution cell has an approximate Gaussian shape, the normalized autocorrelation function or the decorrelation curve of the echo intensity signal will be a Gaussian function of distance [10] [64]. It has been shown by Chen et al. [67] that the Gaussian function is a very good approximation even in case of more realistic transducer's point spread functions.

4.1.2 Correlation Formulation

As it was mentioned before, the volume of space that is occupied by the ultrasound pulse is referred to as a resolution cell. Practically speaking, it is not possible to distinguish

between the scatterers indwelled in the same resolution cell. Nevertheless, if two resolution cells have an amount of overlapping, the distance between them can be estimated based on the amount of correlation between their receiving signals. The correlation is a result of the effect of the same scatterers in the overlapping space. The precise form of the autocorrelation function or simply the decorrelation curve can be obtained using a simplified model of ultrasound imaging. Under Rayleigh scattering condition and hence for fully developed speckle [66], it is shown that the Pearson correlation coefficient between two patches of backscattered intensity signals I_1 and I_2 is determined by Equation 4.3; while the corresponding formula for the backscattered amplitudes A_1 and A_2 is given by Equation 4.4.

$$\rho(I_1, I_2) = \lambda^2 \quad (4.3)$$

$$\rho(A_1, A_2) = \frac{4E(\lambda^2) - 2(1 - \lambda^2)K(\lambda^2) - \pi}{4 - \pi} \quad (4.4)$$

In Equation 4.4 K and E indicate complete elliptic integrals of the first and second kinds, respectively. Assuming that the resolution cell has a Gaussian shape and consequently approximation of the decorrelation curve by a Gaussian function, the parameter λ is dependent to the standard deviation of the resolution cell width in elevational direction σ as it is shown in Equation 4.5 [10].

$$\lambda^2 = \exp\left(\frac{-\delta^2}{2\sigma^2}\right) \quad (4.5)$$

In Equation 4.5, δ represents the separation distance of the patches in elevational direction. It is shown by the equation that there is a definite relationship between correlation ρ and elevational separation δ . The resolution cell width σ is not constant all over the scan plane, and it varies across and down the B-scan. The change in resolution cell width is especially more obvious in axial direction; this means that the resolution cell width changes greatly with respect to the depth. As a result, different decorrelation curves are required at different positions of the scan plane. Theoretically speaking, σ can be computed for different positions of the scan plane by having the detailed specification of

the ultrasound probe and by using the acoustic physics principles. However, the more practical way is to calibrate the decorrelation curves of a specific ultrasound probe by scanning a speckle phantom and then measuring correlation ρ directly from B-scans for different elevational offsets δ . This thesis has taken advantage of this second approach.

4.1.3 Out-of-Plane Motion Estimation Using Speckle

As it was discussed, the decorrelation curve is independent from the medium under Rayleigh scattering condition therefore the elevational distance between two different ultrasound images obtained in close adjacency by the same transducer can be estimated by the use of second order statistics of fully developed speckle patterns. The practical way to do this is to create a speckle phantom which means an object that contains a great amount of randomly located ultrasound scatterers. The speckle phantom resembles Rayleigh scattering conditions, and by scanning it at known regular elevational intervals, a transducer-specific decorrelation curve can be fitted to the set of resulting correlation measurements. This curve can then be used to estimate distances having the correlation measurements. To obtain a set of images with known elevational intervals, we need to somehow measure the position of each image while scanning the speckle phantom. In this thesis, an electromagnetic position sensor is attached to the ultrasound probe to track the position and the orientation of the probe during the experiment.

4.2 Experimental Procedure and Data Acquisition

4.2.1 Overview of Proposed Framework

A brief summary of the framework proposed by this thesis is provided in this section. The block diagram of the proposed framework which shows the whole process as simple steps is also shown in Figure 4.1. Each of the steps shown in the block diagram will be reviewed and described thoroughly in the following.

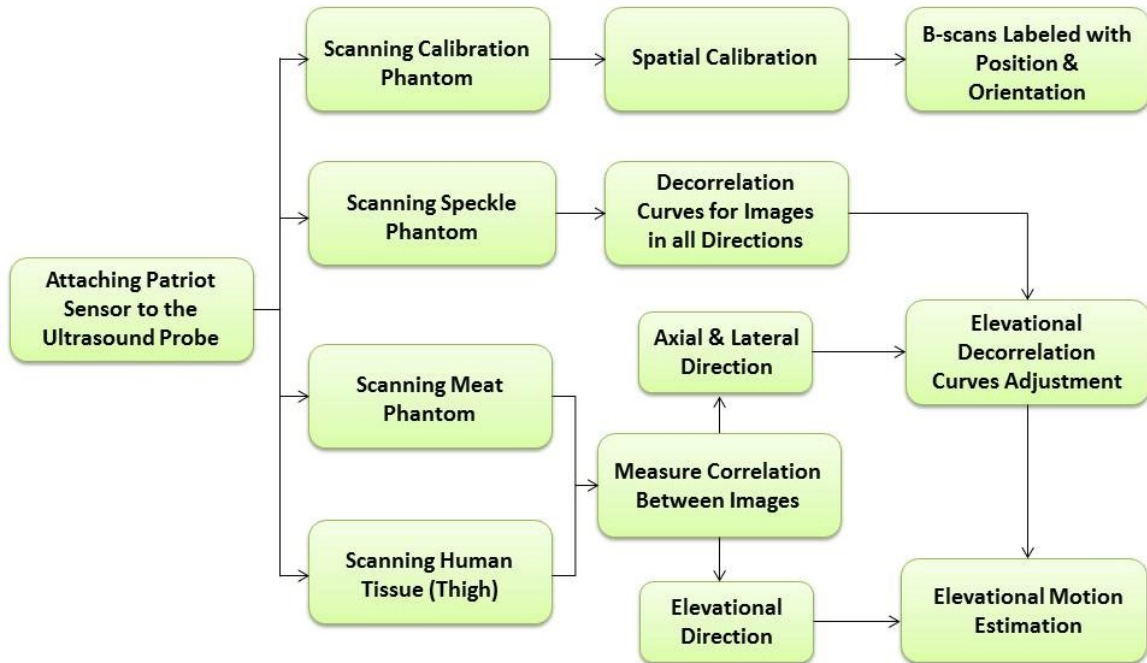


Figure 4.1 Block Diagram of Experimental Procedure and Proposed Methodology

After attaching electromagnetic sensor to the ultrasound probe, a spatial calibration phantom is scanned as the first experiment. This is done because we need to obtain the exact position of each pixel in the images according to the position data recorded for the small sensor attached to the probe. Also, at the beginning of all experiments, a temporal calibration step is performed to match each position reading with the corresponding B-scan image. The details on how temporal and spatial calibration processes are conducted in this study are provided in the following sections. After performing temporal and spatial calibration successfully, we can scan the speckle phantom where we will end up with a set of ultrasound images of fully developed speckles with known elevational separation distance. To calibrate the decorrelation curves, first the images are divided into a number of patches, then the correlation between corresponding patches in the images with specific separation distances are measured. The decorrelation curve is then fitted to the set of resulting correlation measurements for each patch and finally, a particular decorrelation curve is obtained for each specific patch for the particular ultrasound transducer used in the experiments. In the next step, a set of real tissue phantoms including beef phantom and chicken phantom, which are called test phantoms, are scanned to observe how these curves can be utilized to estimate the elevational distance between ultrasound images of real

tissues, and to evaluate the validity of the method. In addition to test phantoms, an experiment is also conducted on human thigh tissue to check the results in a more realistic clinical condition. In such clinical conditions, real human tissues are scanned, and issues such as physiological motion artifacts can affect the images' content.

As discussed before, the main challenge when using speckle decorrelation method is that real tissue images contain regions of coherent scattering. In fact, the regions which mostly contain fully developed speckles are quite rare in images of real tissue. The solution for this problem which is used in this thesis is an adoption of the Cambridge heuristic method which considers the effect of both coherent and non-coherent scatterings and compensates for the deviation of the real tissue correlation curve from its FDS calibrated one [13]. The main idea behind this method is that under isotropic medium assumption (which means that the coherency in the axial and lateral directions is the same as in the elevation direction), it is possible to correct for the out-of-plane deviation by knowing the amount of in-plane deviation from an ideal FDS curve. The practical way to perform this is to locally adjust calibrated correlation curve for every single patch. This means to compare in-plane correlation curves with their corresponding calibrated FDS curves and then adjust the out-of-plane curves based on this difference for each patch. In fact, the in-plane correlation is measured to find the percentage of coherent scattering in the patches, and the adjustment is based on this percentage. Since the resolution cell width is approximately four times larger in the elevation direction, the coherency effect and the elevational displacement are considered to be equal to in-plane effect/displacement multiplied by four. The fixed size of the pixels in the B-scan images causes encountering some limitations in implementing this method because the smallest distance that we can consider in axial and lateral direction is equal to the size of one pixel (0.1 mm here). Therefore, the smallest elevational distance that we can consider is 0.4 mm (0.1×4) which is quite big for motion tracking tasks. It is essential to adapt the curve adjustment task in such way that the shape of the curve is kept. In addition, the effect of the in-plane motion between successive frames should be considered to get better results since we are discussing a freehand system, and the motion of the probe is not constrained any direction. Details on how these challenges are faced and resolved in this thesis are explained by detail in Chapter 5. After successfully deal with the challenges mentioned above, the adjustment of elevational FDS

calibrated curves is achievable and it is possible to find the elevational distance between patches with a good accuracy based on the measured correlation between them from new adjusted curves. This procedure is performed on images of test phantoms and real human tissues, and the results are shown in Chapter 5.

4.2.2 Experimental Setup and Data Acquisition

The experimental setup is consisted of the ultrasound imaging machine and the electromagnetic motion tracking system. The sensor of the electromagnetic system is attached firmly to the ultrasound probe (see Figure 4.2). The source of the electromagnetic field is placed in a location on a wooden table to be both far from large metallic objects, such as desks or cabinets, and near the sensor so the sensor would be in the range during all experiments to have a good performance. The arrangement is shown in Figure 4.3. PATRIOT sensor was connected to a personal computer running Windows 7 via USB interface and the position readings data were displayed and recorded by Polhemus PiMgr application on the computer. The position data are updated and recorded with a sampling rate of 60 Hz. Figure 4.4 shows the PiMgr display screen and the way that the position and orientation data are reported and recorded by this application.



Figure 4.2 PATRIOT Electromagnetic Sensor Mounted on L10-5 Linear Ultrasound Probe



Figure 4.3 Hardware Setup of Picus Ultrasound Machine and PATRIOT Electromagnetic Tracking System

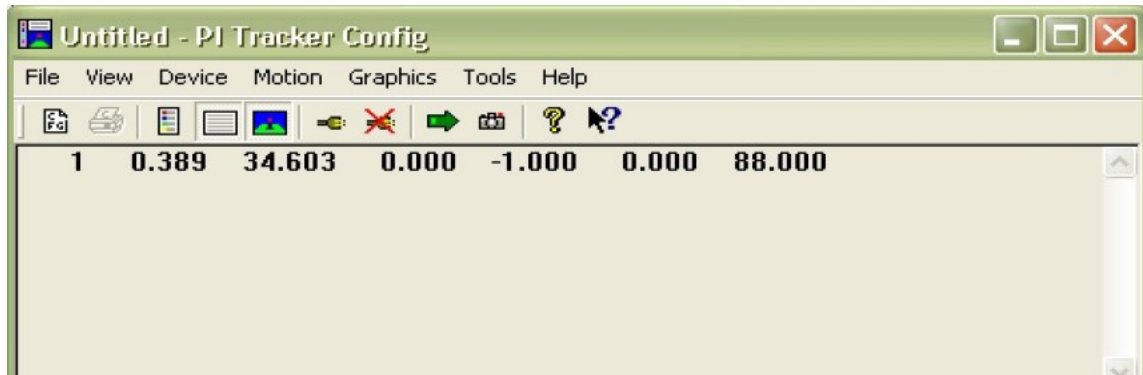


Figure 4.4 Polhemus PiMgr Application Data Record Screen

Specific experimental phantoms including spatial calibration phantom, speckle phantom, and beef and chicken phantom were prepared:

- Spatial calibration phantom used in the experiments of this thesis was a cross-wire phantom made up of two crossing nylon wires of a diameter of 1 mm mounted in Agar jelly as shown in Figure 4.5.

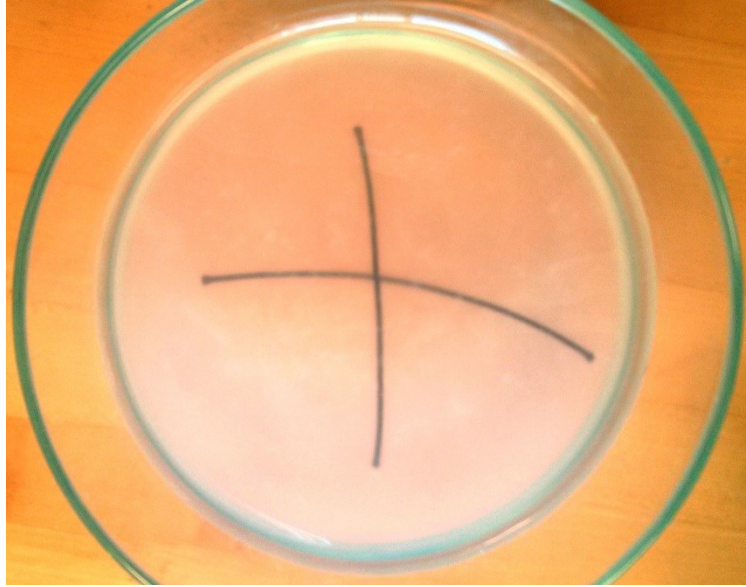
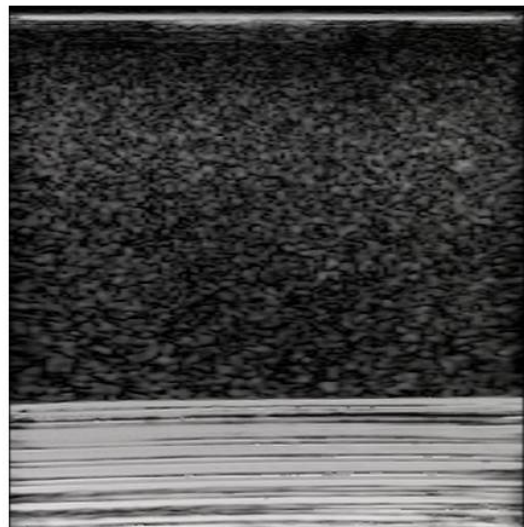


Figure 4.5 Cross-Wire Spatial Calibration Phantom

- Speckle phantom was made by stirring graphite powder and agar powder into hot water (trying to make a uniform distribution of powder in the phantom) and then putting them in the refrigerator to become solid. The approximate amount was 3 gr of graphite powder per 100 ml of water. The speckle phantom and one sample ultrasound image obtained by scanning it are shown in Figure 4.6.



(a)



(b)

Figure 4.6 (a) Scanning Speckle Phantom (b) Typical B-scan Image of Speckle Phantom

- Test phantom contains pieces of beef and chicken meat and a piece of rubber all with known dimensions in jelly as shown in Figure 4.7.

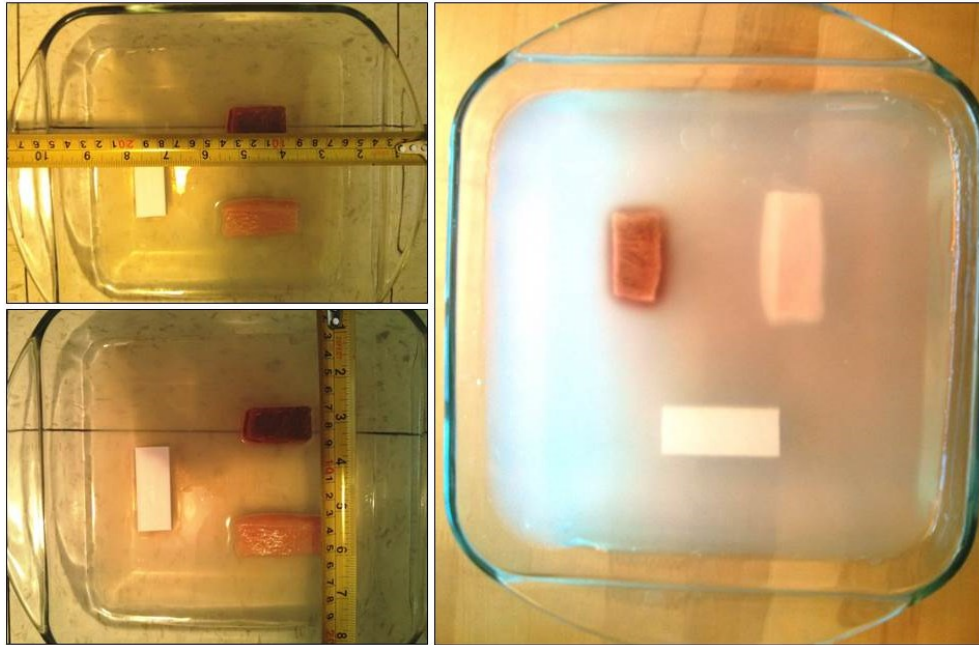


Figure 4.7 Test Phantom Containing Pieces of Beef and Chicken Meat and A Piece of Rubber Mounted in Jelly

All phantoms and also the human thigh were scanned by the ultrasound probe in the elevational direction while the motion of the probe was being recorded by the PATRIOT sensor (Human in vivo experiment is shown in Figure 4.8). The ultrasound images were obtained by the frame grabbing card at a frame rate of 60 Hz. The position and orientation of the probe were also recorded by electromagnetic sensor at the same frame rate, simultaneously. All B-scan images and position readings data were then acquired for each phantom and also for the human real tissue. Firstly some initial data processing routine are performed on the data to make them ready for being processed in order to achieve the final goal of sensorless out-of-plane motion estimation. The primary data processing routines are described in the following sections while the main data processing themes and algorithms are provided by detail in Chapter 5.

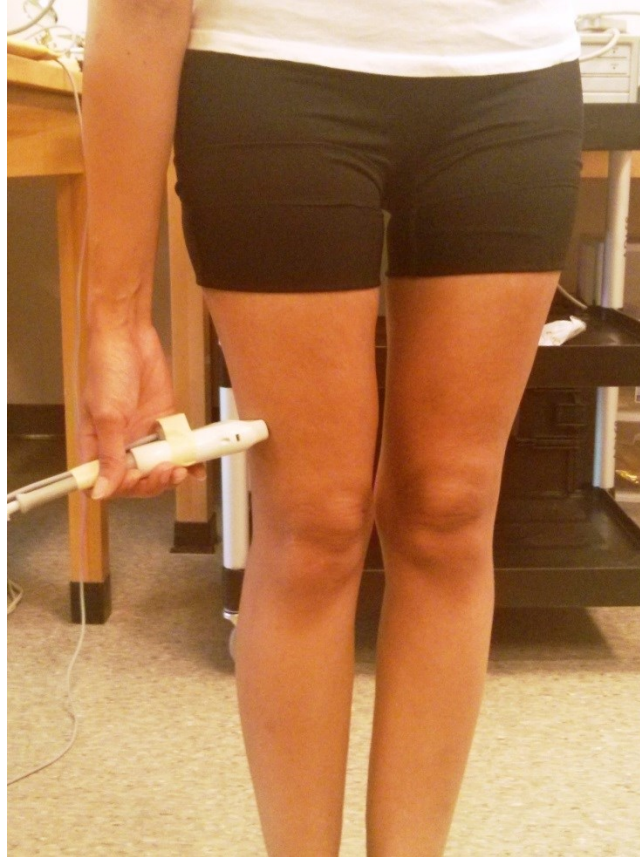


Figure 4.8 In-vivo Scanning of Human Thigh Tissue in Elevational Direction

4.2.3 Ultrasound Machine and Probe Specification

For all experiments in this thesis, a medical ultrasound imaging system (Picus, ESAOTE Europe, Maastricht, Netherlands) in companion with an Asus digital signal processing computer running Windows XP was used. The B-mode output of the ultrasound machine was connected to another computer running Windows 7 the display was on the second computer which was connected to a frame grabbing card to obtain frames directly from the output of the computer; this provided real-time image acquisition with long duration recording. The software that was used to view the data in ultrasound machine computer was ART.LAB [68]. The Picus ultrasound machine and the other computer used to display the data and grab the frames are shown in Figure 4.9.



Figure 4.9 Picus Ultrasound Imaging Machine Accompanied by Computer Connected to Frame Grabbing Card

A linear ultrasound probe was also used in the experiments (Model: L10-5 40 mm). The probe is shown in Figure 4.10. This probe consists of 127 individual piezoelectric crystal transducers with separation distance of $315 \mu\text{m}$. The thickness of this transducers layer is $188 \mu\text{m}$. The probe also contains two impedance matching layers which are embedded to remove unwanted waves and gradually match the impedance in order to optimize the ultrasound waves' transmission. These two matching layers have the thickness of $65 \mu\text{m}$ and $85 \mu\text{m}$ and the ultrasound propagation velocity of 2290 m/s and 2750 m/s , respectively. There is also a fourth layer in the ultrasound probe casing. This layer consists of an acoustic lens which plays the role of ultrasound waves focusing in the medium. The thickness and the propagation velocity of the acoustic lens layer are $1010 \mu\text{m}$ and 975 m/s , respectively [69].



Figure 4.10 L10-5 40 mm Linear Ultrasound Probe

The ultrasound wave frequency is in the range of 2.7-12.5 MHz for this machine and the frequency of 5 MHz was used in the experiments of this thesis. The system acquires samples from received waves every $0.03 \mu\text{s}$. For this specific system, a B-mode frame contains 127 scan lines each produced by one of the 127 transducers of the linear array [69] [70]. The frame observation rate, or simply frame rate, depends on the imaging modality that the system is operating on and is not related to the data storage process. In fact, the frame rate is determined by the repetition rate of a signal produced by a single specific transducer. This concept is called line of sight. The lateral and axial coverage of the frame is different for each imaging modality. The overall lateral coverage is 39.69 mm for B-mode obtained from 127 scan lines with separation distance of $315 \mu\text{m}$ between lines. The axial coverage or the image depth of up to 35 mm is achievable in B-mode. The values provided here are not absolutely correct and can be different for different ultrasonic propagation velocities through different materials being scanned. The received ultrasound signals are sampled with an analog to digital converter (ADC) that has 16 bits including a 4 bit offset. This results in a 12 bit recorded RF signal with a dynamic range of 72 dB [69].

4.2.4 Electromagnetic Sensor Specification

Electromagnetic sensors are good options to be used in calibration of decorrelation curves for sensorless freehand 3D ultrasound applications because they provide a compromise between accuracy and cost. The electromagnetic sensor used in the

experiments of this research is PATRIOT, Polhemus [71]. PATRIOT is a 6 DOF tracking system that computes both the position and orientation of the small sensor as it moves through space. It is also able to measure position and orientation in real-time. The PATRIOT system includes a system electronics unit, a power supply, one sensor, and one source (see Figure 4.11). The system electronics unit contains the hardware and software necessary to generate and sense the magnetic fields, and compute position and orientation. The source is the system's reference frame for sensor measurements. The weight of the system source can be in the range of 250-726 gr. The sensor is a lightweight small cube (9.1 gr). The sensor's position and orientation is precisely measured [72].



Figure 4.11 PATRIOT System; Electronics Unit, Sensor and Source [72]

The static accuracy of the system is 1.524 mm RMS (Root Mean Square) for the X, Y, or Z position and 0.40° RMS for sensor orientation. This specified performance is provided by the system in a non-metallic environment when the sensors are within a diameter of about 75 cm from the standard source. Operations at greater ranges will result in slightly degraded performance (see Figure 4.12). The latency of the system is less than 18.5ms, and the sampling (or update) rate is equal to 60 Hz for each sensor. The system provides multiple output formats including position in Cartesian coordinates (centimeters) and orientation in direction cosines, Euler angles or quaternions. The system runs Polhemus PiMgr GUI software which provides output data in 6 columns; the first three columns determine position of the sensor in X, Y, and Z directions, and the other three ones determine orientation of the sensor by reporting Azimuth, Elevation, and Roll angles [73].

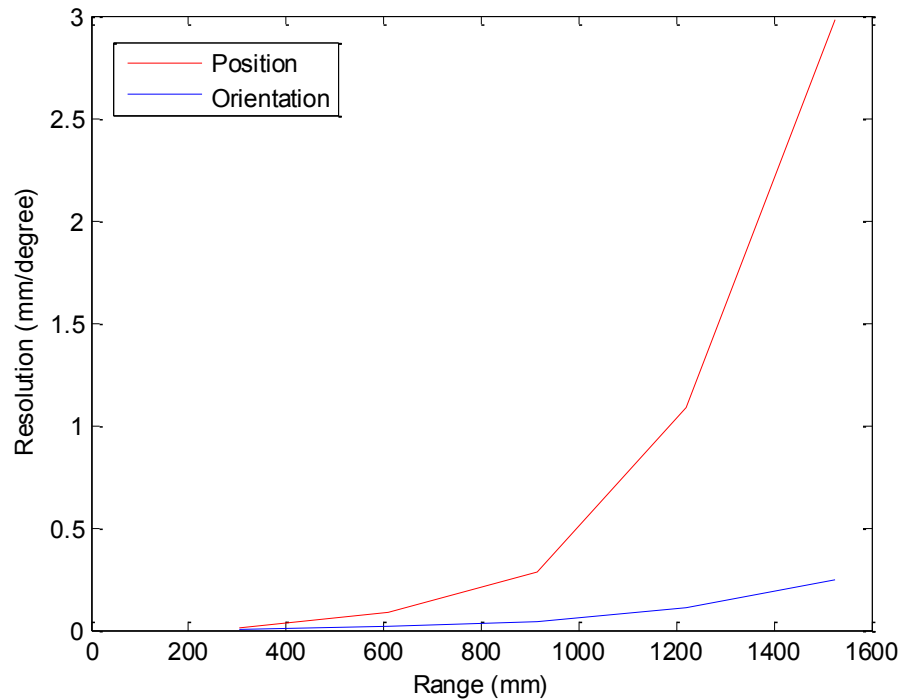


Figure 4.12 Range vs. Resolution Curve of PATRIOT Tracking System (Reconstructed from [72]).

4.3 Primary Data Processing

Since the frame grabbing card takes the image of the whole display screen, therefore the ultrasound frames acquired by the frame grabbing card include areas larger than only the B-mode images. As a result, it is required to first crop out the unwanted areas from all acquired frames. This was performed by using OpenCV Library resulting in B-scan images of size 395×400 pixels (3.95×4 cm) as shown in Figure 4.13. Cropping the B-mode images from the original large images was the first processing step performed successfully on all data. Two other essential steps required to be done before proceeding to main data analysis are temporal calibration and spatial calibration which are described by detail in the following sections.

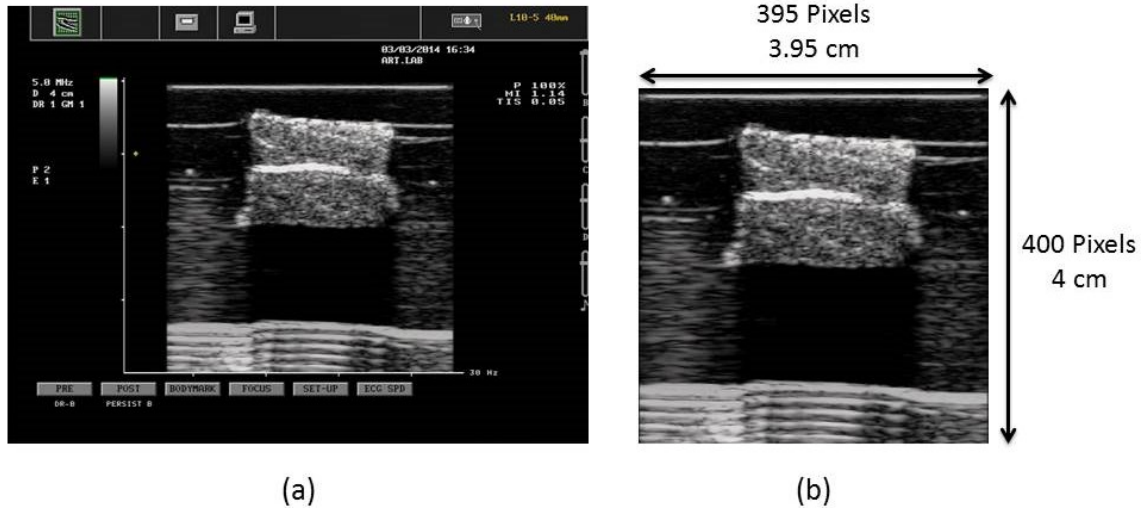


Figure 4.13 (a) Original Image of Ultrasound Machine Screen Acquired by Frame Grabbing Card While Scanning Beef Phantom. (b) B-scan Image of Beef Phantom After Cropping Unwanted Regions

4.3.1 Temporal Calibration

It was mentioned briefly before that the temporal calibration process is about matching ultrasound images with their true corresponding position readings. It deals with the estimation of ultrasound machine latency, as well as position sensing device latency, and finally calculates the difference between them. This difference is then required to be added to one stream to adjust time-stamps of position readings stream and images stream so they can be meaningfully matched together.

The approach used in experiments of this thesis to perform the temporal calibration is adapted from the one proposed by Cambridge group for using their Stradx freehand 3D system [34] and is implemented in MATLAB R2014a. It is said in this approach that for performing temporal calibration, a step input is required to be applied to both the image and position streams simultaneously. Practically speaking, we can produce step changes in both the image content and position readings by first holding the probe still against the skin for few seconds and then suddenly jerking it away. Then we have to look for the sudden changes in the images content and position readings. Finally any difference in the timings of these observed disturbances in two streams can be used to adjust the offset added to the position sensor timestamps.

To determine the step input in position readings stream, we monitor the motion of the probe looking at the amount it has translated between successive position readings (the orientation angles are ignored in this step). As it was said the probe should be held steady for 2-3 seconds at the beginning of the experiment. In this context, “holding the probe steady” means that it should not move by more than 1 mm between successive position readings. We jerk the probe suddenly causing sudden jumps in position readings (see Figure 4.14 and Figure 4.15). The step input is assumed to be taken place mid-way between the two position readings which first differed by more than 1 mm. The plots of position readings data in 2D and 3D and also the amount of translation between successive position readings are shown for the beef phantom experiment in Figure 4.14-16. The position reading that is determined as the beginning of the step input is flagged in all above mentioned plots.

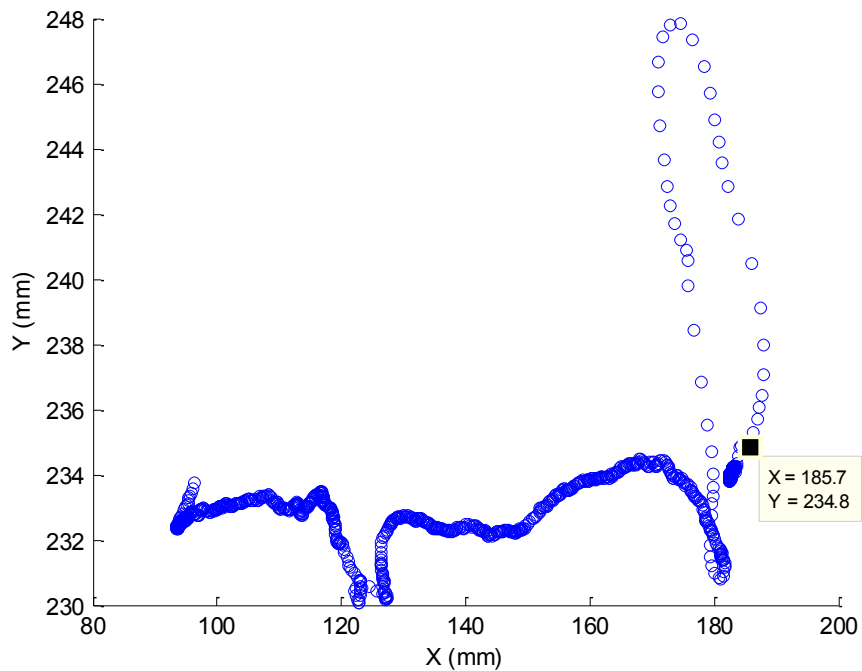


Figure 4.14 Plot of Position Readings Data Recorded for Beef Phantom Experiment in Two Dimensions (X and Y in mm)

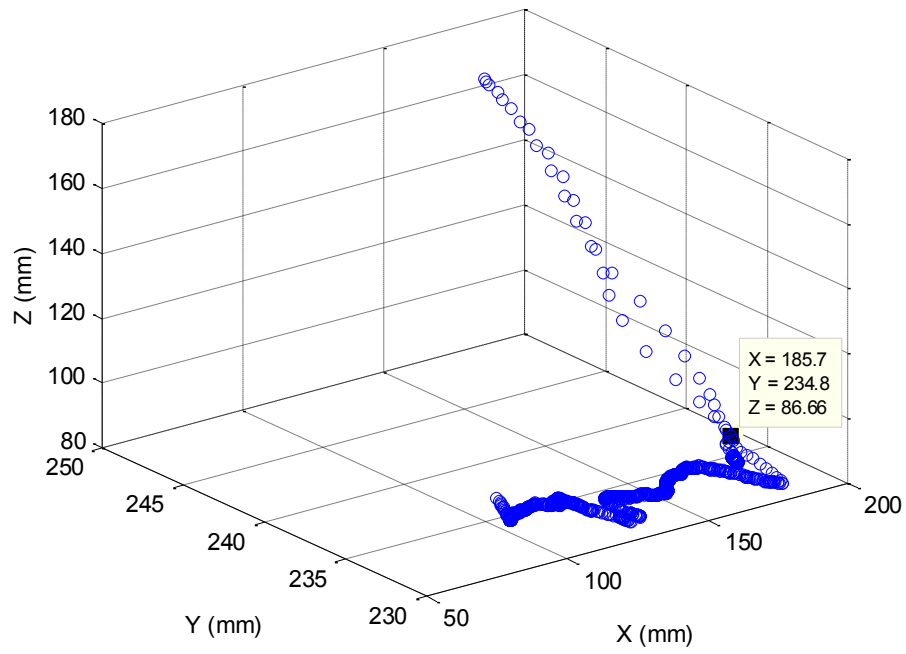


Figure 4.15 Plot of Position Readings Data Recorded for Beef Phantom Experiment in Three Dimensions (X, Y and Z in mm)

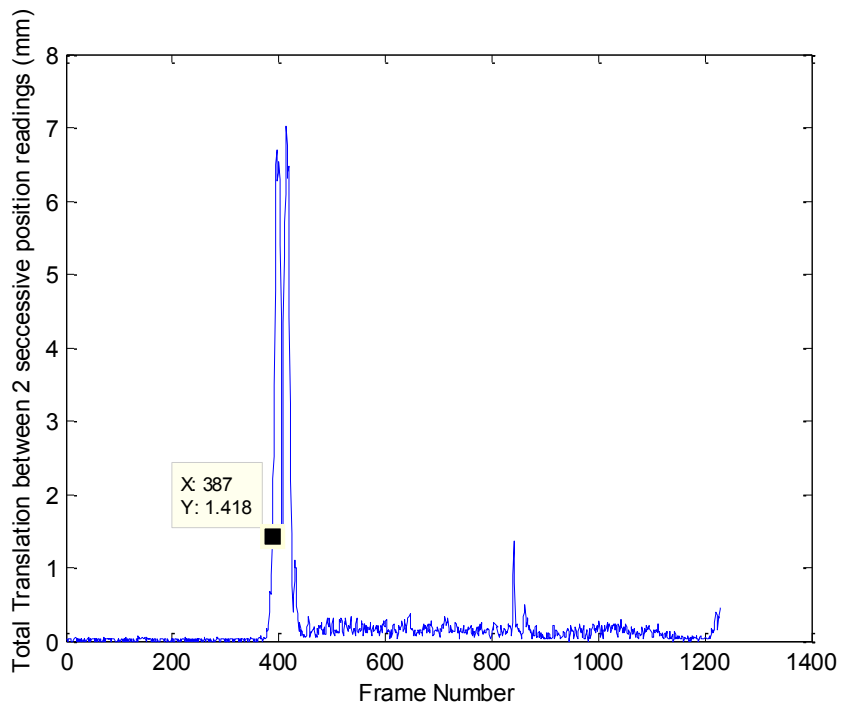


Figure 4.16 Total Translations between Successive Position Readings in mm for Beef Phantom Experiment

To determine the step input in ultrasound image stream, we need to compare successive images and measure the difference between them. To achieve this goal a particular type of measurement Δ_{im} is defined to calculate the difference between two images. It sums the pixel intensity values along ten rows and columns (these rows and columns are arranged in such a way that the space between them is equal) passing over the whole image. These sums are then subtracted from their values in the previous frame, and the absolute values are accumulated to provide a measure of difference between two successive images. To provide a better understanding, the Δ_{im} calculation procedure is visualized in Figure 4.17.

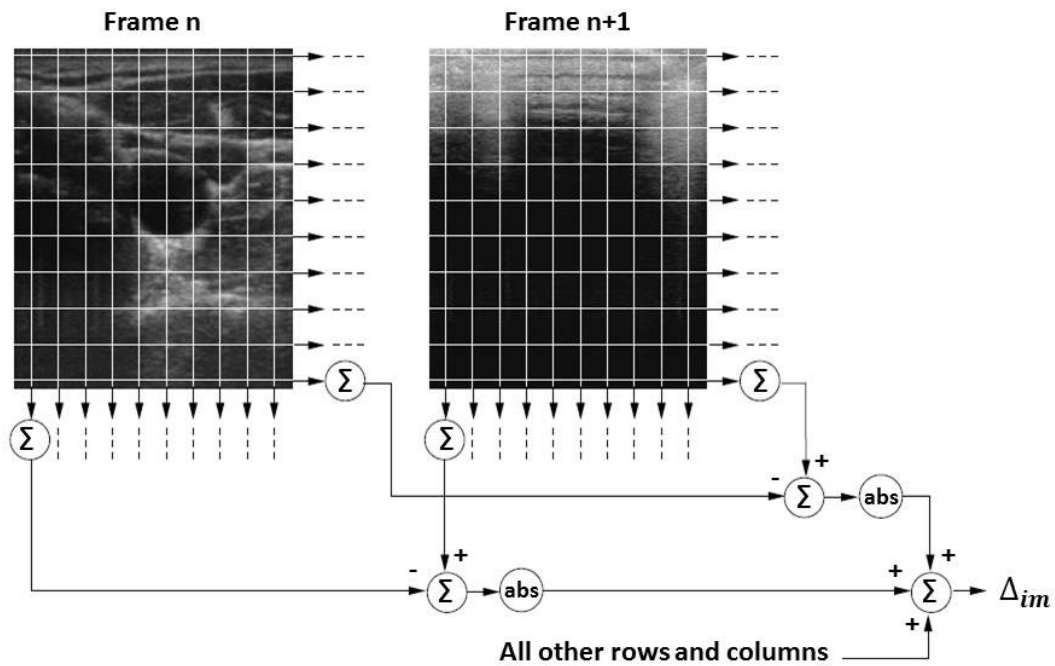


Figure 4.17 Measuring Difference between Successive B-scan Frames for Detecting Sudden Changes in Image Content [34]

To find the frame that represents the beginning of step input in the image stream, we calculate the Δ_{im} for all images during the period in which the probe was hold steady (approximately the first 2-3 seconds of the experiment) and find the maximum value between this calculated Δ_{im} s. this value is called maximum steady-state value Δ_{im} . Then we start calculating Δ_{im} for other remaining frames looking for the first Δ_{im} that exceeds the maximum steady-state value by 10%. The algorithm stops immediately after finding the first value of Δ_{im} that satisfies this condition and the step input is considered to occur

mid-way between the two images that produced this increased Δ_{im} . A schematic view of determining step input occurrence in image stream and position stream is shown in Figure 4.18.

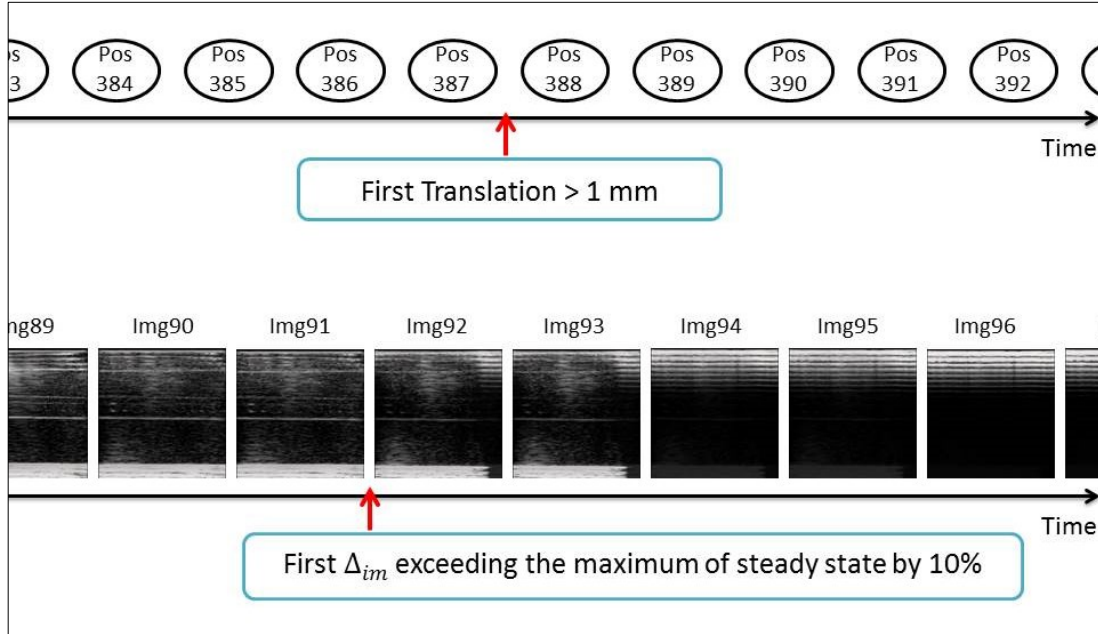


Figure 4.18 Deduction of Step Input Occurrence Time in Position and Image Streams

Now that we have the exact time, in both position and image stream, at which the step input has taken place, therefore it is possible to adjust the timing of the two streams. This adjustment results in images and position readings to have comparable time stamps. Given the position and image stream with the same time stamping, the exact position of each image frame can be calculated by interpolating the position readings just before and just after the image. This scenario applies only when the images and the position readings are acquired with a different frame rate and the time interval between two successive images is different from the time interval between two successive position readings. In this case we need a sampling window to find the position readings that the particular image is lying between them and interpolate between them to find the exact position of each image as shown in Figure 4.19a. In our experiments, since the position readings and the images were obtained with the same frame rate (both equal to 60 Hz), there is no need for interpolation. In fact, in this case, after the timing adjustment of two streams, simply the most recent image can be labeled with the most recent position reading as shown in Figure 4.19b.

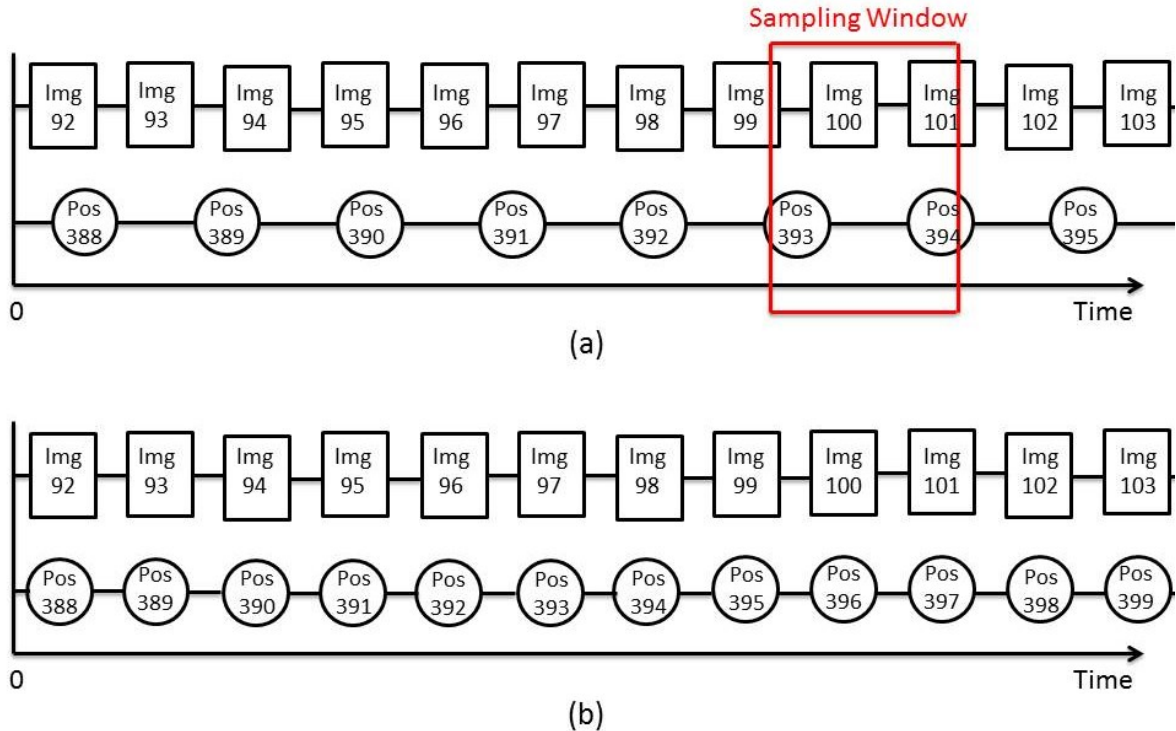


Figure 4.19 Matching Images and Positions. (a) In case of different frame rates, each image lies between two specific position readings and it is possible to find its positions accurately by linear interpolation between those two position readings. (b) In case of the same frame rates, the most recent image can be simply labeled with the most recent position reading.

4.3.2 Spatial Calibration

After we are done with the temporal calibration and the images are precisely matched with their corresponding positions and orientations, it is turn to perform the spatial calibration in order to determine the exact position of each image pixel in 3D space. It was discussed before that position sensing device indicates the 3D location of the small sensor attached to the ultrasound probe while we need the location of scan plane or each pixel of image in 3D space. The spatial calibration process is in fact the process of estimating the six-DOF rigid-body transformation matrix between the position sensor coordinate system and image plane coordinate system. A brief summary of spatial calibration process and how it works was provided before in Section 3.2.2.

It was discussed in the summary that there are four different coordinate systems involved in the spatial calibration process: the world coordinate system or the coordinate system of reconstruction volume indicated by C , the coordinate system of position sensing

device (the electromagnetic transmitter) indicated by T, the coordinate system of the sensor mounted on the probe (the electromagnetic receiver) indicated by R, and finally the coordinate system of the image plane indicated by P. The arrangement of these coordinate systems in the experiments of this thesis is displayed in Figure 4.20. In order to determine the location of every pixel in 3D space, it has to be transformed first from coordinate system of the image plane P to the coordinate system of the receiver R, second to the transmitter T, and last, to the reconstruction volume C. The overall calibration equation which multiplies all mentioned transformation matrices in order to convert each pixel's location in the image plane to its location in 3D space is provided in Equation 4.6.

$$\begin{pmatrix} x \\ y \\ z \\ 1 \end{pmatrix} = T_{C \leftarrow T} T_{T \leftarrow R} T_{R \leftarrow P} \begin{pmatrix} S_x u \\ S_y v \\ 0 \\ 1 \end{pmatrix} \quad (4.6)$$

In this equation, $T_{I \leftarrow J}$ shows the transformation from the coordinate system J to coordinate system I . u and v are the column and row indices of the pixel in the image, and S_x and S_y are scale factors with units of mm/pixel.

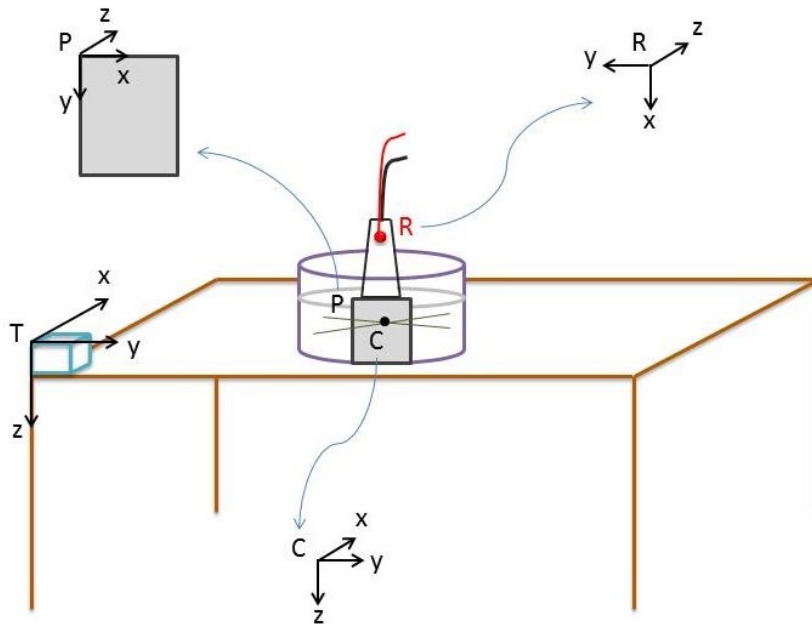


Figure 4.20 Arrangement of Coordinate Systems Involved in Spatial Calibration Experiment

The calibration process is usually performed by scanning a phantom with known geometric dimensions. One of the most common calibration phantoms that is able to accurately and precisely calibrate the freehand 3D system, is cross-wire phantom [74] [75]. In this type of phantom, two intersecting wires are mounted in jelly, with the electromagnetic transmitter located at some fixed location with respect to the wires. The cross-wire phantom prepared for the experiments of this thesis and a typical B-scan image acquired from scanning this phantom are shown in Figure 4.21.

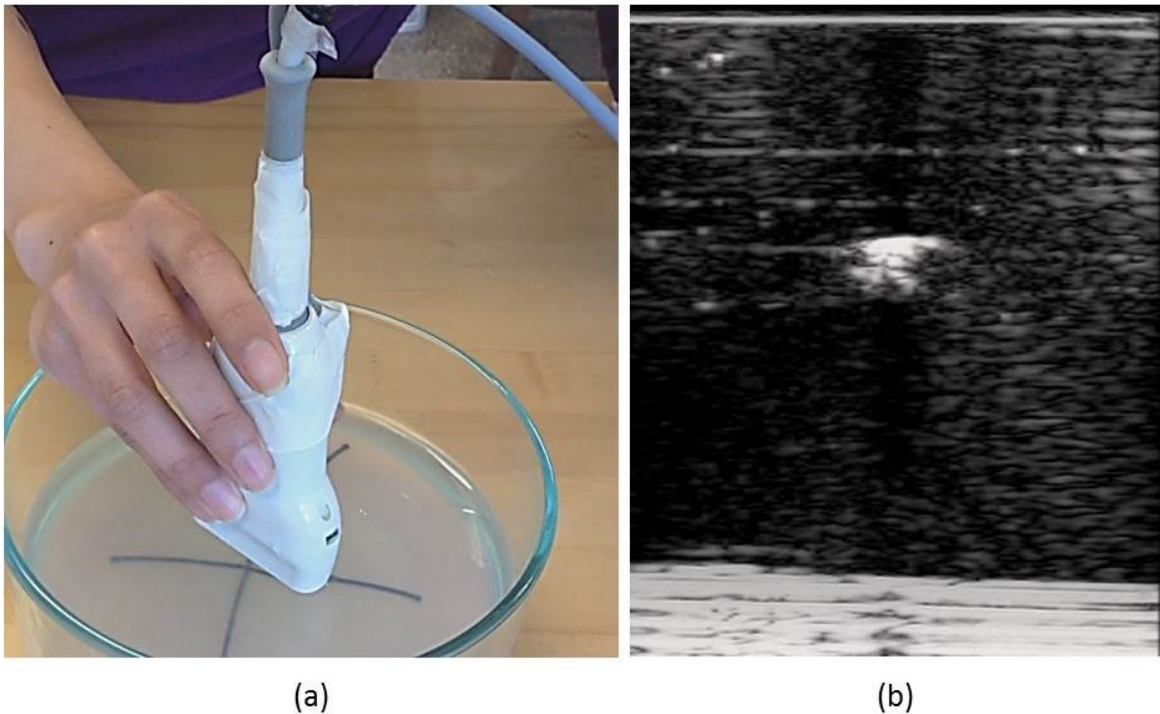


Figure 4.21 (a) Scanning Cross-Wire Phantom Containing Two Crossing Nylon Wires of 1mm Diameter Mounted in Agar Jelly (b) Typical B-scan of Cross-Wire Calibration Phantom with Cross of Two Wires Obviously Detectable (Area of Approximately $2 \times 1 \text{ mm}^2$)

In case of using cross-wire phantom, to simplify the calibration equations, the origin of C (reconstruction volume) is not assumed to be located at the corner of the reconstruction volume (as shown before in Figure 3.3) but it is assumed to be at the intersection of the wires instead. In the experiment, the location where the wires cross is scanned repeatedly from different directions by the ultrasound probe, resulting in B-scans each showing a detectable cross (as shown in Figure 4.21b). Considering Equation 4.6 and the assumption

of reconstruction volume' origin to be located at the intersection of the wires, the pixels at the center of the cross should satisfy Equation 4.7.

$$\begin{pmatrix} 0 \\ 0 \\ 0 \\ 1 \end{pmatrix} = T_{C \leftarrow T} T_{T \leftarrow R} T_{R \leftarrow P} \begin{pmatrix} S_x u \\ S_y v \\ 0 \\ 1 \end{pmatrix} \quad (4.7)$$

The first three rows of the equation give three equations involving the measurements; $T_{T \leftarrow R}$, u and v , S_x and S_y , with the unknowns; $T_{C \leftarrow T}$ and $T_{R \leftarrow P}$. $T_{T \leftarrow R}$ can be calculated for each image frame having the position and orientation readings acquired from the electromagnetic position sensing device. A transformation between two 3-D coordinate systems has six degrees of freedom: three rotations (α , β , γ) and three translations (x , y , z). There are many ways to parameterize a rotation between two 3-D coordinate systems, including unit quaternions, rotation matrices and a variety of three-angle systems. The electromagnetic sensor used in our experiments (PATRIOT, Polhemus) adopts a Z-Y-X Euler angles scheme to report the orientation of the sensor.

The Euler angles reported by PATRIOT sensor are called azimuth, elevation and roll and are indicated by α , β , and γ , respectively. These angles represent an azimuth-primary sequence of frame rotations that define the current orientation of the sensor with respect to its zero-orientation state. The defining rotation sequence is an azimuth rotation followed by an elevation rotation followed by a roll rotation. The Euler angle coordinates that are output of PATRIOT as a measure of sensor orientation are displayed in Figure 4.22. In this figure, the x , y , z 3D coordinate system represents the sensor frame in its current orientation state and the X , Y , Z 3D coordinate system represents the reference frame against which the relative orientation of the sensor frame is measured. The azimuth angle α is defined as a rotation of the X and Y reference axes about the Z reference axis (the transition axes labeled X' and Y' represent the orientation of the X and Y axes after the azimuth rotation). The elevation angle β is defined as a rotation of the Z reference axis and the X' transition axis about the Y' transition axis (the transition axis labeled Z' represents the orientation of the Z reference axis after the elevation rotation). The current x -axis of the current sensor frame represents the orientation of the X' transition axis after the elevation rotation. Lastly, the roll angle γ is defined as a rotation of the Y' and Z' transition axes about the x -axis of the sensor frame. The y and z -axes of the current sensor frame represent the orientation of the Y' and Z' transition axes after the roll rotation.

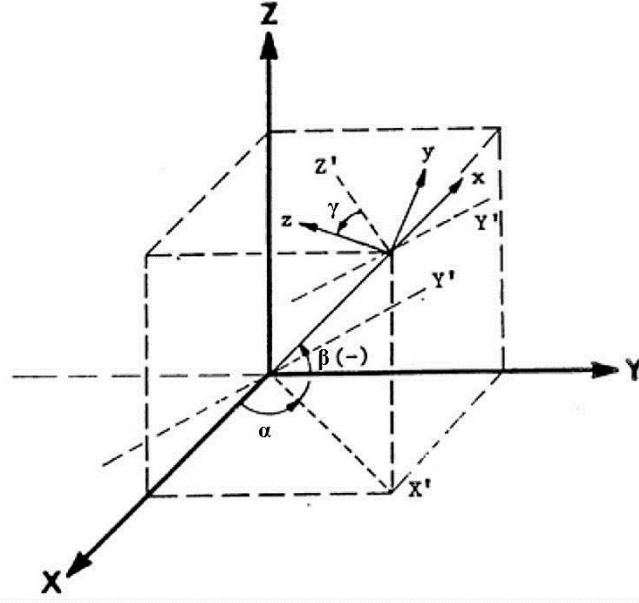


Figure 4.22 Z-Y-X Euler Angles Reported by PATRIOT Sensor as A Measure of Sensor's Orientation [76]

Using Z-X-Y Euler angles approach, the homogeneous matrix describing the transformation takes the form shown in Equation 4.8 [77].

$$T_{J \leftarrow I} = \begin{pmatrix} \cos \alpha \cos \beta & \cos \alpha \sin \beta \sin \gamma - \sin \alpha \cos \gamma & \cos \alpha \sin \beta \cos \gamma + \sin \alpha \sin \gamma & x \\ \sin \alpha \cos \beta & \sin \alpha \sin \beta \sin \gamma + \cos \alpha \cos \gamma & \sin \alpha \sin \beta \cos \gamma - \cos \alpha \sin \gamma & y \\ -\sin \beta & \cos \beta \sin \gamma & \cos \beta \cos \gamma & z \\ 0 & 0 & 0 & 1 \end{pmatrix} \quad (4.8)$$

In Equation 4.7, u and v are the column and row indices of the pixel at the center of the cross. The common way to determine u and v , considering the quality of ultrasound images, is to manually locate the center point pixel in each B-scan. It makes the calibration process time-consuming but in the context of our work (sensorless probe motion estimation) it is better to choose the method which gives accurate results even if it is time-consuming. Because we need to do the calibration process only once and after that the FDS decorrelation curves are calibrated for the speckle phantom we don't need it anymore. S_x and S_y are scale factors with units of mm/pixel. Given the 4 cm axial depth of the B-scans and the image size of 400×395 pixels, it is simply computable that $S_y = \frac{40}{400} = 0.1$ mm/pixel and considering the square shape of each pixel S_x is similarly equal to 0.1. If

m B-scans are available in the image sequence, then the Equation 4.7 can create a system of nonlinear homogeneous equations as shown in Equation 4.9.

$$0 = f(\theta, \phi) \quad (4.9)$$

In the above equation, θ shows the measurements and ϕ represents the unknowns. Having a pre-determined set of equations (the number of equations must be greater than the number of unknowns), the system can be solved using several iterative methods such as the robust Levenberg–Marquardt algorithm which is used in this thesis.

For calibration, we are only interested in $T_{R \leftarrow P}$, but we must also solve for $T_{C \leftarrow T}$, even though we will subsequently discard these values and adopt an arbitrary, convenient $T_{C \leftarrow T}$ for reconstruction, as explained in the previous section. Therefore, it may appear that ϕ must be a 12-element vector, composed of the six parameters of $T_{R \leftarrow P}$ and the six parameters of $T_{C \leftarrow T}$. However, it is clear from inspection of the geometry that the coordinate system C can be at any orientation and still satisfy Equation 4.7. This means that the three orientation angles of $T_{C \leftarrow T}$ are not identifiable. These angles are therefore removed from ϕ , and for convenience set to zero in Equation 4.9 which means that the reconstruction volume coordinate system C and the transmitter coordinate system T will have the same orientation as shown before in Figure 4.20.

When applying Levenberg–Marquardt algorithm, we assigned particular initial values to the elements of ϕ vector. After a number of iterations, when the elements of ϕ vector are converged to one value and $\Delta\phi$ is sufficiently small for successive iterations, the algorithm will stop and the converged value of ϕ is considered as the answer of the equations system. It needs to be mentioned that a system of nonlinear equations can have multiple solutions and to find the answer we are looking for, the initial values assigned to unknowns have an important role. In fact, in iterative methods, the point that we start our calculations from can affect the answer that the system converge to. In this thesis, we had a rough estimation of the value of unknowns from experimental setup so the initial values were selected based on this rough estimation. By putting the resulted values of ϕ vector in Equation 4.6, we can calculate the 3D location of pixel at the center of the cross to see how close they are to the origin of C (the point with X, Y, and Z values all equal to zero). Distribution of the

calculated values for X, Y, and Z for all B-scan frames displaying the detectable cross are shown in Figure 4.23 to 4.25.

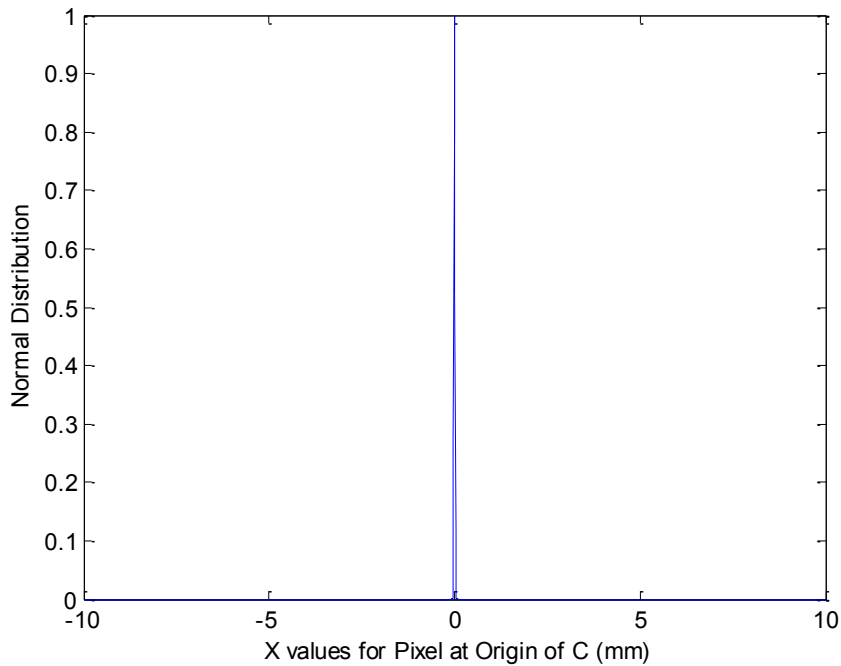


Figure 4.23 Normal Distribution of Estimated X Values for Pixel at Origin of C for All B-scans Representing Image of Wires Crossing (Mean = -0.0025 mm, Variance = 0.0107 mm²).

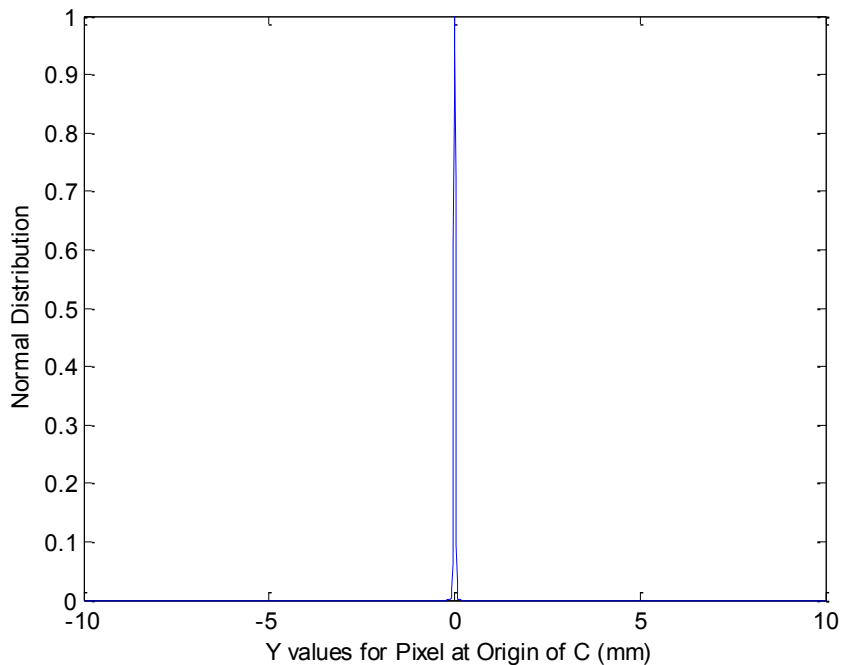


Figure 4.24 Distribution of Estimated Y Values for Pixel at Origin of C for All B-scans Representing Image of Wires Crossing (Mean = 0.0021 mm, Variance = 0.0221 mm²).

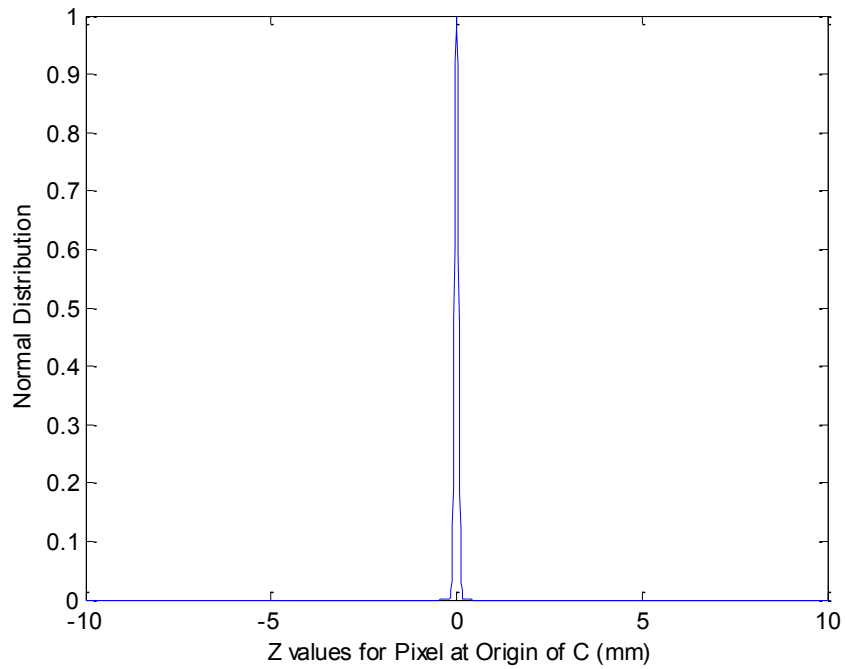


Figure 4.25 Distribution of Estimated Z Values for Pixel at Origin of C for All B-scans Representing Image of Wires Crossing (Mean = -0.00005 mm, Variance = 0.0491 mm²).

Chapter 5

Data Processing and Results

According to the primary data processing routines described in Chapter 4, we have to deal with two kinds of data in this chapter. The position data from the electromagnetic sensor and the B-scan images acquired from ultrasound probe and machine. It was discussed in previous chapter that how the raw position and image data were processed in order to obtain the 3D location of each pixel in the images. In this chapter the main data processing scheme will be completely covered which is about using B-scan images of speckle phantom (which are labeled with the position and orientation) to estimate the out of plane motion between B-scan frames of different test phantoms and also B-scans of real human tissue experiment. All algorithms used in this chapter are implemented on MATLAB R2014a.

5.1 Data Samples Selection

For the purpose of sensorless out-of-plane motion estimation using speckle decorrelation method we need to divide B-scan images into smaller patches because ultrasound resolution cell's width is not equal all over the image and it varies across and

down the B-scans. Therefore it is required to calibrate decorrelation curves for small patches all over the image. There are different approaches for dividing ultrasound images into patches, for example in some studies with the aim of detecting FDS regions in images, moving patches or overlapping patches are defined and used [52]. Since the effect of both FDS and non-FDS regions is considered in the proposed method of this thesis, there is no need for overlapping patches and each frame is simply divided into an 8 column x 12 row grid of patches. The patches located in the two first rows and four last rows of the grid were considered as noisy patches and were disregarded in the data processing procedure because they contained strong specular features. The grid used to divide images to patches and the valid patches which are used for the out-of-plane motion estimation task are shown Figure 5.1.

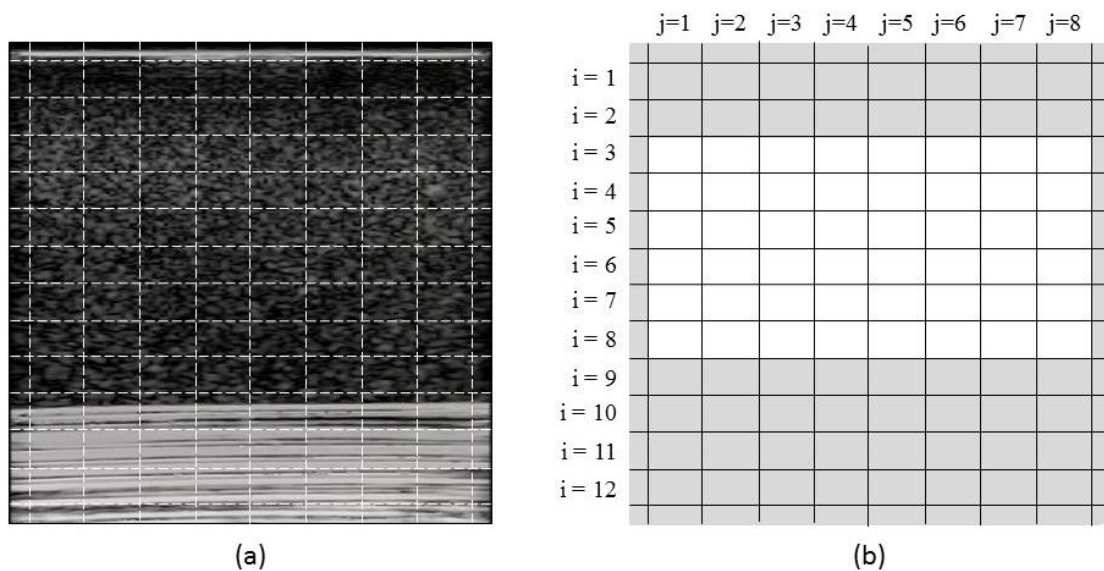


Figure 5.1 (a) Grid of Patches Applied on B-scan Image of Speckle Phantom (b) Grid of Patches with Valid Patches Shown in White and Invalid Patches (Disregarded Due to Noise) Shown in Gray

In order to find each patch' location in 3D space we consider the pixel at the center of the patch. Therefore in our algorithm the 3D location of the pixel at the center of each patch is calculated for every image using the position readings data from sensor, results of spatial calibration process, and Equation 4.6. It gives us a matrix of x, y, and z values of the central pixels of patches for all frames. The distances between patches for all possible pairs of images in the image sequence is calculated then. This distance is calculated in

three elevational, axial, and lateral directions which are corresponding to z, y, and x directions, respectively. For each patch in every frame we look up in 30 next frames and only consider the frames which are separated by an elevational distance equal to 0.1, 0.2, 0.3, 0.4, 0.5, 0.6, 0.7, or 0.8 mm. The experiments show that the data decorrelate in the elevational direction over a distance not greater than 0.8mm, that is why we do not consider any other distances greater than 0.8 mm. Among all the selected frames, 100 frames are randomly selected for each particular elevational distance. Therefore each point in decorrelation curves can be represented with 100 samples. These finally selected frames make up our database for implementation of speckle decorrelation method.

5.2 FDS Decorrelation Curves Calibration

In order to generate and calibrate decorrelation curves of speckle phantom, we need to calculate the correlation between patches with known elevational distance. An approximation of the speckle correlation function as a function of the elevational distance δ between two B-scans I_1 and I_2 using the Gaussian model function was given in Equation 4.5. In practice, this approximation works well when the RF signal provided by the ultrasound imaging device are directly used and the gray level intensity of the image is defined on a linear scale. Unfortunately, as it was discussed before, the RF signal is not generally available on most standard ultrasound systems in clinical environments. In such standard ultrasound systems, the RF intensity data are compressed on a logarithmic scale and the output is B-mode images with pixels' intensity values ranged from 0 to 255. Since we deal with B-mode images in this thesis and it is one of the advantages of our work, it is required to first convert the intensity values back to a linear scale by applying the relation from Smith and Fenster work [78] given in Equation 5.1.

$$I(i, j) = 10^{\frac{P(i, j)}{L}} \quad (5.1)$$

In Equation 5.1, $I(i, j)$ represents the decompressed gray level intensity of the pixel located at i th row and j th column of the image, $P(i, j)$ is the measured intensity in the B-mode image, and L is the linearization factor which converts the 0 to 255 log scale of the original data to a linear scale (0 to 72 dB range). This range is selected because the

recorded RF signal by the Picus ultrasound machine used in the experiments of this thesis has a dynamic range of 72 dB.

The decorrelation curves are usually obtained by capturing a set of B-scan images at known distances along the elevation direction and measuring the normalized correlation coefficients. The formulation for the normalized correlation coefficients $\rho(d)$ is given by Equation 5.2 [79].

$$\rho(d) = \frac{\sum_{i=1}^m \sum_{j=1}^n (I_0(i, j) - \bar{I}_0)(I_d(i, j) - \bar{I}_d)}{\sqrt{\sum_{i=1}^m \sum_{j=1}^n (I_0(i, j) - \bar{I}_0)^2 \sum_{i=1}^m \sum_{j=1}^n (I_d(i, j) - \bar{I}_d)^2}} \quad (5.2)$$

In the above equation, I_0, I_d stand for to the pixel intensity array of a particular patch of the B-scan image located at $d = 0$ and the pixel intensity array of the corresponding patch in the image located at distance d , respectively. Also, \bar{I}_0 and \bar{I}_d are the mean value intensity of the patches, and m and n are the height and width of the patches.

5.2.1 In-Plane Motion Compensation

Before proceeding to the decorrelation curves calibration step, it is necessary to remind that in our experiments we are dealing with a freehand system. It means that, unlike most studies on this topic in which the probe is mounted on a mechanical device allowing accurate translations only in elevational direction, motion of the probe in this thesis is totally unconstrained. The probe is moving by hand in an arbitrary manner and its motion is not limited in any directions. The main advantage of using this approach in experiments is that it is in complete agreement with the eventual goal of out-of-plane motion estimation task which is about engineering a sensorless freehand 3D ultrasound system. The problem with this approach is that the freehand motion does not produce pure elevational translations of the probe and in-plane motion and out-of-plane rotations are also included in the motion between successive frames. Disregarding the in-plane motion between frames will causes inaccuracies in the result. Therefore it is required to first compensate for in-plane motion and then proceed to speckle decorrelation method. Examples of such studies can be found in [11] [80]. In this thesis we adopt the idea in previous works to be applicable on B-mode images. Assuming that we are considering two B-scan frames A and

B and after dividing images into the patches, for each patch in frame A we introduce a range of potential offsets in axial and lateral directions for the corresponding patch in frame B. Then we move the patch in frame B within the possible offset ranges and calculate correlation coefficient between the patch in frame A and the shifted patch in frames B. Among all measured correlation coefficients we select the maximum value in order to create and calibrate elevational decorrelation curves (see Figure 5.2). Also, the axial and lateral offset of the patch in frame B that generates this maximum value is considered as the in-plane translation between these two frames. Applying this method on the data can improve the accuracy of out-of-plane motion estimation in the next step.

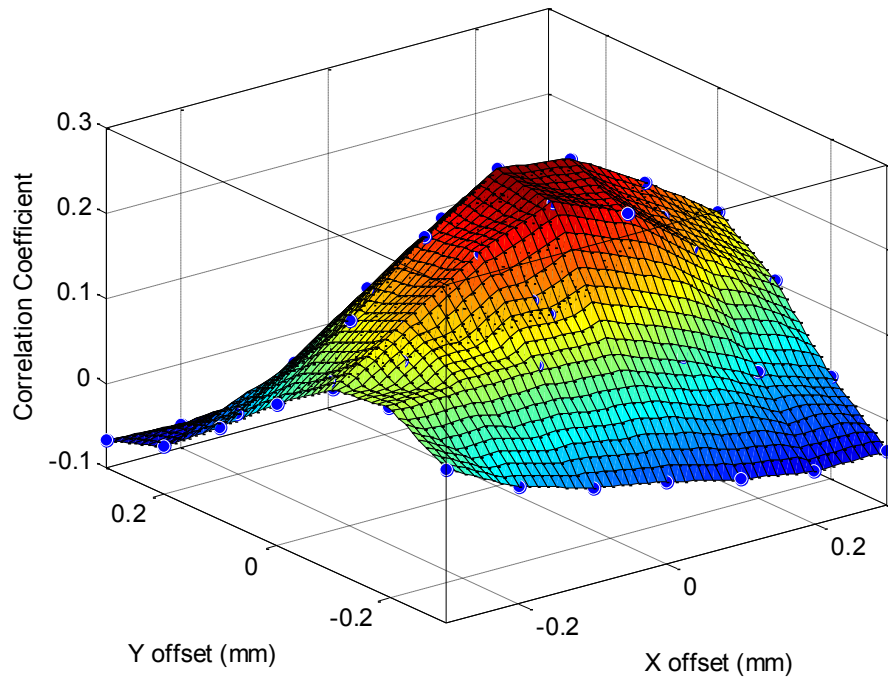


Figure 5.2 Surface Fitted on Measured Correlations between Particular Corresponding Patches of Two Frames for Different Amounts of In-Plane Offset between Them

5.2.2 Creating Decorrelation Curves

The correlation coefficient values are measured for several patches in the images. For each patch and for each specific elevational distance, all measured correlation coefficients are averaged to end up with only one data point. In fact, each data point on each curve is the average of a large number of observations (this number for the speckle phantom

decorrelation curves is equal to 100 in this thesis). After calculating all the required data points for a particular patch, it is possible to fit a curve into the data and create the decorrelation curve for that patch. The decorrelation curves can be simply created by applying linear interpolation method between successive data points. In this thesis it is done by using the MATLAB Curve Fitting ToolboxTM and by selecting the linear interpolation method in the toolbox. A number of these decorrelation curves obtained for the speckle phantom are shown in Figures 5.3, 5.4, and 5.5. The curves shown in Figure 5.3 are from the first column of the grid but at different depths. The curves displayed in Figure 5.4 are obtained for the patches from the same column near the center of the B-scan (column four), but at different rows. Similarly, the curves shown in Figure 5.5 are obtained for patches located at different depths of the same column (column eight) in the B-scan image. The decorrelation curves displayed in these figures can help us to interpret how the resolution cell width σ is not the same all over the B-scan image and varies depending on the lateral and axial position of the patch in the image. It can be seen in the figures that the widths of the curves shows great amount of variation in the resolution cell down the B-scan but there is little variation across the B-scan. In fact, different patches in the same row give similar curves but different patches in the same column show curves with different widths. Also it is obvious from the curves that the imperfect elevational focusing of ultrasound beam becomes much worse at the bottom of the scan in comparison to the top of the scan.

It was discussed before that in order to achieve the final goal of out-of-plane motion estimation it is required to calibrate decorrelation curves for the speckle phantom not only in elevational direction but also in lateral and axial directions. For moving the patches in the lateral and axial directions we do not need to have two different frames. In fact, we can calculate the axial and lateral decorrelation curves by only shifting the patches in the same frame and measuring the correlation coefficient between the shifted patch and the original one. Since in this thesis we are dealing with B-mode images rather than RF signal images, the amount of movement in axial and lateral directions is constrained to the dimensions of one pixel. The pixels of the B-scans here have a square shape of 0.1×0.1 mm therefore the finest possible offset that is achievable in axial and lateral directions is equal to 0.1 mm. However, we calculate axial and lateral correlation coefficients at offsets of 0, 0.1, 0.2, and

0.3 mm. The axial and lateral decorrelation curves acquired from speckle phantom B-scans for the patches located at column 1, column 4, and column 8 of the patches grid are shown respectively in Figures 5.6, 5.7, and 5.8.

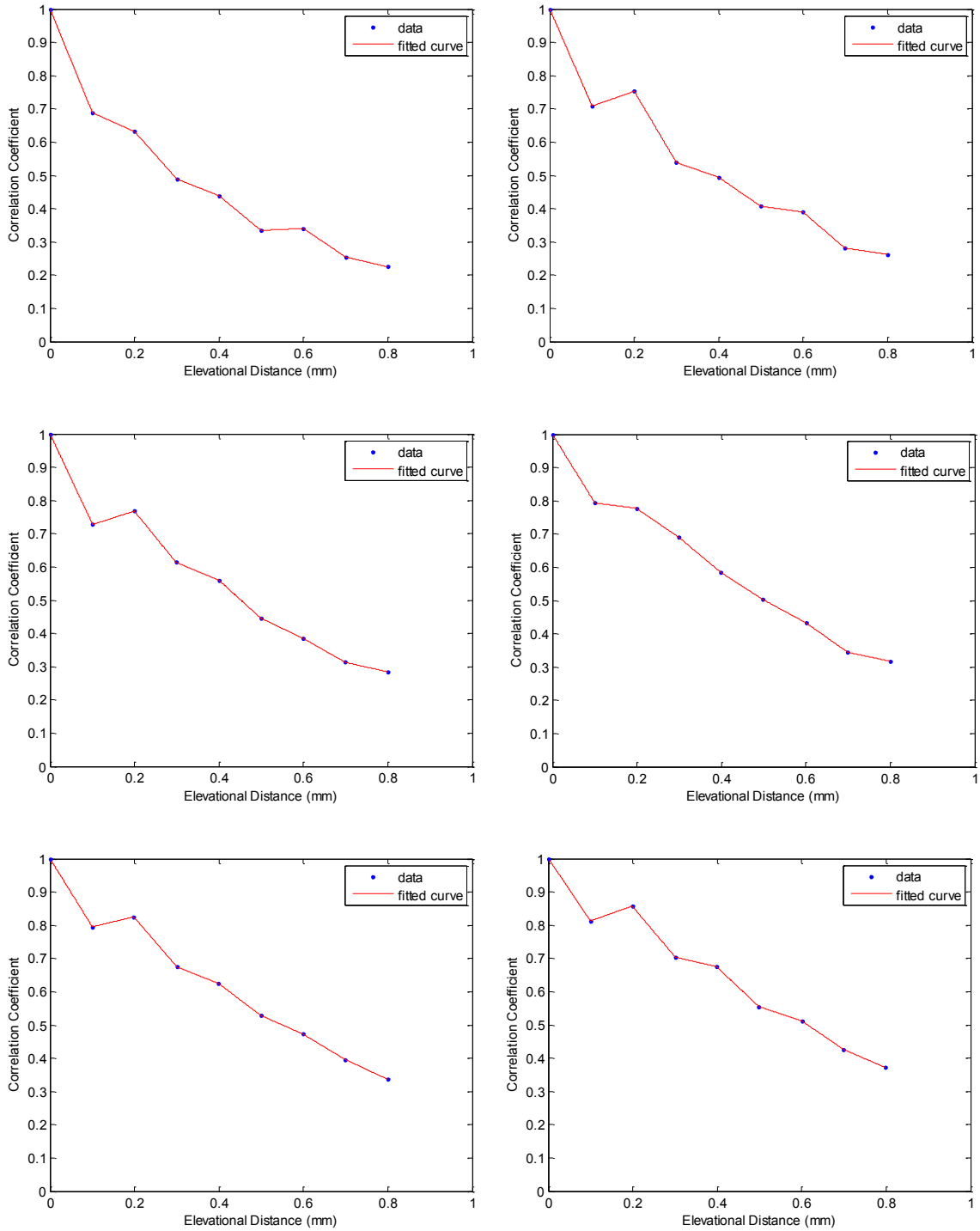


Figure 5.3 Elevational Decorrelation Curves of Speckle Phantom for Six Patches from Column 1 of Grid but at Different Rows (Top right is for the patch located at row 3, top left is for the patch located at row 4, middle right is for the patch located at row 5, middle left is for the patch located at row 6, bottom right is for the patch located at row 7, and bottom left is for the patch located at row 8).

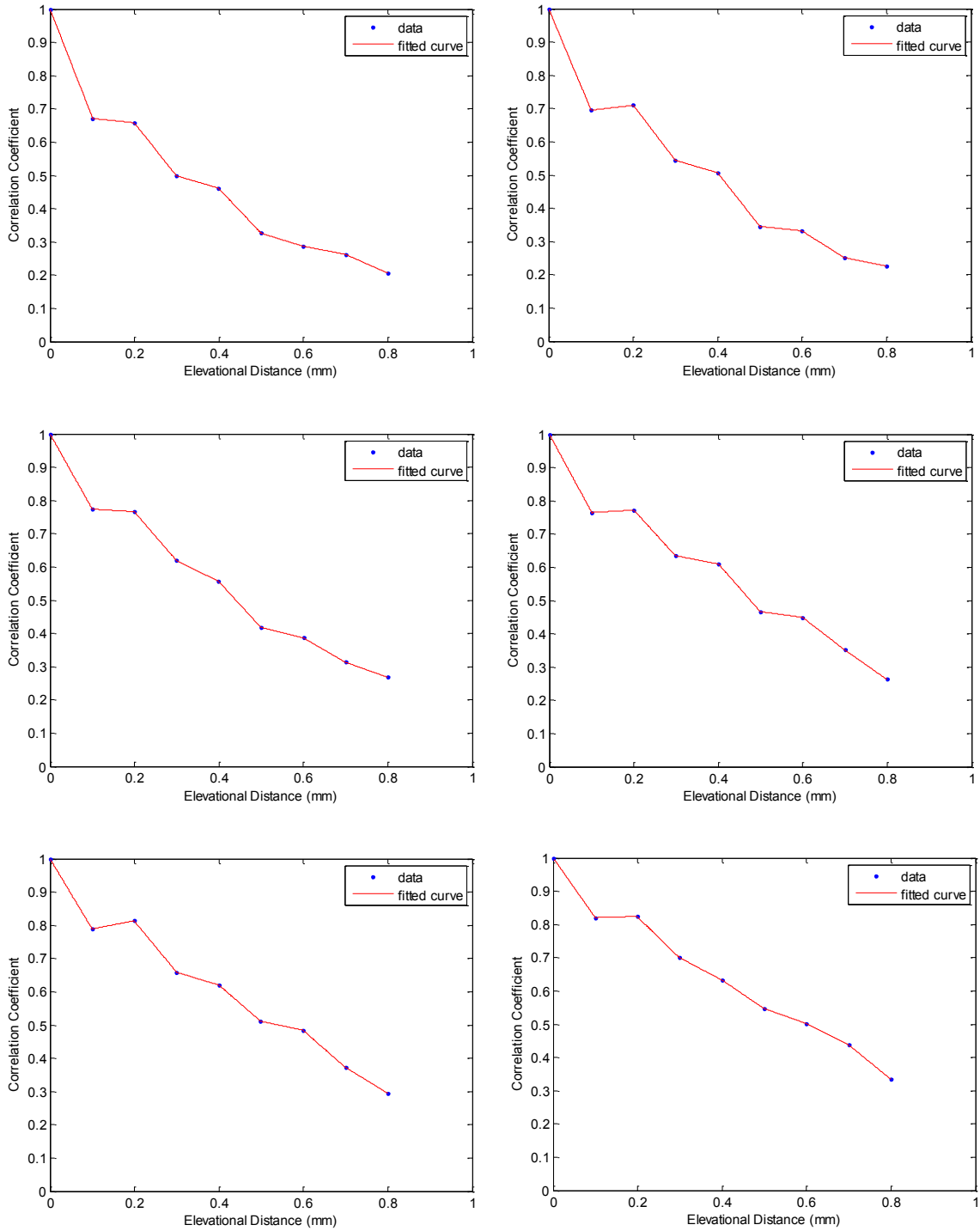


Figure 5.4 Elevational Decorrelation Curves of Speckle Phantom for Six Patches from Column 4 of Grid but at Different Rows (Top right is for the patch located at row 3, top left is for the patch located at row 4, middle right is for the patch located at row 5, middle left is for the patch located at row 6, bottom right is for the patch located at row 7, and bottom left is for the patch located at row 8).

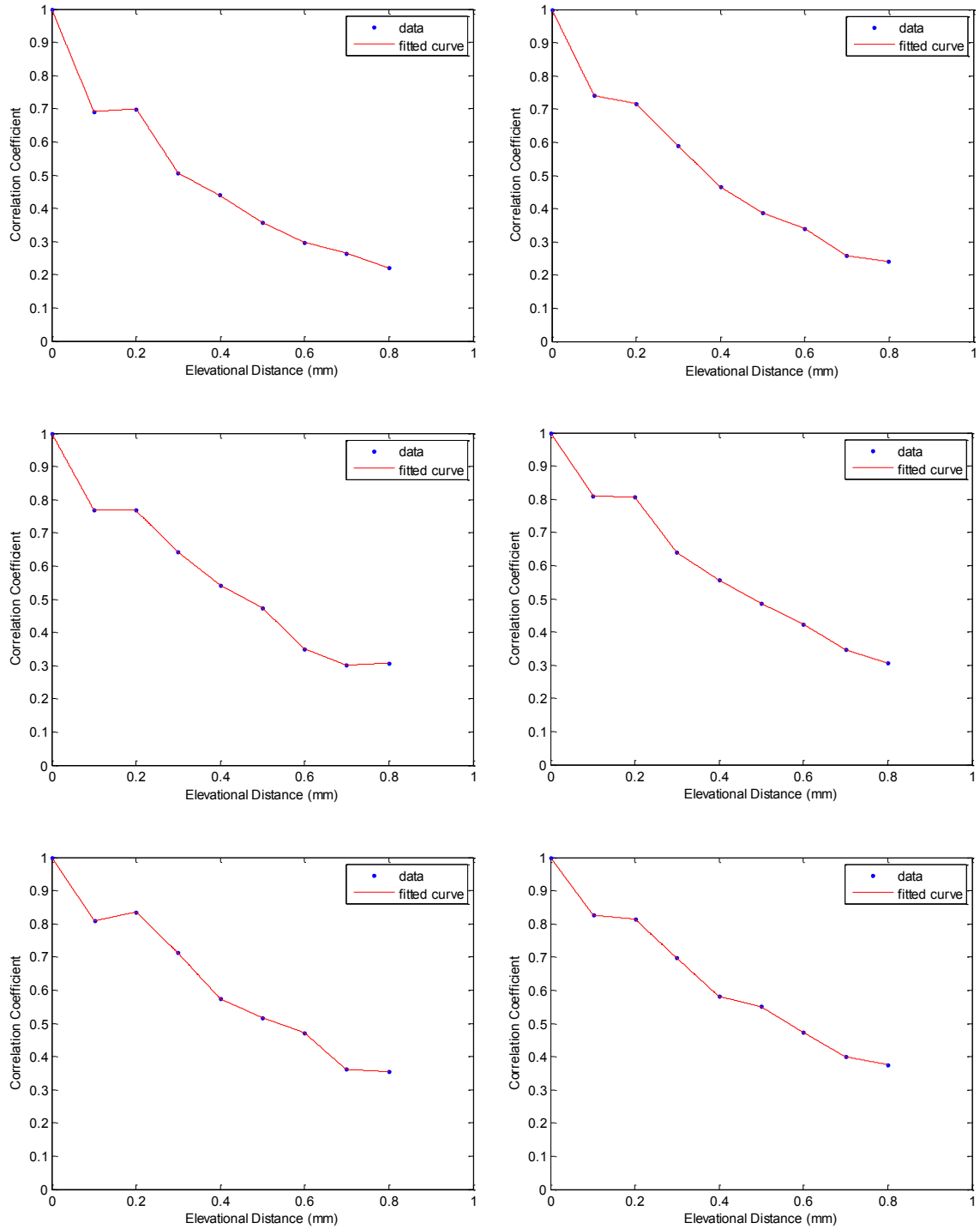


Figure 5.5 Elevational Decorrelation Curves of Speckle Phantom for Six Patches from Column 8 of Grid but at Different Rows (Top right is for the patch located at row 3, top left is for the patch located at row 4, middle right is for the patch located at row 5, middle left is for the patch located at row 6, bottom right is for the patch located at row 7, and bottom left is for the patch located at row 8).

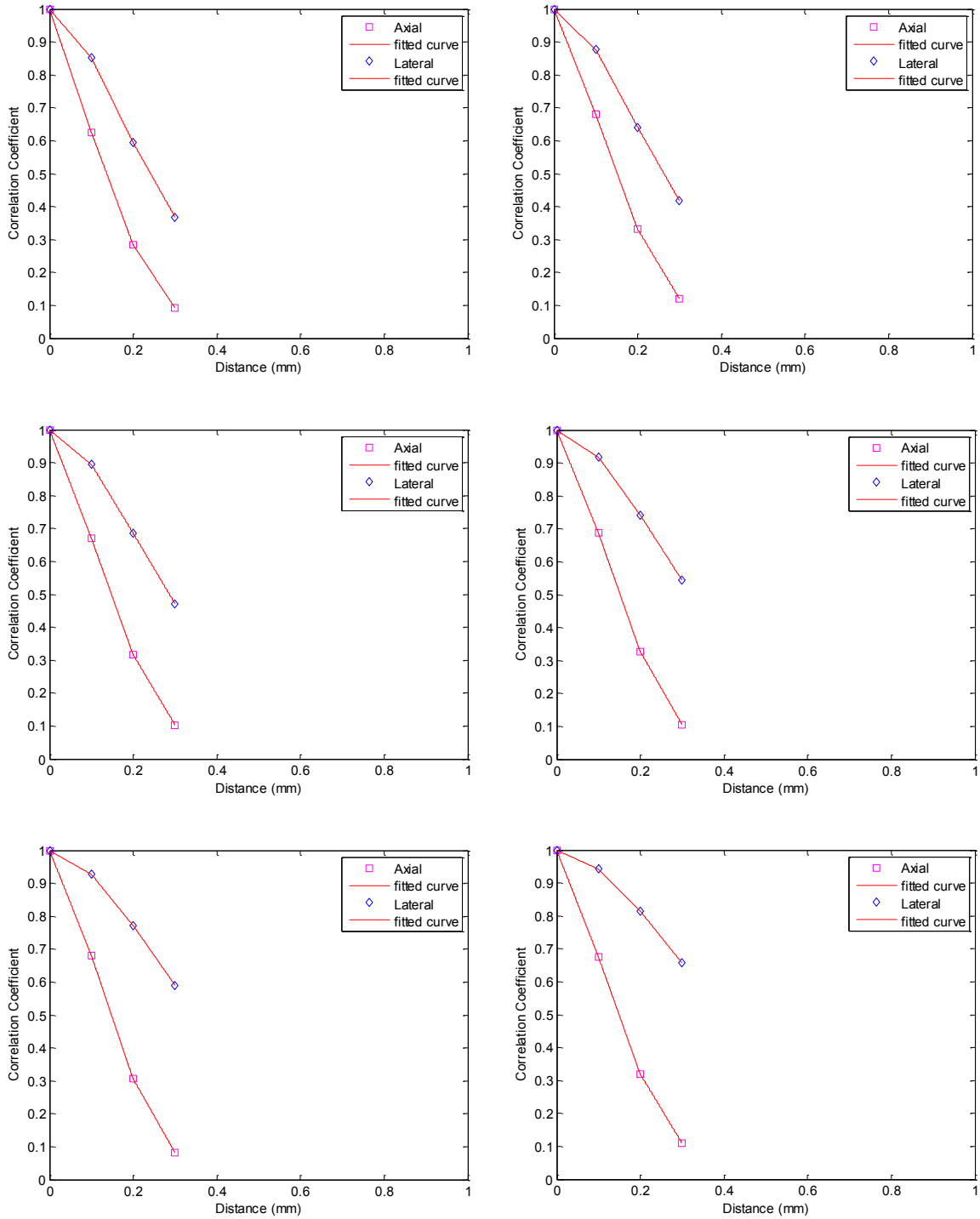


Figure 5.6 Axial and Lateral Decorrelation Curves of Speckle Phantom for Six Patches from Column 1 of Grid but at Different Rows (Top right is for the patch located at row 3, top left is for the patch located at row 4, middle right is for the patch located at row 5, middle left is for the patch located at row 6, bottom right is for the patch located at row 7, and bottom left is for the patch located at row 8).

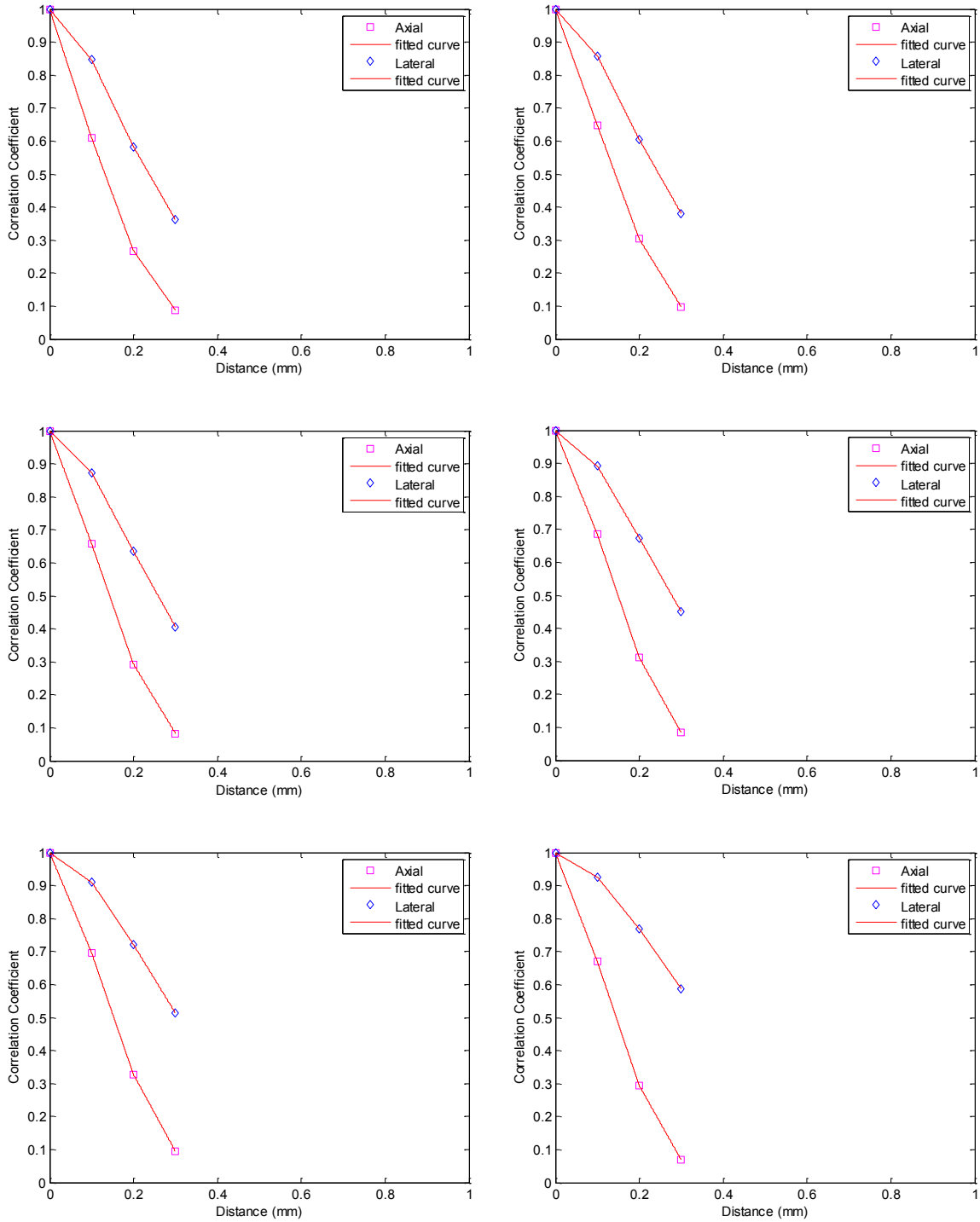


Figure 5.7 Axial and Lateral Decorrelation Curves of Speckle Phantom for Six Patches from Column 4 of Grid but at Different Rows (Top right is for the patch located at row 3, top left is for the patch located at row 4, middle right is for the patch located at row 5, middle left is for the patch located at row 6, bottom right is for the patch located at row 7, and bottom left is for the patch located at row 8).

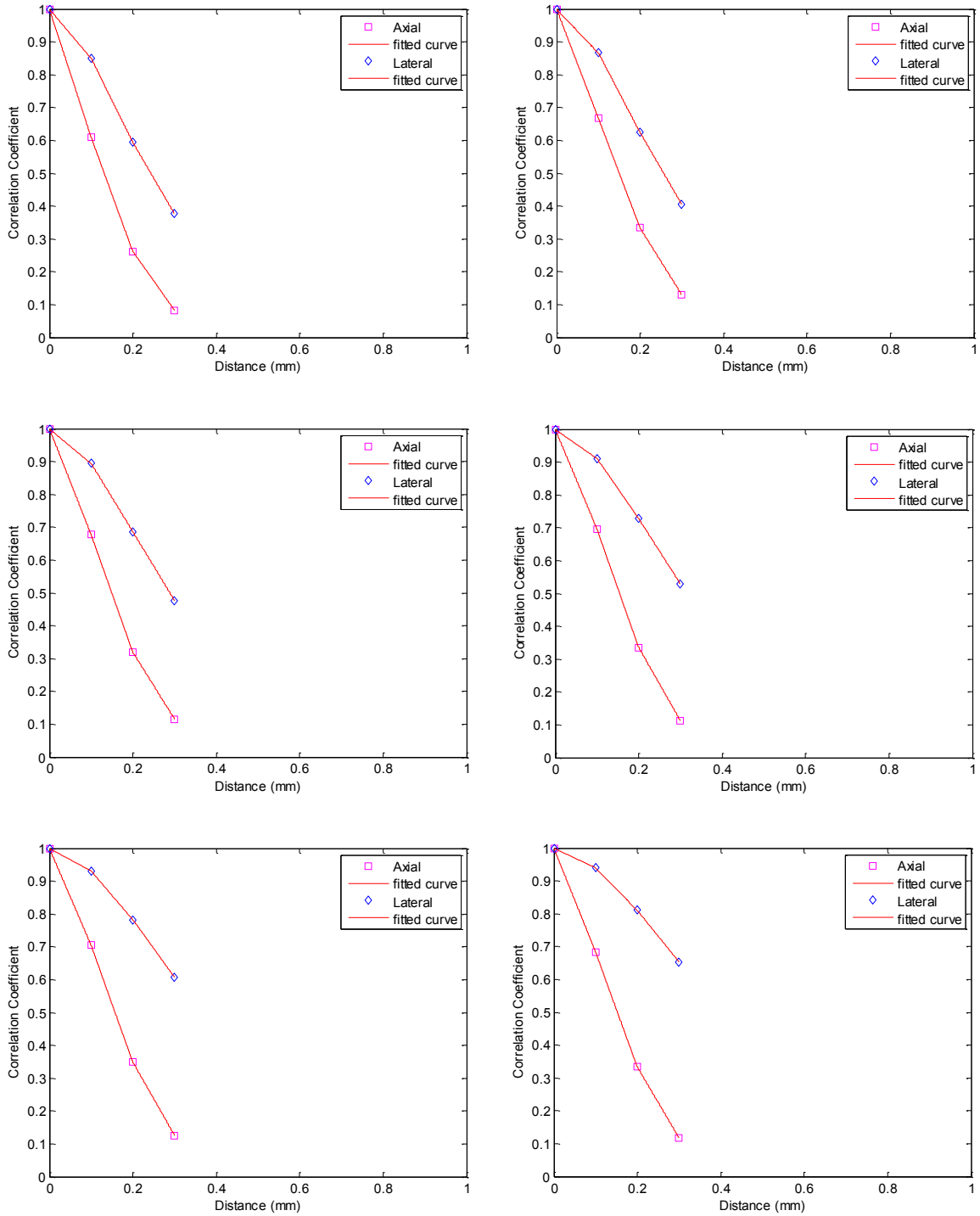


Figure 5.8 Axial and Lateral Decorrelation Curves of Speckle Phantom for Six Patches from Column 8 of Grid but at Different Rows (Top right is for the patch located at row 3, top left is for the patch located at row 4, middle right is for the patch located at row 5, middle left is for the patch located at row 6, bottom right is for the patch located at row 7, and bottom left is for the patch located at row 8).

5.3 FDS Decorrelation Curves Adjustment

The eventual purpose of this study is to use the calibrated decorrelation curves to estimate the elevational spacing between pairs of scans in the beef and chicken phantoms data sets and the human tissue data set. However, the ultrasound images of real tissue contain regions of coherent scattering and it has been shown in many studies that using the original FDS decorrelation curves in order to estimate elevational motion between frames indicates a significant amount of error. On the other hand, regions of Rayleigh scattering are quite rare in real tissue scans and if we try to detect these regions and apply the method only on these regions it will cause disregarding a great amount of information in the data set. In order to avoid these difficulties, the new approaches try to consider the effect of both Rayleigh scattering and coherent scattering in the images and it is not surprising that these recent approaches are more successful in this area. As it was discussed before, the method used in this thesis is an adaptation of Cambridge heuristic model [13] for RF ultrasound signals. In fact, this thesis tries to overcome the limitations of using B-mode ultrasound images and adjusts the model in such a way to make it applicable on B-mode ultrasound images. A detailed explanation of the Cambridge heuristic model and how data processing algorithms are implemented in this thesis is provided in the following.

Assume that we intend to estimate the elevational distance between two particular corresponding patches A and B respectively from B-scan frames i and j in a real tissue data set. If the patches contain only FDS regions, the correlation coefficient between them can be written as $\rho_r = \rho(A, B)$, where ρ_r stands for the correlation under Rayleigh scattering condition. Now if we add a component of coherent scattering to each patch as it is the case when dealing with images of real tissue, it will increase the correlation between patches. The new patches are modeled as $A + kB$ and $B + kA$ ($0 \ll k \ll 1$) and consequently the correlation coefficient between them will change to $\rho = \rho(A + kB, B + kA)$. The parameter k is used to measure the amount of correlation caused by coherent scattering over the distance between two patches. By expanding this recent expression for the correlation coefficient using Equation 4.4, it is possible to derive the relationship between ρ and ρ_r and consequently the formula to calculate parameter k as they are given in Equation 5.3 and 5.4, respectively.

$$\rho = \frac{(1 + k^2)\rho_r + 2k}{(1 + k^2) + 2k\rho_r} \quad (5.3)$$

$$k = \frac{(1 - \rho\rho_r)}{(\rho - \rho_r)} - \frac{\sqrt{(1 - \rho^2)(1 - \rho_r^2)}}{(\rho - \rho_r)} \quad (5.4)$$

Having these equations, we first calculate axial and lateral decorrelation curves for the patch A. if the patch A shows an axial correlation ρ_a at axial shift of d_a , having the FDS axial decorrelation curves we know the expected correlation ρ_r , therefore we can use Equation 5.4 to calculate k_a that represents the amount of coherent scattering in patch A. we can repeat the same routine in the lateral direction and calculate k_l at lateral shift of d_l for the patch A. Under the assumption of physical isotropy of the coherent scatterers in the axial, lateral and elevational directions, we expect to have the equal amount of coherent scattering over an elevational distance d_e . Since the resolution of the ultrasound imaging systems in elevational direction is around four times worse than the resolution in axial direction, it is assumed that each amount of d_e is correspondence to $4d_a$ and $4d_l$. Since we are dealing with B-mode images in this thesis and we have a limitation that the finest possible displacement in axial and lateral directions is equal to 0.1 mm (height and width of one pixel), we calculate k_a and k_l for the set of displacements $\{0, 0.1, 0.2\}$ mm. Therefore it gives us a matching set of values k_e for elevational offsets $\{0, 0.4, 0.8\}$ mm. Then we simply average k_a and k_l as it is given in Equation 5.5 to obtain the final set of values for k_e .

$$k_e(4d) = 0.5(k_a(d) + k_l(d)) \quad (5.5)$$

Now we can calculate adapted elevational decorrelation curve for patch A which accounts for both Rayleigh scattering and coherent scattering using the relation given in Equation 5.3. As it was mentioned before, we are working with B-mode images and the amount of displacement in axial and lateral direction is constrained by the size of one pixel. Therefore we have only three correlation data points (corresponding to the elevational distances equal to 0, 0.4 mm, and 0.8 mm) to create the new adapted elevational

decorrelation curves. One approach around this problem is to simply create the adapted decorrelation curve using only these available data points as it is shown in Figure 5.9. The problem with this approach is that it totally disregards the shape of original FDS decorrelation curves which is an important factor in elevational motion estimation task. Therefore using this approach can cause a great amount of error and only the results of motion estimation around adapted points (0.4 mm and 0.8 mm) would be accurate. Another approach which we have used in this thesis is to shift other data points between 0 and 0.4 mm and also the data points between 0.4 mm and 0.8 mm based on the amount of shifts for 0.4 mm and 0.8 mm to preserve the shape of the original curve. Assuming that the difference between the FDS correlation and adapted correlation at elevational distance of 0.4 mm is equal to $D_{0.4}$, the amount of shift for the points corresponding to the set of elevational distances $\{0.1, 0.2, 0.3\}$ mm can be equal to $\{0.25D_{0.4}, 0.5D_{0.4}, 0.75D_{0.4}\}$. we can repeat this analysis for the point corresponding to elevational distance of 0.8 mm and shift the data points corresponding to the set of elevational distances $\{0.5, 0.6, 0.7\}$ by the set of amounts $\{0.25D_{0.8}, 0.5D_{0.8}, 0.75D_{0.8}\}$. The adapted curve which is created by using the second approach in this thesis is shown in Figure 5.10.

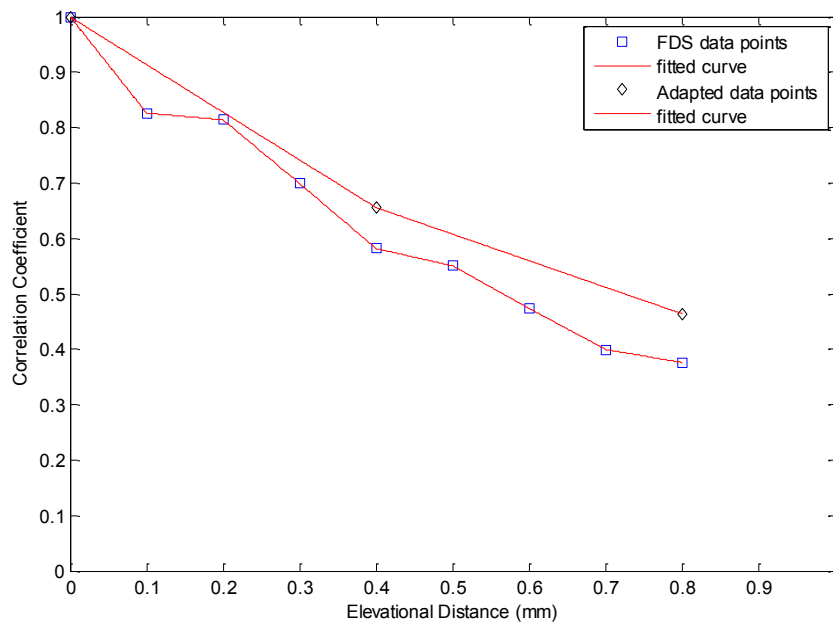


Figure 5.9 FDS Decorrelation Curve Adjustment Using Only Two Adapted Data Points Corresponding to Elevational Distances Equal to 0.4mm and 0.8mm

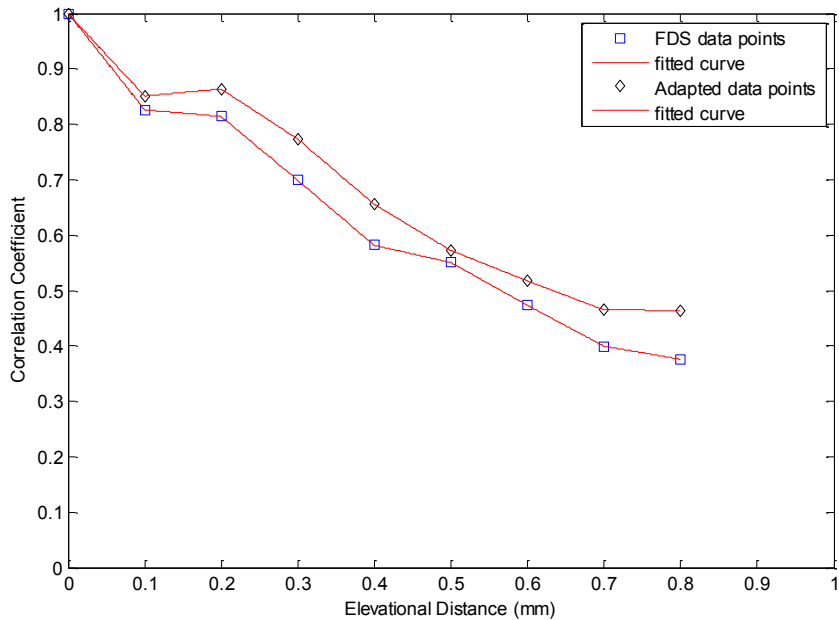


Figure 5.10 FDS Decorrelation Curve Adjustment by Adapting All Data Points Based on Amount of Displacement for Data Points Corresponding to Elevational Distances Equal to 0.4mm and 0.8mm

5.4 Method Evaluation

After sample frames of test phantoms and human thigh separated by elevational distances from the specific set of elevational distances $\{0.1, 0.2, 0.3, 0.4, 0.5, 0.6, 0.7, 0.8\}$ mm are selected using the approach described in Section 5.1 and the adapted elevational decorrelation curves are created and calibrated for each patch, we can use these curves to estimate the elevational distance between patches. In fact, by looking up a particular measured correlation coefficient between two corresponding patches of two frames in the decorrelation curve we can find the elevational distance between them. After performing the entire data processing steps on the data sets and estimate the separation distance between patches, the results from valid lookups were averaged to obtain a single distance estimate for each pair of scans.

This procedure is performed on B-scan images of beef test phantom, chicken test phantom, and human thigh and the estimated elevational distances using this method are compared to the measured elevational distances acquired from Patriot electromagnetic sensor. It is worth mentioning that in this study we consider the measured elevational

distances by Patriot electromagnetic sensor as gold standard and we assume that they are entirely accurate. Therefore, the amount of error in the results reported in this section is based on the deviations from Patriot sensor measurements which itself can have some amount of inaccuracy with respect to the true elevational distance between frames. It also needs to be noticed that in B-scans of beef and chicken data set, unlike the human thigh data set, only a partial region of the image is displaying the tissue. Therefore, we had to change the location and size of the patches grid for these two data sets before performing data analysis. However, for human thigh data set, in which the B-scans fully contain the image of the tissue, dividing images into patches is exactly similar to what was described and shown in Section 5.1. The grid of the patches used to divide the images of human thigh, beef and chicken data sets and their corresponding grid applied on images of speckle phantom are shown respectively in Figure 5.11, Figure 5.12, and Figure 5.13.

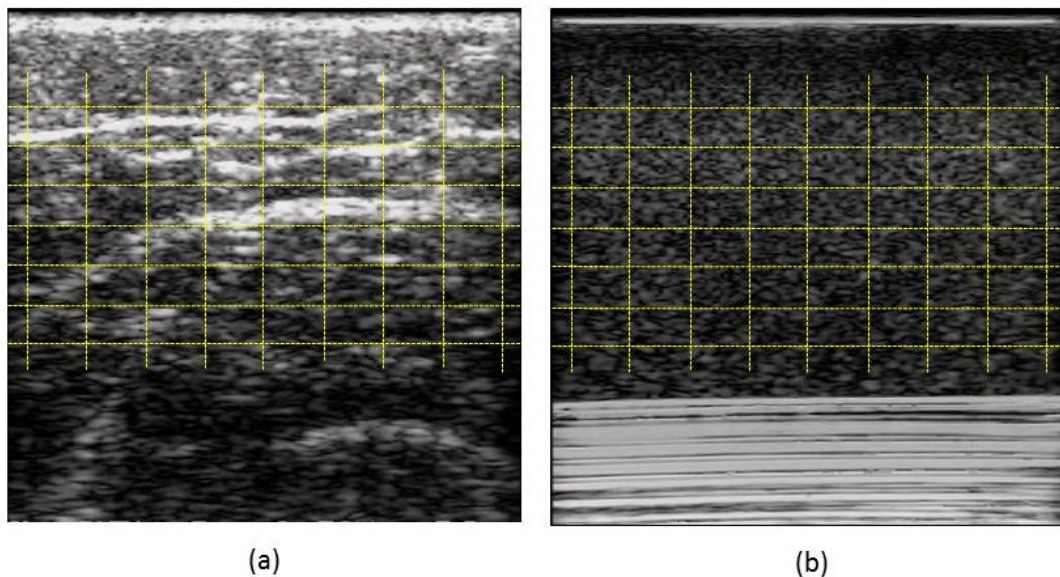


Figure 5.11 (a) Typical B-scan Image of Human In-vivo Data Set with 8×12 Grid Dividing Image into Patches (b) Typical B-scan Image of Speckle Phantom Data Set Divided into Patches by The Same Grid

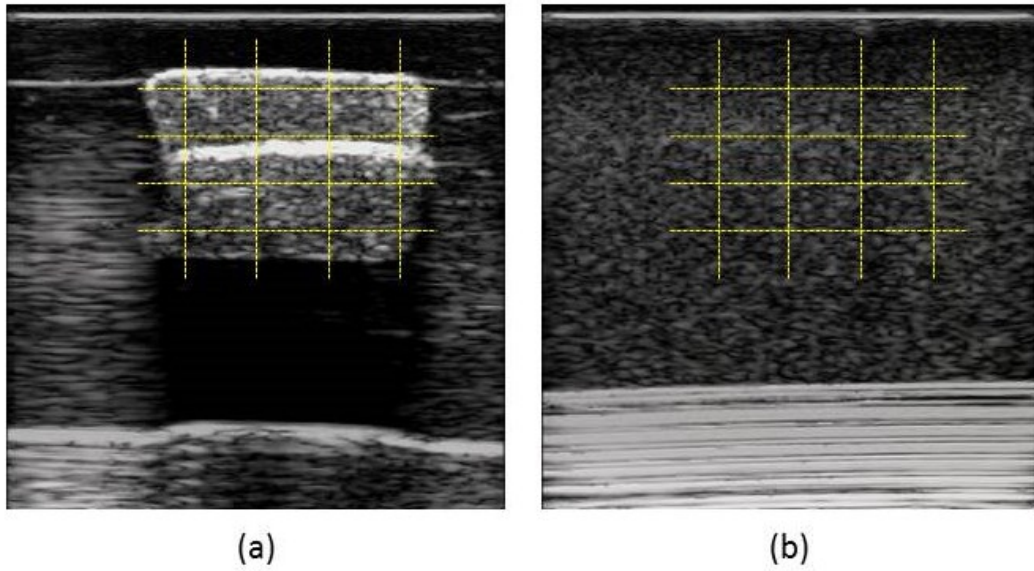


Figure 5.12 (a) Typical B-scan Image of Beef Data Set with 3×3 Grid Dividing Image into Patches (b) Typical B-scan Image of Speckle Phantom Data Set Divided into Patches by The Same Grid

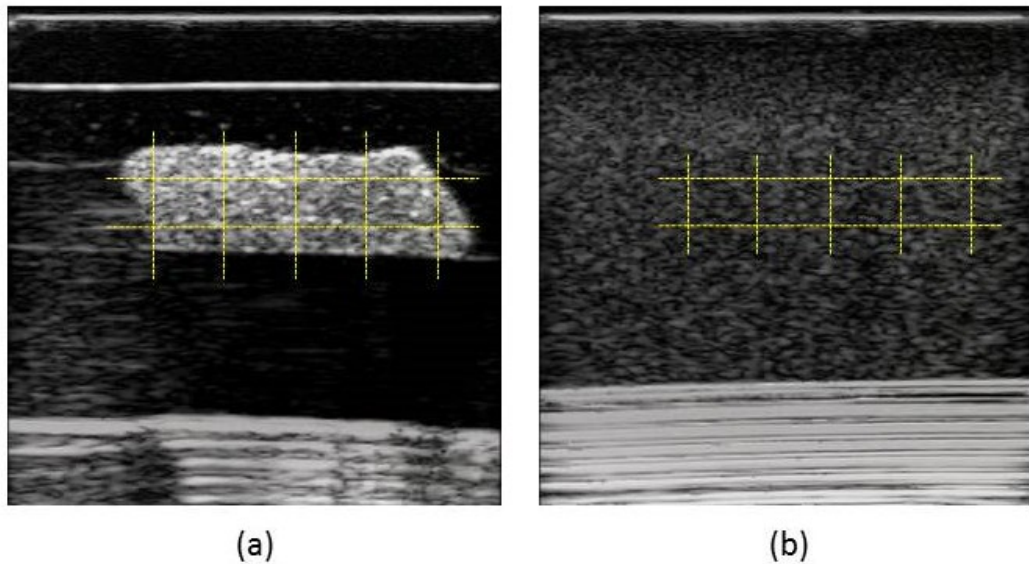


Figure 5.13 (a) Typical B-scan Image of Chicken Data Set with 1×4 Grid Dividing Image into Patches (b) Typical B-scan Image of Speckle Phantom Data Set Divided into Patches by The Same Grid

As it was discussed, the distance between any pair of frames was estimated by averaging all valid patch lookups on the elevational decorrelation curves. The mean and the standard deviation of these inter-scan spacings are shown in Table 5.1. Additionally,

the graphs represented in Figure 5.14, Figure 5.15, and Figure 5.16 show the mean of these inter-frame estimated distances, with the error bars representing \pm standard deviation, respectively for chicken, beef and human thigh data sets. It can be interpreted from the table that for the elevational distances ranged from 0.3 mm to 0.6 mm results of the chicken data set indicates errors of 3.45-8.76%. This range of error for the beef data set and human thigh data set are 0.34-5.26% and 1.41-7.31%, respectively. Since the results of Cambridge heuristic method also indicated errors in the nearly same range, it can be concluded that the method proposed in this thesis was successful in adopting and implementing Cambridge heuristic method on B-mode ultrasound images.

	Frame Separation (mm)							
	0.1± 0.001	0.2± 0.001	0.3± 0.001	0.4± 0.001	0.5± 0.001	0.6± 0.001	0.7± 0.001	0.8± 0.001
Chicken	0.2240 ±0.0508	0.2568 ±0.0465	0.3263 ±0.0279	0.4223 ±0.0703	0.4664 ±0.0527	0.6207 ±0.0969	0.6040 ±0.0544	0.6618 ±0.0794
Beef	0.2027 ±0.1013	0.2081 ±0.0278	0.3158 ±0.0549	0.4155 ±0.0530	0.4983 ±0.0734	0.5913 ±0.0877	0.6032 ±0.0413	0.6773 ±0.0784
Human thigh	0.1924 ±0.0612	0.2268 ±0.0364	0.3069 ±0.0509	0.3944 ±0.0659	0.4711 ±0.0594	0.5561 ±0.0823	0.5590 ±0.0731	0.6582 ±0.0794

Table 5.1 Elevational Distance Estimations (Results are shown as the mean distance estimated \pm one standard deviation for all frames separated by 0.1, 0.2, 0.3, 0.4, 0.5, 0.6, 0.7, and 0.8mm).

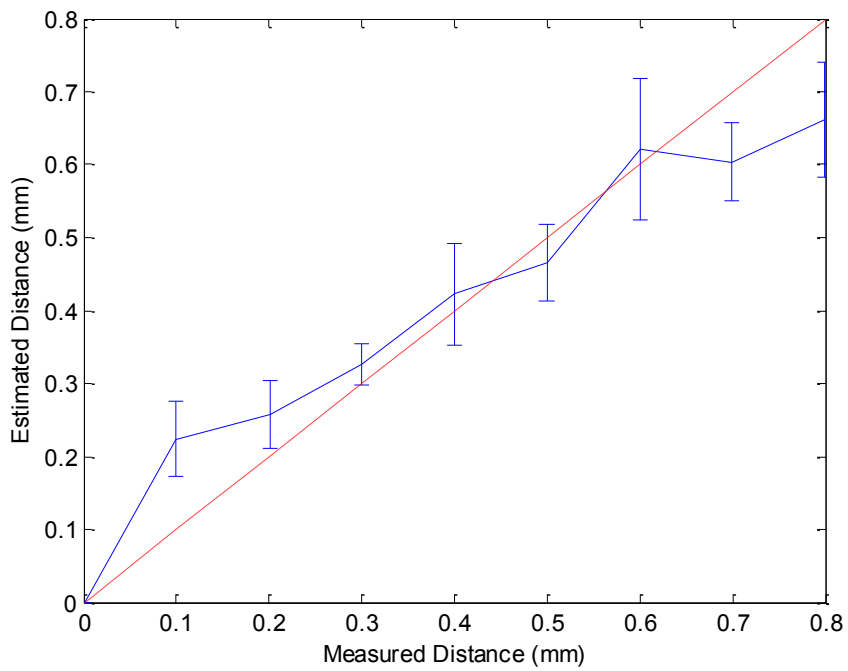


Figure 5.14 Elevational Distance Estimations for Chicken Data Set

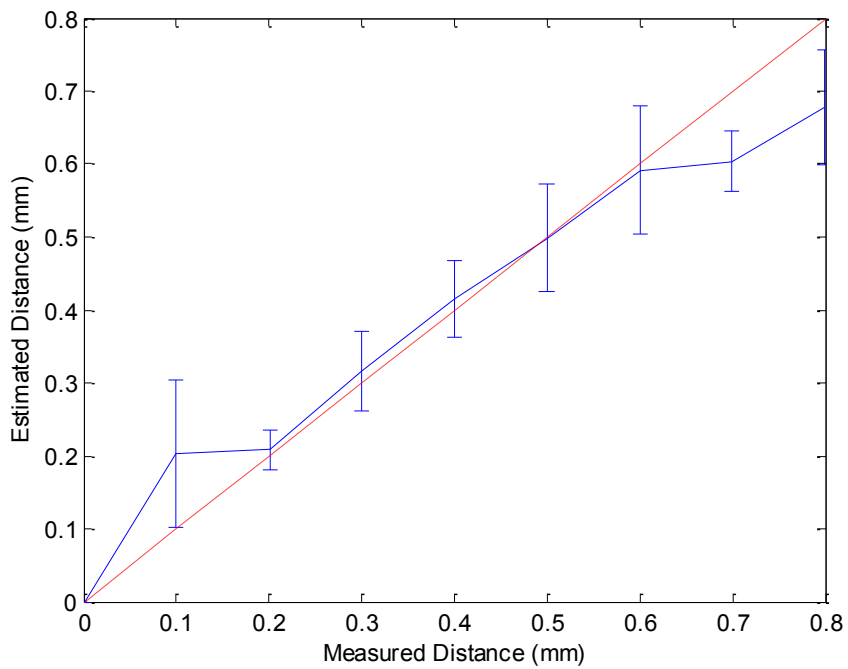


Figure 5.15 Elevational Distance Estimation for Beef Data Set

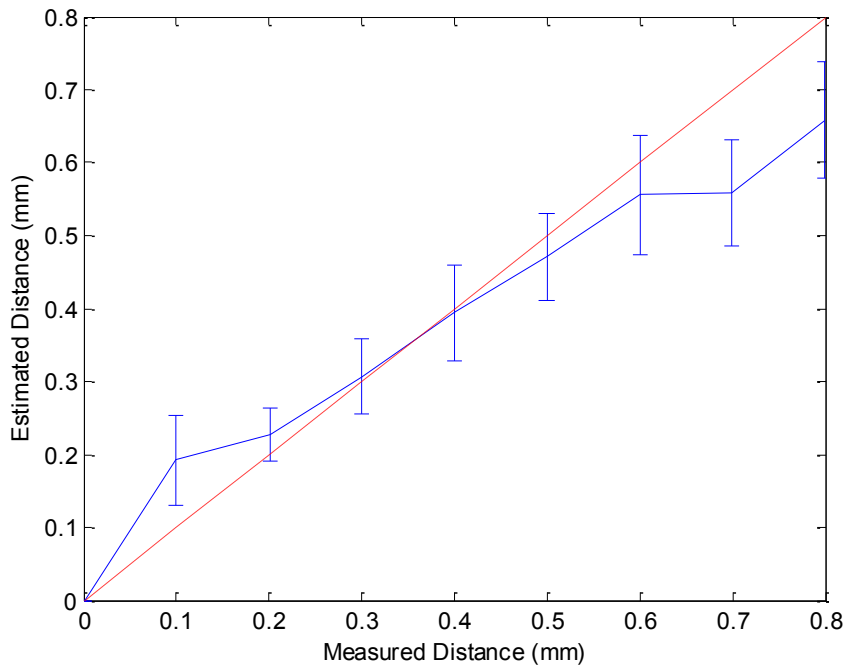


Figure 5.16 Elevational Distance Estimation for Human Thigh Data Set

5.5 Discussion

It can be seen from the graphs that the method works quite remarkable for the elevational distances ranged from 0.2 mm to 0.6 mm. The small errors in elevational distance estimation within this range is because the calibration curves are obtained by averaging many correlation measurements and it is not surprising that one specific measurement for two particular patches may differ slightly from the average. The larger errors for separation distances below 0.2 mm and above 0.6 mm are more systematic. When two patches are separated by either a very small or very large distance in the elevational direction, their correlation locates in the nearly flat regions of decorrelation curves in which a slight difference between measured correlation from and expected correlation will cause a significant difference in estimated distance. A schematic view of these regions of systematic error (gray regions) and the way that they cause inaccuracy in results is shown in Figure 5.17. Consider two patches are separated by a given very small elevational distance d_1 , if the measured correlation between these patches is slightly higher than expected correlation it causes an invalid lookup. On the other hand, if the measured correlation is slightly lower than the expected correlation it causes an overestimation of

elevational separation (d'_1). Similarly, we can consider two patches separated by a given very large elevational distance d_2 . If the measured correlation between these patches is slightly higher than expected correlation it causes an underestimation of elevational separation (d'_2) and if the measured correlation is slightly lower than expected correlation it results in an overestimation of elevational separation (d''_2).

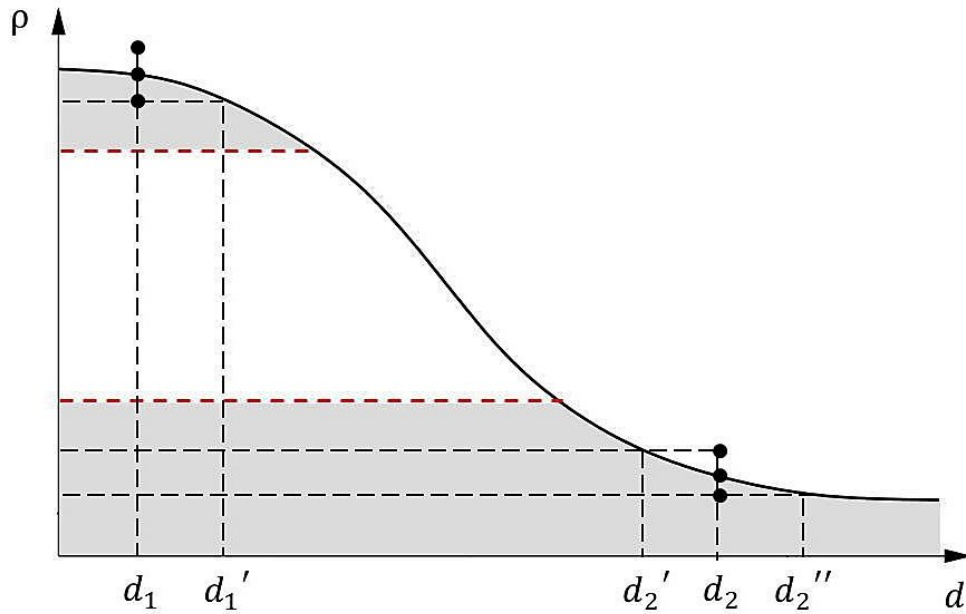


Figure 5.17 Systematic Errors Occurring for Frames Separated by Either Very Small or Very Large Distances in Elevational Direction (based on [13])

Since physiological motion is involved when scanning real tissue *in vivo*, the subject cannot be completely still during the experiment and it causes some amount of motion artifact in the images. Therefore it is expected for test phantoms to show more accurate results in comparison with real human tissue data set. This can explain the results of beef data set which are almost perfectly accurate (of course outside the systematic error regions). However, by comparing the results obtained for all data sets including chicken, beef and human tissue it can be concluded that the number of patches involved in analysis and their location in the image can make a great difference. In beef data set we consider 9 patches (see Figure 5.12) which are all located around the depth where the ultrasound beam is focused (1 cm focus on a 4 cm depth setting), but in chicken data set only 4 patches are involved and they all are located about 1 cm in depth lower than the ultrasound

beam focusing (see Figure 5.13). Since the distance estimations for chicken data set is based on a proportion of patches from the lower location in the B-scans than the focusing depth, the estimated elevational distances are more deviated from true elevational distances. The reason explaining this error is attenuation of ultrasound signals which increases going further in depth and consequently increases the noise in the image content (noise signal is essentially uncorrelated in all directions). For the same reason, the estimated distances for beef data set which are resulted from patches around the ultrasound focusing depth are quite matched to the true separation distances. Distance estimation results for the human tissue are based on patches from all over the B-scan image (both higher and lower depths than the ultrasound focusing depth and also patches located near the focusing depth), therefore it is not surprising that the average of these all estimations from all over the image is slightly deviated from true separation distances.

It was mentioned before that the gold standard considered in this study is the measured elevational distances by Patriot electromagnetic sensor and Patriot position readings themselves show deviations from the true elevational distances between frames. In fact, in this study the true elevational distances values are unknown and we are trying to evaluate a new measurement technique by comparing it with an established technique. The method commonly used in such cases is Bland-Altman method to assess the agreement between two measurement techniques [81]. The method is used when two methods are compared neither provides an unequivocally correct measurement. It plots the difference scores of two measurements against the mean for each subject and discusses that if the new method agrees sufficiently well with the established method, the old may be replaced. The Bland-Altman method calculates the mean difference between two methods of measurement, and 95% limits of agreement. It is expected that the 95% limits include 95% of differences between the two measurement methods. If the provided differences within the limits of agreement are not clinically important (depending on the clinical context and application), we can use the two measurement methods interchangeable. In fact, the smaller the range between these two limits the better the agreement is. The Bland-Altman plots for the data sets of this thesis are shown in Figure 5.18 to Figure 5.20.

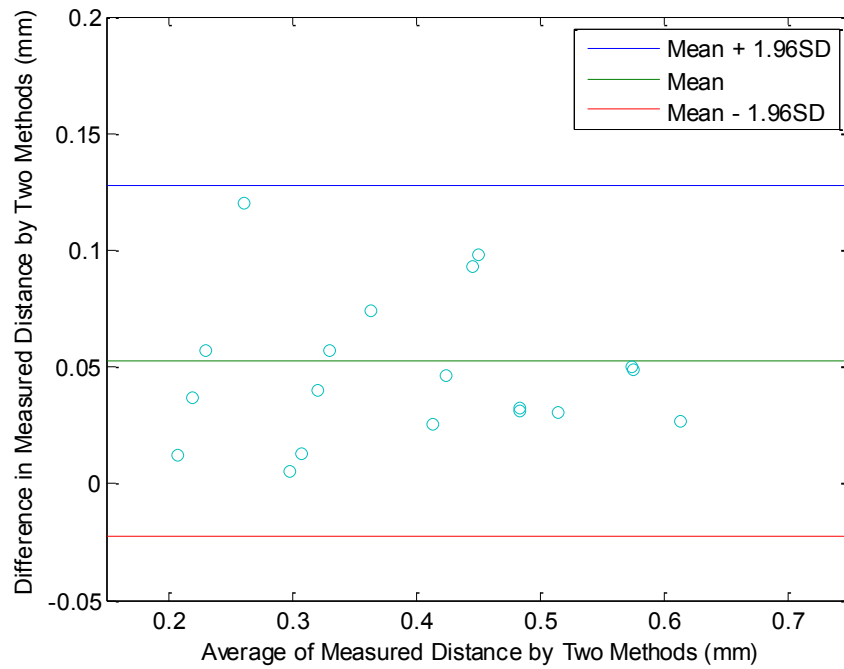


Figure 5.18 Difference against Mean for Elevational Distance Measurements of Chicken Data Set (Mean = 0.0526 mm, Standard Deviation = 0.0385 mm)

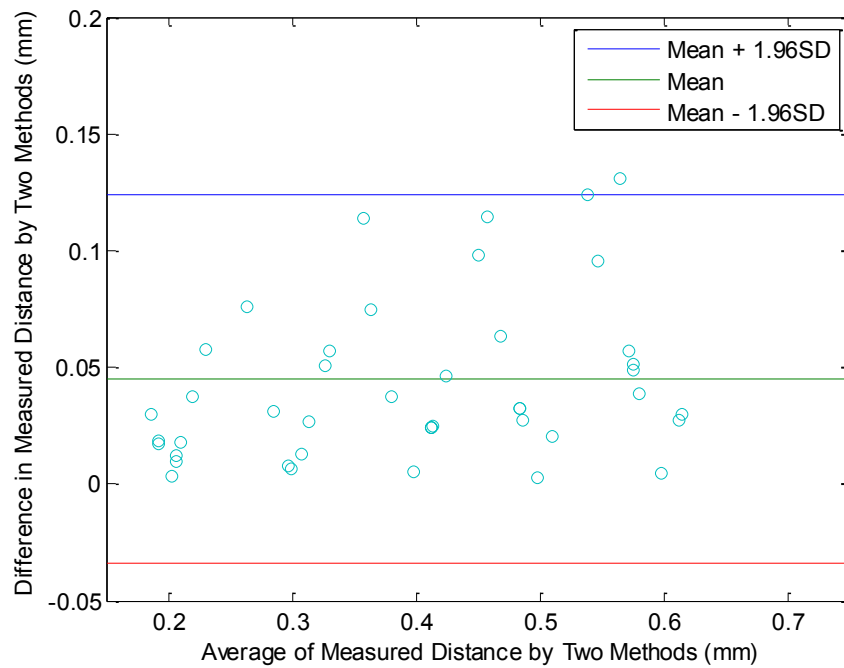


Figure 5.19 Difference against Mean for Elevational Distance Measurements of Beef Data Set (Mean = 0.0452 mm, Standard Deviation = 0.0403 mm)

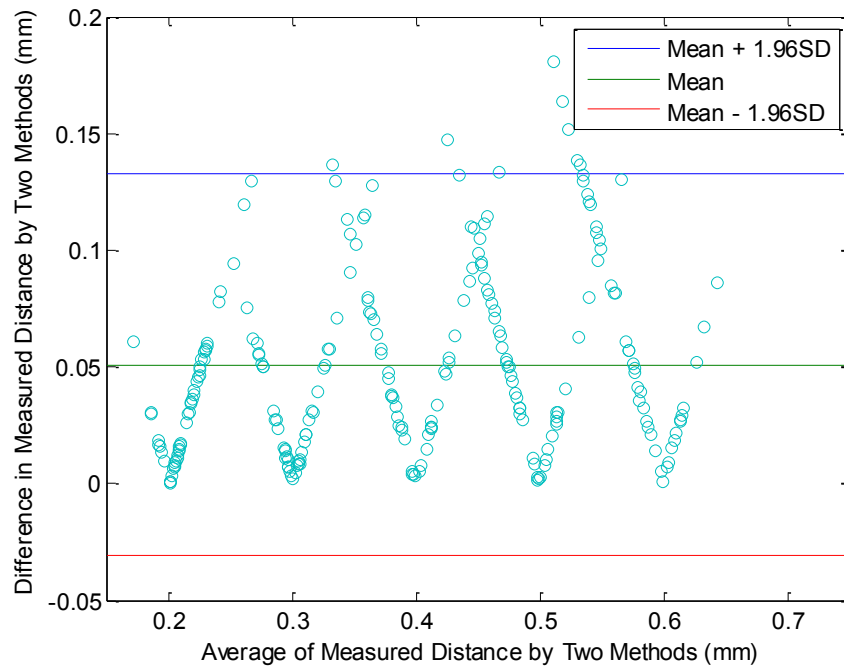


Figure 5.20 Difference against Mean for Elevational Distance Measurements of Human Thigh Data Set (Mean = 0.0510 mm, Standard Deviation = 0.0417 mm)

The formulation for calculating limits of agreement is given as $[\bar{d} - 1.96s, \bar{d} + 1.96s]$, where \bar{d} is the mean difference and s is the standard deviation of the differences. The calculated limits of agreement for different data sets are provided in Table 5.2. It can be seen from the table that the range between two limits is approximately equal to 0.15 mm for all data sets which is a quite sufficient accuracy for motion tracking task in the context of freehand 3D ultrasound imaging. Therefore, it can be concluded that the electromagnetic sensor can be replaced by the method proposed in this thesis for out-of-plane motion estimation and for elevational distances ranged from 0.2 mm to 0.6 mm.

	Chicken	Beef	Human Thigh
Limits of Agreement (mm)	-0.0227 – 0.1280	-0.0337 – 0.1241	-0.0308 – 0.1327

Table 5.2 Limits of Agreement Calculated Using Bland-Altman Method for Different Data Sets

Before finishing this section it is required to be mentioned that performing 3D reconstruction was not included in the defined framework of this thesis but the results of this study are intended to be used in 3D reconstruction tasks. In fact, the eventual goal of sensorless out-of-plane motion estimation is the 3D reconstruction of a whole volume from 2D ultrasound images. Therefore it would be a good idea to provide a brief discussion on the procedure and also the challenges standing in its way. For 3D reconstruction task, we need to position many frames in space relative to each other. In order to locate one frame relative to another one in 3D space, it is required to have the elevational distance estimations for at least three non-collinear patches of the two frames. Therefore a plane can be fitted to these set of points in space and the frame will be located in this plane. There are different methods for selecting these patches or for averaging between estimated distances of different patches to finally end up with the most accurate positioned three points in space. The most important challenge in positioning frames that the 3D reconstruction algorithm needs to deal with, is the error accumulation. Assuming that e is the mean error of the method in positioning one frame relative to previous frame, error accumulation causes an angular and distance error of the order ne in positioning of B-scan $i + n$ relative to B-scan i . Another important challenge is about the frames orientation; since the out-of-plane motion estimation results are not completely accurate, if the method underestimate the distance for some patches and overestimate the distance for some other patches it can cause a change in the frame orientation relative to previous frame. Also the method is not able to determine the direction of motion between frames which is an important factor in performing reconstruction task. Finally, considering the effect of in-plane translations and rotations can improve the results of out-of-plane motion estimation and consequently improve the results of 3D reconstruction algorithm.

Chapter 6

Conclusions and Future Work

This chapter will complete this thesis by providing a summary of the proposed experiments and algorithms, the major findings, and a number of recommendations to pursue as future works.

6.1 Conclusions

This thesis was trying to examine a method for sensorless out-of-plane displacement estimation between ultrasound B-scan images that can be used in freehand 3D ultrasound applications. The method used in this thesis is based on the speckle decorrelation approach and considers the effect of both FDS and non-FDS regions. The main contribution of this thesis was to adapt the method in a way to be applicable on B-mode ultrasound images. To the best of my knowledge, all previous research works on this topic have used RF ultrasound signals. Since RF data are not always available in clinical environments, adjustment of currently available successful methods in order to make them suitable for B-mode ultrasound images has a great importance. Another important contribution of this work was the usage of electromagnetic sensor for tracking motion of the probe and moving

the probe freely. It means that the motion of the probe was not constrained in any directions during the experiments unlike most previous works in this area that take advantage of using some mechanical device to constrain the probe motion to only pure elevational translation. In fact, we were dealing with a true freehand system with the encumbrance of in-plane motion which needed to be overcome. We also applied the method on real in vivo human data which are affected by both in-plane motion and the presence of physiological motions, and are more difficult to deal with.

In order to obtain accurate results on B-mode ultrasound images, experimental procedures and data processing algorithms were developed. The electromagnetic position tracking sensor was attached to the ultrasound probe and the speckle phantom (an artificial object that contains a great amount of randomly located ultrasound scatterers) was scanned. Temporal and spatial calibrations were applied on the data to label each image with the accurate position and orientation. B-scan images were divided into patches and their pixel values were converted to a linear scale. Data sets of frames at known regular elevational intervals were selected. After dealing with in-plane motion between frames, the correlation between the contents of those selected frames was measured and a transducer-specific decorrelation curve was fitted to the set of resulting correlation measurements. Decorrelation curves were not calculated in only elevational direction but also in axial and lateral direction. To examine the effect of coherent scattering, the axial and lateral decorrelation curves were also calculated for test data. By comparing axial and lateral decorrelation curves for each set of test data with their corresponding FDS calibrated curves an estimation of the amount of coherent scattering was obtained for each patch. Using this estimation and under isotropic medium assumption, the elevational FDS calibrated curves were adapted for each patch in each data set and these new adapted curves were used to estimate elevational displacement between frames.

The method was shown to be successful in accurately estimating elevational distances ranged from 0.2 mm to 0.6 mm for both test phantoms data sets and real human tissue experiment. The small errors in elevational distance estimation within this range was due to the deviation of one correlation measurement from the averages of many correlation measurements that are used to create the decorrelation curve. Physiological motion was also introduced as a source of error for in vivo human experiment. The errors for

estimations out of 0.2 mm to 0.6 mm range was because of locating correlation measurement in the nearly flat regions of decorrelation curves in which a slight difference between measured correlation from an expected correlation will cause a significant difference in estimated distance. Additionally, it was shown that the location of patches in the image can affect the results. In fact, motion estimation results obtained by considering patches located near the focusing depth of ultrasound beam showed better results in comparison with the patches located at depths lower than the focusing depth.

6.2 Future Works

In this section, three major avenues for further work are identified:

The first is to consider the effect of in-plane and out-of-plane rotations as well as in-plane translation on decorrelation curves. It would improve the accuracy of the method if we develop an algorithm to compensate for the in-plane and out-of-plane rotation before proceeding to out-of-plane translation estimation and it would make a difference in widespread clinical acceptance and usage of sensorless freehand 3D ultrasound systems.

The second is to design experiments to more specifically analyze the decorrelation curves adaptation scheme from the perspective of ultrasound physics and examine the sensitivity of the results to beam focusing depth. This may lead to develop the scheme and improve the results.

The third is to develop a powerful 3D reconstruction algorithm in order to make a whole 3D volume based on the estimated out-of-plane displacements between frames. Assuming that e is the mean error of the method in positioning one frame relative to previous frame, error accumulation causes an angular and distance error of the order ne in positioning of B-scan $i + n$ relative to B-scan i . Therefore the reconstruction algorithm is required to be designed specifically to deal with error accumulation challenge when positioning many frames in 3D space relative to each other.

References

- [1] Wackerhage, Henning, and Michael J. Rennie. , "How Nutrition and Exercise Maintain the Human Musculoskeletal Mass.," *Journal of anatomy*, vol. 208, no. 4, pp. 451-458, 2006.
- [2] Leunig, Michael, Paul E. Beaulé, and Reinhold Ganz., "The concept of femoroacetabular impingement: current status and future perspectives.," *Clinical orthopaedics and related research*, vol. 467, no. 3, pp. 616-622, 2009.
- [3] Tan, Ai Lyn, Richard J. Wakefield, Philip G. Conaghan, Paul Emery, and Dennis McGonagle., "Imaging of the musculoskeletal system: magnetic resonance imaging, ultrasonography and computed tomography.," *Best Practice & Research Clinical Rheumatology*, vol. 17, no. 3, pp. 513-528, 2003.
- [4] Nelson, Thomas R., and T. Todd Elvins., "Visualization of 3D ultrasound data.," *Computer Graphics and Applications, IEEE*, vol. 13, no. 6, pp. 50-57, 1993.
- [5] Wakefield, Richard J., Wayne W. Gibbon, Philip G. Conaghan, Philip O'Connor, Dennis McGonagle, Colin Pease, Michael J. Green, Douglas J. Veale, John D. Isaacs, and Paul Emery. , "The value of sonography in the detection of bone erosions in patients with rheumatoid arthritis: a comparison with conventional radiography.," *Arthritis & Rheumatism*, vol. 43, no. 12, pp. 2762-2770, 2000.
- [6] Fenster, Aaron, Donal B. Downey, and H. Neale Cardinal., "Three-dimensional ultrasound imaging.," *Physics in medicine and biology*, vol. 46, no. 5, p. R67, 2001.
- [7] Gee, Andrew, Richard Prager, Graham Treece, and Laurence Berman. , "Engineering a freehand 3D ultrasound system.," *Pattern Recognition Letters*, vol. 24, no. 4, pp. 757-777, 2003.
- [8] Afsham, Narges, Mohammad Najafi, Purang Abolmaesumi, and Robert Rohling.,

- "A Generalized Correlation-Based Model for Out-of-plane Motion Estimation in Freehand Ultrasound.," pp. 1-1, 2013.
- [9] Hsu, Po-Wei, Richard W. Prager, Andrew H. Gee, and Graham M. Treece., "Freehand 3D ultrasound calibration: A review.," *Springer Berlin Heidelberg*, 2009.
- [10] Prager, Richard W., Andrew H. Gee, Graham M. Treece, Charlotte JC Cash, and Laurence H. Berman., "Sensorless freehand 3-D ultrasound using regression of the echo intensity," *Ultrasound in medicine & biology*, vol. 29, no. 3, pp. 437-446, 2003.
- [11] Housden, R. James, Andrew H. Gee, Graham M. Treece, and Richard W. Prager., "Subsample interpolation strategies for sensorless freehand 3D ultrasound.," *Ultrasound in medicine & biology*, vol. 32, no. 12, pp. 1897-1904, 2006.
- [12] Tuthill, Theresa A., J. F. Krücker, J. Brian Fowlkes, and Paul L. Carson. , "Automated three-dimensional US frame positioning computed from elevational speckle decorrelation.," *Radiology*, vol. 209, no. 2, pp. 575-582, 1998.
- [13] Gee, Andrew H., R. James Housden, Peter Hassenpflug, Graham M. Treece, and Richard W. Prager., "Sensorless freehand 3D ultrasound in real tissue: speckle decorrelation without fully developed speckle.," *Medical image analysis*, vol. 10, no. 2, pp. 137-149, 2006.
- [14] Christensen, DOUGLAS A., "Ultrasonic bioinstrumentation," New York, wiley, 1988.
- [15] Hoskins, Peter R., Kevin Martin, Abigail Thrush, and T A Whittingham, *Diagnostic Ultrasound: Physics and Equipment*, London, England: Greenwich Medical Media Limited, 2003.
- [16] Bushong, Stewart C., and Benjamin R. Archer., *Diagnostic Ultrasound: Physics, Biology, and Instrumentation.*, St Louis: Mosby Year Book, 1991.
- [17] Kremkau, Frederick W., *Diagnostic Ultrasound: Principles and Instruments*, Seventh ed., Missouri: Saunders Elsevier, 2006.
- [18] Prince, Jerry L., and Jonathan M. Links. , *Medical Imaging: Signals and Systems*, Upper Saddle River: Pearson Prentice Hall, 2006.

- [19] Hedrick, Wayne R., David L. Hykes, and Dale E. Starchman. , *Ultrasound Physics and Instrumentation*, Fourth ed., Missouri: Elsevier Mosby, 2005.
- [20] Neau, Guillaume, and Deborah Hopkins., "The promise of ultrasonic phased arrays and the role of modeling in specifying systems," in *Proc. ASNT Fall Conference & Quality Testing Show*, Houston, 2006.
- [21] Charbonnier, Caecilia, Lazhari Assassi, Pascal Volino, and Nadia Magnenat-Thalmann., "Motion study of the hip joint in extreme postures.," *The Visual Computer* , vol. 25, no. 9, pp. 873-882, 2009.
- [22] Kaplan, Phoebe A., Aurello Matamoros Jr, and Joseph C. Anderson., "Sonography of the musculoskeletal system," *AJR. American journal of roentgenology* , vol. 155, no. 2, pp. 237-245, 1990.
- [23] Gibbon, Wayne William, Gillian Long, Dominic Anthony Barron, and Philip James O'Connor. , "Complications of orthopedic implants: sonographic evaluation.," *Journal of clinical ultrasound*, vol. 30, no. 5, pp. 288-299, 2002.
- [24] Lin, John, David P. Fessell, John A. Jacobson, William J. Weadock, and Curtis W. Hayes., "An illustrated tutorial of musculoskeletal sonography: Part I, introduction and general principles.," *American Journal of Roentgenology*, vol. 175, no. 3, pp. 637-645, 2000.
- [25] Cho, Kil-Ho, Young-Hwan Lee, Sung-Moon Lee, Muhammad Usman Shahid, Kyung Jin Suh, and Joon Hyuk Choi., "Sonography of bone and bone-related diseases of the extremities.," *Journal of Clinical Ultrasound*, vol. 32, no. 9, pp. 511-521, 2004.
- [26] Klauser, Andrea S., and Philippe Peetrons., "Developments in musculoskeletal ultrasound and clinical applications.," *Skeletal radiology*, vol. 39, no. 11, pp. 1061-1071, 2010.
- [27] Prager, Richard W., Umer Z. Ijaz, Andrew Gee, and Graham M. Treece., "Three-dimensional ultrasound imaging.," *Proceedings of the Institution of Mechanical Engineers, Part H: Journal of Engineering in Medicine*, vol. 224, no. 2, pp. 193-223, 2010.

- [28] Smith, Stephen W., Henry G. Pavy Jr, and Olaf T. von Ramm., "High-speed ultrasound volumetric imaging system. I. Transducer design and beam steering.," *Ultrasonics, Ferroelectrics and Frequency Control, IEEE Transactions*, vol. 38, no. 2, pp. 100-108, 1991.
- [29] Light, Edward D., and Stephen W. Smith., "Two dimensional arrays for real time 3D intravascular ultrasound.," *Ultrasonic imaging*, vol. 26, no. 2, pp. 115-128, 2004.
- [30] Rohling, Robert Nicholas., "3D freehand ultrasound: reconstruction and spatial compounding.," Th se de Doctorat University of Cambridge, UK, 1998.
- [31] Bosch, John A., Coordinate measuring machines and systems, CRC Press, 1995.
- [32] Birkfellner, W., F. Watzinger, F. Wanschitz, G. Enislidis, C. Kollmann, D. Rafolt, R. Nowotny, R. Ewers, and H. Bergmann. , "Systematic distortions in magnetic position digitizers.," *Medical physics*, vol. 25, no. 11, pp. 2242-2248, 1998.
- [33] Hummel, J., M. Figl, W. Birkfellner, Michael R. Bax, R. Shahidi, C. R. Maurer Jr, and H. Bergmann., "Evaluation of a new electromagnetic tracking system using a standardized assessment protocol.," *Physics in medicine and biology*, vol. 51, no. 10, p. N205, 2006.
- [34] Prager, Richard W., Andrew Gee, and Laurence Berman., "Stradx: real-time acquisition and visualization of freehand three-dimensional ultrasound.," *Medical Image Analysis*, vol. 3, no. 2, pp. 129-140, 1999.
- [35] Prager, Richard W., Robert Rohling, Andrew Gee, and Laurence Berman., "Rapid calibration for 3-D freehand ultrasound.," *Ultrasound in medicine & biology*, vol. 24, no. 6, pp. 855-869, 1998.
- [36] Hughes, S. W., T. J. D'Arcy, D. J. Maxwell, W. Chiu, A. Milner, J. E. Saunders, and R. J. Sheppard. , "Volume estimation from multiplanar 2D ultrasound images using a remote electromagnetic position and orientation sensor.," *Ultrasound in medicine & biology*, vol. 22, no. 5, pp. 561-572, 1996.
- [37] Mercier, Laurence, Thomas Langø, Frank Lindseth, and Louis D. Collins., "A review of calibration techniques for freehand 3-D ultrasound systems.," *Ultrasound*

- in medicine & biology*, vol. 31, no. 2, pp. 143-165, 2005.
- [38] Solberg, Ole Vegard, Frank Lindseth, Hans Torp, Richard E. Blake, and Toril A. Nagelhus Hernes., "Freehand 3D ultrasound reconstruction algorithms—a review," *Ultrasound in medicine & biology*, vol. 33, no. 7, pp. 991-1009, 2007.
- [39] Sherebrin, Shi, Aaron Fenster, Richard N. Rankin, and David Spence. , "Freehand three-dimensional ultrasound: implementation and applications.," *Medical Imaging 1996. International Society for Optics and Photonics.*, 1996.
- [40] Martens, D. I. T. L. E. F., and O. H. Gilja., "The EchoPAC-3D software for 3D image analysis.," *Basic and new aspects of gastrointestinal ultrasonography. Singapore: World Scientific*, pp. 305-29, 2005.
- [41] Carr, Jonathan C., Jan L. Stallkamp, Michelle M. Fynes, Andrew H. Gee, Richard W. Prager, Graham M. Treece, Chris Overton, and Laurence Berman. , "Design of a clinical free-hand 3D ultrasound system," in *Medical Imaging 2000. International Society for Optics and Photonics*, 2000.
- [42] McCann, Hugh A., Joseph C. Sharp, Thomas M. Kinter, C. Neill McEwan, Christian Barillot, and James F. Greenleaf., "Multidimensional ultrasonic imaging for cardiology.," *Proceedings of the IEEE*, vol. 76, no. 9, pp. 1063-1073, 1988.
- [43] Estépar, Raúl San José, Marcos Martín-Fernández, Carlos Alberola-López, James Ellsmere, Ron Kikinis, and Carl-Fredrik Westin., "Freehand ultrasound reconstruction based on roi prior modeling and normalized convolution.," *Medical Image Computing and Computer-Assisted Intervention-MICCAI 2003. Springer Berlin Heidelberg*, pp. 382-390, 2003.
- [44] San Jose-estepar, Raul, M. A. R. C. O. S. MARTIn-FERNAndez, P. Pablo Caballero-Martínez, Carlos Alberola-López, and Juan Ruiz-Alzola., "A theoretical framework to three-dimensional ultrasound reconstruction from irregularly sampled data.," *Ultrasound in medicine & biology*, vol. 29, no. 2, pp. 255-269, 2003.
- [45] Barry, C. D., C. P. Allott, N. W. John, P. M. Mellor, P. A. Arundel, D. S. Thomson, and J. C. Waterton. , "Three-dimensional freehand ultrasound: image reconstruction and volume analysis.," *Ultrasound in medicine & biology*, vol. 23, no. 8, pp. 1209-1224, 1997.

- [46] Rohling, Robert, Andrew Gee, and Laurence Berman., "A comparison of freehand three-dimensional ultrasound reconstruction techniques.," *Medical image analysis*, vol. 3, no. 4, pp. 339-359, 1999.
- [47] Sanches, João M., and Jorge S. Marques., "A Rayleigh reconstruction/interpolation algorithm for 3D ultrasound.," *Pattern recognition letters*, vol. 21, no. 10, pp. 917-926, 2000.
- [48] Afsham, Narges, Mohammad Najafí, Purang Abolmaesumi, and R. Rohling. , "Out-of-plane motion estimation based on a Rician-Inverse Gaussian model of RF ultrasound signals: speckle tracking without fully developed speckle.," in *SPIE Medical Imaging. International Society for Optics and Photonics*, 2012.
- [49] Zahiri-Azar, Reza, and Septimiu E. Salcudean., "Motion estimation in ultrasound images using time domain cross correlation with prior estimates.," *Biomedical Engineering, IEEE Transactions on*, vol. 53, no. 10, pp. 1990-2000, 2006.
- [50] Treece, Graham M., Richard W. Prager, Andrew H. Gee, and L. Berman. , "Correction of probe pressure artifacts in freehand 3D ultrasound.," *Medical Image Analysis*, vol. 6, no. 3, pp. 199-214, 2002.
- [51] Hassenpflug, Peter, Richard W. Prager, Graham M. Treece, and Andrew H. Gee., "Speckle classification for sensorless freehand 3-D ultrasound.," *Ultrasound in medicine & biology*, vol. 31, no. 11, pp. 1499-1508, 2005.
- [52] Rivaz, Hassan, Emad Boctor, and Gabor Fichtinger., "A robust meshing and calibration approach for sensorless freehand 3D ultrasound.," *Medical Imaging. International Society for Optics and Photonics*, 2007.
- [53] Laporte, Catherine, and Tal Arbel., "Learning to estimate out-of-plane motion in ultrasound imagery of real tissue.," *Medical image analysis* , vol. 15, no. 2, pp. 202-213, 2011.
- [54] Crawford, D. C., D. O. Cosgrove, E. Tohno, W. E. Svensson, B. Al-Murrani, D. S. Bell, K. Stepniewska, and J. C. Bamber. , "Visual impact of adaptive speckle reduction on US B-mode images.," *Radiology*, vol. 183, no. 2, p. 555-561, 1992.
- [55] Loizou, Christos P., Constantinos S. Pattichis, Christodoulos I. Christodoulou,

- Robert SH Istepanian, Marios Pantziaris, and Andrew Nicolaidis., "Comparative evaluation of despeckle filtering in ultrasound imaging of the carotid artery.," *Ultrasonics, Ferroelectrics and Frequency Control, IEEE Transactions on*, vol. 52, no. 10, pp. 1653-1669, 2005.
- [56] Leroy, Antoine, Pierre Mozer, Yohan Payan, and Jocelyne Troccaz. , "Intensity-based registration of freehand 3D ultrasound and CT-scan images of the kidney.," *International journal of computer assisted radiology and surgery*, vol. 2, no. 1, pp. 31-41, 2007.
- [57] Tay, Peter C., Bing Li, Chris D. Garson, Scott T. Acton, and John A. Hossack. , "Left ventricle segmentation using model fitting and active surfaces.," *Journal of signal processing systems*, vol. 55, no. 1-3, pp. 139-156, 2009.
- [58] Sanches, João M., and Jorge S. Marques., "A Rayleigh reconstruction/interpolation algorithm for 3D ultrasound.," *Pattern recognition letters*, vol. 21, no. 10, pp. 917-926, 2000.
- [59] Chivers, R. C., "Tissue characterization.," *Ultrasound in medicine & biology*, vol. 7, no. 1, pp. 1-20, 1981.
- [60] Bhandari, Anil K., and Navin C. Nanda., "Myocardial texture characterization by two-dimensional echocardiography.," *The American journal of cardiology*, vol. 51, no. 5, pp. 817-825, 1983.
- [61] Thijssen, J. M., B. J. Oosterveld, P. C. Hartman, and G. J. E. Rosenbusch. , "Correlations between acoustic and texture parameters from RF and B-mode liver echograms.," *Ultrasound in medicine & biology*, vol. 19, no. 1, pp. 13-20, 1993.
- [62] Thijssen, Johan M., "Ultrasonic speckle formation, analysis and processing applied to tissue characterization.," *Pattern Recognition Letters*, vol. 24, no. 4, pp. 659-675, 2003.
- [63] Jensen, Jørgen Arendt., "A model for the propagation and scattering of ultrasound in tissue.," *Acoustical Society of America. Journal*, vol. 89, no. 1, pp. 182-190, 1991.
- [64] Ng, James, Richard Prager, Nick Kingsbury, Graham Treece, and Andrew Gee.,

- "Modeling ultrasound imaging as a linear, shift-variant system.," *Ultrasonics, Ferroelectrics and Frequency Control, IEEE Transactions on*, vol. 53, no. 3, pp. 549-563, 2006.
- [65] Goodman, Joseph W., "Statistical properties of laser speckle patterns.," *Laser speckle and related phenomena. Springer Berlin Heidelberg*, pp. 9-75, 1975.
- [66] Wagner, Robert F., Stephen W. Smith, John M. Sandrik, and Hector Lopez. , "Statistics of speckle in ultrasound B-scans.," *IEEE TRANS. SONICS ULTRASONICS*, vol. 30, no. 3, pp. 156-163, 1983.
- [67] Chen, Jian-Feng, J. Brian Fowlkes, Paul L. Carson, and Jonathan M. Rubin. , "Determination of scan-plane motion using speckle decorrelation: theoretical considerations and initial test.," 1997.
- [68] "esaote uk," Esaote S.p.A., [Online]. Available: http://www.esaote.co.uk/modules/core/page.asp?p=ART_LAB. [Accessed 25 July 2014].
- [69] Silver, Jason I., "Development of Ultrasound Based Techniques for Measuring Skeletal Muscle Motion," Diss. Carleton University, Ottawa, 2009.
- [70] E. Esaote, "Picus User Manual: Instructions for Use and Technical Discription," 2008.
- [71] "POLHEMUS INNOVATION IN MOTION," POLHEMUS, 2014. [Online]. Available: <http://www.polhemus.com/motion-tracking/all-trackers/patriot/>. [Accessed 25 July 2014].
- [72] Patriot Brochure, Polhemus, [Online]. Available: http://polhemus.com/_assets/img/PATRIOT_Brochure.pdf.
- [73] Polhemus, "Patriot User Manual," 2012.
- [74] Detmer, Paul R., Gerard Bashein, Timothy Hodges, Kirk W. Beach, Eric P. Filer, David H. Burns, and D. Eugene Strandness Jr., "3d ultrasonic image feature localization based on magnetic scanhead tracking:< i> In vitro</i> calibration and validation.," *Ultrasound in medicine & biology*, vol. 20, no. 9, pp. 923-936, 1994.
- [75] Barry, C. D., C. P. Allott, N. W. John, P. M. Mellor, P. A. Arundel, D. S. Thomson,

- and J. C. Waterton., "Three-dimensional freehand ultrasound: image reconstruction and volume analysis.," *Ultrasound in medicine & biology*, vol. 23, no. 8, pp. 1209-1224, 1997.
- [76] "PATRIOT USER MANUAL," Polhemus, Colchester, Vermont, U.S.A., 2012.
- [77] Craig, John J., Introduction to robotics: mechanics and control., Reading, MA: Addison-Wesley, 1989.
- [78] Smith, Wendy L., and Aaron Fenster., "Optimum scan spacing for three-dimensional ultrasound by speckle statistics.," *Ultrasound in medicine & biology*, vol. 26, no. 4, pp. 551-562, 2000.
- [79] Krupa, Alexandre, Gabor Fichtinger, and Gregory D. Hager., "Real-time motion stabilization with B-mode ultrasound using image speckle information and visual servoing.," *The International Journal of Robotics Research*, vol. 28, no. 10, pp. 1334-1354, 2009.
- [80] Conrath, Juliette, and Catherine Laporte., "Towards Improving the Accuracy of Sensorless Freehand 3D Ultrasound by Learning.," *Machine Learning in Medical Imaging. Springer Berlin Heidelberg*, pp. 78-85, 2012.
- [81] Bland, J. Martin , and DouglasG Altman., "Statistical methods for assessing agreement between two methods of clinical measurement.," *The lancet*, vol. 327, no. 8476, pp. 307-310, 1986.